August 2015

Vortex-Induced Vibration of Structures with Broken Symmetry

Banafsheh Seyedaghazadeh
University of Massachusetts - Amherst

VORTEX-INDUCED VIBRATION OF STRUCTURES WITH BROKEN SYMMETRY

A Dissertation Presented

by

BANAFSHEH SEYEDAGHAZADEH

Submitted to the Graduate School of the
University of Massachusetts Amherst in partial fulfillment
of the requirements for the degree of

DOCTOR OF PHILOSOPHY

May 2015

Department of Mechanical and Industrial Engineering

VORTEX-INDUCED VIBRATION OF STRUCTURES WITH BROKEN SYMMETRY

A Dissertation Presented

By

BANAFSHEH SEYEDAGHAZADEH

Approved as to style and content by:

_____
Yahya Modarres-Sadeghi, Chair

_____
David Schmidt, Member

_____
Sanjay Raja Arwade, Member

_____
Donald Fisher, Department Head
Department of Mechanical and Industrial Engineering

To my parents and my loving husband,

who always provided me with their unconditional support. Their love was my inspiration and my driving force. Without their love and support this project would not have been made possible.

ACKNOWLEDGMENTS

I would like to thank my advisor, Prof. Yahya Modarres-Sadeghi for his guidance and continuous support. He has been an invaluable mentor, supporting and encouraging me throughout the course of my graduate studies. I would also like to extend my gratitude to the members of my committee, Prof. Jonathan Rothstein, Prof. David Schmidt and Prof. Sanjay Raja Arwade for their support and insight on this project.

A special thank you to all the Mechanical Engineering undergraduates who helped me during the course of experiments; Robert J. Pizzano Jr., Collin Budz, Austin Priebe, Robert Cummings, Eric Baggan and Griffin MacCarn. I would like to specially thank Dan Carlson, who was always there when I needed help in running experiments at the water tunnel, no matter how long that took. Thanks to Rick Winn and Al Rakouskas from the MIE Department for their help in setting up the experiments.

A special thank you to all my friends and especially my wonderful lab-mates, Pariya, Gary and Anil whose support and friendship helped me to stay focused on this project and who have provided me with the encouragement to continue when the going got tough.

Last but not least, I am deeply grateful to my family and my loving husband, Hamed for always supporting and encouraging me to follow my dreams.

ABSTRACT

VORTEX-INDUCED VIBRATION OF STRUCTURES WITH BROKEN SYMMETRY

MAY 2015

BANAFSHEH SEYEDAGHAZADEH

B.Sc. UNIVERSITY OF TABRIZ

M.Sc. UNIVERSITY OF TABRIZ

Ph.D., UNIVERSITY OF MASSACHUSETTS AMHERST

Directed by: Professor Yahya Modarres-Sadeghi

A bluff body, i.e., an object with a blunt cross-section immersed in cross-flow forms an unstable wake, resulting in the formation of large-scale vortical structures, which induce unsteady forces on the body. If the body is flexible or flexibly mounted, vortex-induced vibration (VIV) results, which can have significant implications for a number of physical systems, from aeolian harps to power transmission lines, towing cables, undersea pipelines, drilling risers and mooring lines used to stabilize offshore floating platforms. VIV has been a major subject of research in recent years. The majority of these studies have focused on symmetric systems in which the structure, its geometry, its boundary conditions and the incoming flow are symmetric. However, in many real-world applications, VIV occurs in asymmetric systems. A flexibly-mounted vertical uniform circular cylinder which is placed in a uniform current is an example of a system with symmetric geometry, boundary conditions and wake. This geometry is usually considered as a canonical configuration in modeling structures undergoing VIV. However, many other configurations can exist in

which the geometrical symmetry of the system is broken, such as an inclined cylinder in which the cylinder is placed with an angle with respect to the incoming flow direction, or a tapered cylinder in which the diameter of the circular cylinder varies along its length, or when the geometry of the cross-section changes from circular to other shapes such as square or triangle. Also, in some other cases, such as a circular cylinder which is forced to rotate about its long axis, the symmetry of the surrounding wake is broken by the rotation imposed on the cylinder. These cases among many examples are systems with broken symmetry, and are widely used in the offshore industry. The main objective of this thesis is to study VIV of systems with broken symmetry. For this purpose, experiments are conducted and the VIV response of the systems are studied in terms of amplitude and frequency of oscillations as well as the wake of the cylinder. It is shown that higher harmonics contributions of flow forces play an important role in VIV of structures. Also, various taper ratios in VIV of tapered cylinders are found to be the major parameters influencing the VIV response of tapered cylinders. Different rotation rates in VIV of a rotating cylinder, various angles of attack in VIV of a triangular cylinder and different angles of inclination in VIV of flexible inclined cylinder are found to be the influencing parameters in studying the VIV of structures with broken symmetry.

TABLE OF CONTENTS

Page

LIST OF TABLES

LIST OF FIGURES

CHAPTER 1

INTRODUCTION

The subject of vortex-induced vibrations (VIV) is of practical interest in many engineering fields, occurring in numerous real world applications such as offshore structures, marine cables, towed cables, drilling risers in petroleum production, mooring cables, tethered structures, pipelines and other hydrodynamic applications.

Vortex-induced vibrations can be categorized as a subset of flow-induced instabilities, in which the structural instability is originated from the shed vortices, leading to relatively large amplitudes of oscillations within a range of flow velocities. VIV has a self-limiting nature owing to the energy balance between the excitation forces from periodic vortex shedding and the damping induced by the surrounding fluid. Hence, the instability caused by VIV is different from other unstable oscillations typically occurring. Despite the moderate amplitude of oscillations caused by VIV, the structure fails as a consequence of fatigue caused by periodic oscillations of the structure.

The objective in several VIV studies is to understand the underlying physics with the goal of controlling VIV. On the other hand, recently, the structures undergoing VIV are becoming known as sources of energy harvesting and several recent investigations have focused on extracting energy from these systems (Bernitsas et al., 2008; Abdelkefi et al., 2012; Grouthier et al., 2012).

Understanding the underlying mechanism of VIV has been partly achieved through some numerical methods such as Reynolds-averaged Navier–Stokes equations (RANS), large eddy simulations (LES), vortex element methods (VEM), and their various combinations (Bearman, 1984; Sarpkaya, 2004; Williamson and Govardhan, 2004; Wu et al., 2012). Recently, by the advancement of computational power, the direct numerical simulations methods are being used to study VIV systems (Evangelinos et al., 2000; Dong and Karniadakis, 2005; Bourguet et al., 2012). Laboratory tests are among the reliable methods in understanding the physics of VIV. Owing to the fact that different system parameters in experimental tests can be controlled and adjusted, empirical codes are broadly used in studying VIV (Vandiver and Li, 1995; Triantafyllou et al., 1999; Larsen et al., 2000).

The majority of the existing experimental and numerical studies have been conducted for the symmetric system; i.e. systems with symmetric geometries, boundary conditions and wakes. However, in many real-world applications, VIV is observed in systems with asymmetry. It is worth noting that when the symmetry is broken, the structure can experience other flow-induced instabilities, as well. For instance, an asymmetric geometry of the structure might lead to galloping, in which the structure experiences low frequency large-amplitude oscillations, as opposed to VIV in which the maximum amplitude of oscillations is limited to around one cylinder diameter. VIV of the structures with broken symmetry has received much less attention than the symmetric systems, mainly because of the complexities such as three-dimensionality in the surrounding fluid that is being introduced to such systems.

The main objective of this thesis is to study VIV of systems with a broken symmetry in the boundary conditions, for example in curved, tapered and inclined cylinders, and some other with asymmetry in their surrounding wake, such as rotating cylinders in flow.

This thesis is organized as follows: Chapter 2 contains a brief summary of the fundamentals of the flow around a stationary cylinder, vortex induced vibrations, the important parameters used in VIV and a summary of different approaches in studying VIV. Chapter 3 focuses on VIV of tapered cylinder and the influence of taper ratio on the VIV of the cylinder is investigated. Chapter 4 discusses VIV of a curved circular cylinder. The influences of higher harmonic flow forces are investigated on the VIV response of the curved cylinder. Chapter 5 focuses on the VIV of a rotating cylinder. It focuses on the asymmetric wake around the fixed and oscillating cylinder and the influence of different rotation rates on VIV. Chapter 6 discusses the flow characteristics and flow-induced vibrations of a stationary and oscillating triangular cylinder. The response of the system is studied in terms of the amplitude of oscillations as well as the flow forces at varying angles of attack. Chapter 7 discusses VIV of flexible inclined cylinders. The dynamic response is studied for different angles of inclination and the validity of the Independence Principle (IP) is investigated. Finally, in Chapter 8, a general conclusion is presented. This chapter sums up topics of discussion in the thesis and points out main contributions of the present study and possible ideas for the future works.

CHAPTER 2

INTRODUCTION AND BACKGROUND

In this chapter, an introduction to the fundamentals of vortex shedding and vortex-induced vibrations (VIV) of the structures is presented. Starting from the flow around stationary cylinders, the VIV phenomenon is introduced. A review of previous studies on VIV is provided.

2.1 Flow around stationary bluff body

For a bluff body, defined as an object that has a blunt cross section such as a circular cylinder, immersed in flow, the surrounding flow is characterized by the Reynolds number defined as

$$\mathrm{Re} = \frac{\rho U D}{\mu} \tag{2.1}$$

in which, ρ is the fluid density, U the flow velocity, D cylinder diameter and μ is the flow viscosity.

At very low Reynolds numbers ($Re < 5$), the streamlines of the flow around a circular cylinder resemble those of the potential flow solution and the flow remains unseparated. In this case, stagnation points (points where the local velocity of the fluid is zero) exist both fore and aft of the cylinder (Blevins, 1990). As Reynolds number increases slightly ($5 < Re < 40$), two vortices form in the wake of the cylinder but still remain attached

to the cylinder and the wake is still steady in this case. Beyond $Re \approx 40$, the wake becomes unstable and small perturbations in the flow or on the surface of the cylinder will cause vortices to break off from the cylinder and shed periodically downstream (Bearman, 1984). Different flow regimes around the stationary circular cylinder as a function of Re number are shown in Figure 2.1 (Blevins, 1990). While vortex shedding can occur in general for any bluff body, flow around circular cylinders has been studied widely as a canonical structure used in real life applications. There exists a common feature for the flow around circular cylinder for $Re>40$, in which vortex shedding behind the cylinder follows the Von-Karman street pattern as shown in Figure 2.2; two vortices with opposite rotations are shed with a frequency of vortex shedding ,f_v, which is non-dimensionalized as:

$$St = \frac{f_v D}{U} \tag{2.2}$$

where, St is the Strouhal number. It has been shown experimentally that the Strouhal number is a function of Reynolds number which stays around a constant $St=0.2$ for a large range of Re in subcritical regime ($Re<3\times10^5$) for a circular cylinder as shown in Figure 2.3.

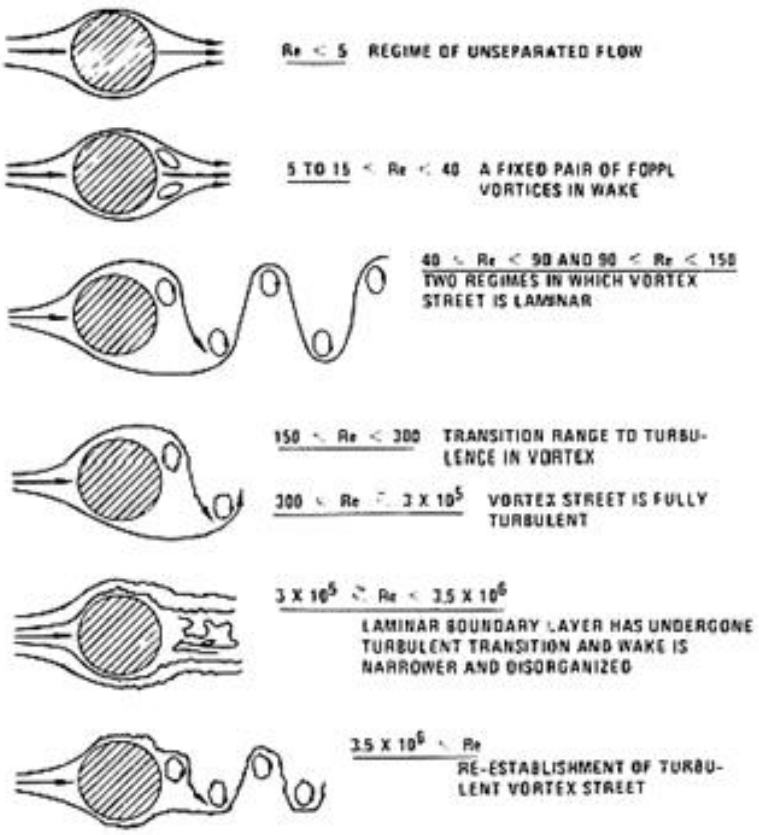

Figure 2.1. Different flow regimes across stationary circular cylinder (Blevins, 1990).

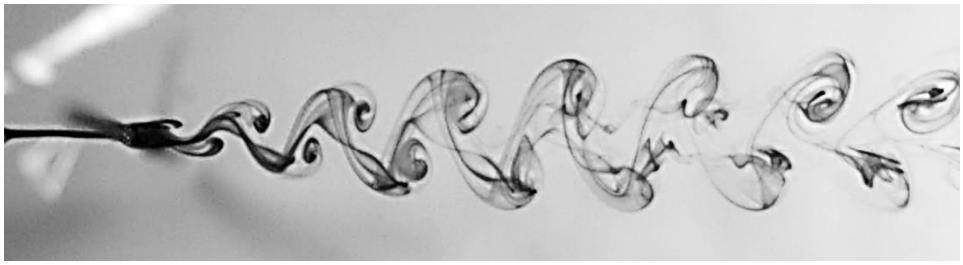

Figure 2.2. Von-Karman street behind a stationary circular cylinder at *Re*=100. The visualization is conducted for this study using the method discussed later in Chapter 3.

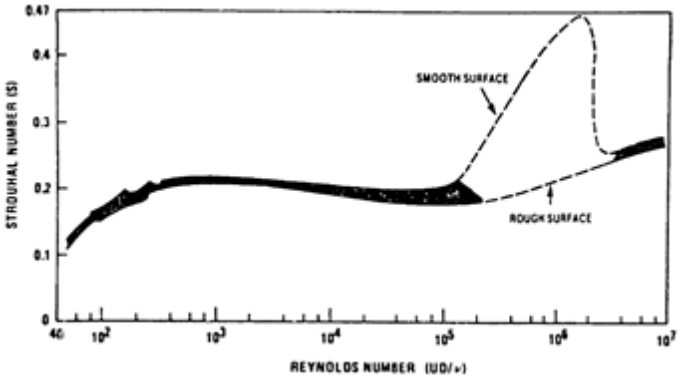

Figure 2.3. Strouhal number as a function of Reynolds number for stationary circular cylinder (Blevins, 1990).

2.2 Vortex-induced vibrations

If the structure is flexible or flexibly mounted, synchronization can occur during which the frequency of the vortex shedding gets close to the natural frequency of the structure. At this time, the body motion takes the control over the vortex shedding frequency and deviates it from the Strouhal law to a different value: the frequency of oscillation. Hence, the structure will be excited by the periodic forces from vortex shedding and the structure undergoes relatively large amplitude oscillations. This is called vortex-induced vibrations (VIV) (Bearman, 1984). At the time the structure starts to oscillate under the influence of vortex shedding in its wake, the surrounding flow will be also influenced by the movement of the cylinder. There will be a feedback mechanism through this fluid-structure interaction and finally the structure and the surrounding flow will reach a stable dynamic equilibrium in which the flow and the structure will get to a balanced energy level. One of the features of VIV is that the amplitude of oscillations does not grow indefinitely; instead, the maximum amplitude of oscillations is limited to about one cylinder diameter. Consequently, what makes failure in structure undergoing VIV is not

the failure due to the large amplitude of oscillations, but moderate and periodic oscillations that lead to the fatigue of the structure. Several comprehensive reviews such as Bearman (1984), Sarpkaya (2004), Williamson and Govardhan (2004), Vandiver (2012) have covered the fundamentals of vortex shedding and vortex-induced vibrations extensively.

2.3 One-degree-of-freedom vortex-induced vibrations

Vortex-induced vibrations typically occur in ocean engineering structures such as mooring lines, towing cables and tethering lines. These are long flexible structures which undergo VIV at different flow velocities. Not only the structures are complex and flexible, but also the flow in the ocean is not uniform and well-defined, but it is mainly sheared. Such system properties make the VIV studies for ocean structures very complex. One simplification used in studying VIV in such scenarios is to focus on the fluid-structure interaction around a very small section of such large flexible cylinders. In doing so, the structure can be assumed to be a rigid but flexibly mounted cylinder, placed in uniform flow (Figure 2.4).

Circular cylinders placed in flow experience drag and lift forces acting in two perpendicular directions: The streamwise (inline) and the transverse (crossflow) directions, respectively. Due to the symmetry of the circular cross-section the mean value for the lift force is zero. As a consequence of periodic vortex shedding, the lift and drag forces have a periodic component as well. When vortices shed in the wake of a circular cylinder, the forcing frequency in the crossflow direction (CF) is equal to the frequency of vortex shedding. This happens since one vortex is being shed from each side of the cylinder per

cycle. However, in the inline direction (IL), the shedding of both vortices has the same effect on the cylinder, and therefore the periodic drag force has a frequency twice the vortex shedding. If the structure has two degree-of-freedom it will oscillate in both CF and IL directions with the frequencies associated with the lift and drag forces, respectively. In general the amplitude of oscillations in the inline direction is much smaller than that in the crossflow direction (Williamson and Govardhan, 2004). On this basis, the primary simplified models focus on restricting the motion of the cylinder to a single degree of freedom in the crossflow direction. This representation is a simple mass-spring-dashpot system in which the cylinder has a mass *m*, the elastic mount has a spring constant *k*, and a damping constant *c* is used to model the structural damping.

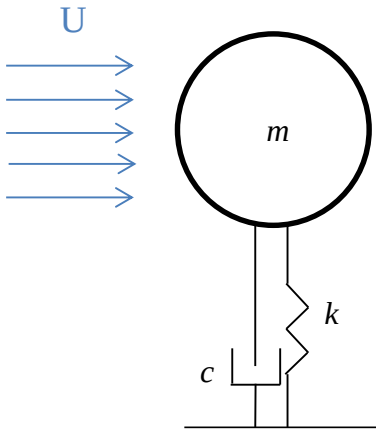

Figure 2.4. Schematic of a rigid circular cylinder with one degree-of-freedom subjected to flow.

The equation of motion generally used to represent the oscillations of a cylinder in the transverse direction, *y*, is the linear equation of a mass-spring-dashpot system, which is subjected to an external periodic force due to the flow as:

$$m\ddot{y} + c\dot{y} + ky = f_y, \tag{2.3}$$

where, m is the mass per unit length of the cylinder, y is the cylinder position measured from rest and f_y is the corresponding periodic lift force. The fluctuating lift force can be expressed in terms of the dimensionless lift coefficient C_y where:

$$C_y = \frac{f_y}{\frac{1}{2}\rho U^2 DL}. \tag{2.4}$$

Assuming that the cylinder's displacement has a sinusoidal form:

$$y(t) = y_0 \sin(\omega_{osc} t), \tag{2.5}$$

in which, ω_{osc} is the oscillation frequency of the cylinder, the flow force in the crossflow direction will have a phase difference φ with respect to the motion of the cylinder as

$$f_y(t) = f_0 \sin(\omega_{osc} t + \phi). \tag{2.6}$$

From equations (2.3)-(2.6), the non-dimensional amplitude and frequency can be derived as (Govardhan and Williamson, 2000):

$$A^* = \frac{1}{4\pi^3} \frac{C_y \sin\phi}{(m^* + C_A)\zeta} \left(\frac{U^*}{f^*}\right)^2 f^*, \tag{2.7}$$

$$f^* = \sqrt{\frac{m^* + C_A}{m^* + C_{EA}}}. \tag{2.8}$$

In these equations,

$$A^* = \frac{A}{D}, \tag{2.9}$$

is the dimensionless amplitude (A is the amplitude of oscillations),

$$f^* = \frac{f_{osc}}{f_N}, \tag{2.10}$$

is the dimensionless frequency (f_{osc} is the frequency of oscillations and f_N is the natural frequency of the system in water),

$$U^* = \frac{U}{f_N D}, \tag{2.11}$$

is the reduced velocity and the mass ratio, which is the ratio of the cylinder mass (or moving mass) to the mass of the displaced fluid (m_d) is defined as:

$$m^* = \frac{m}{\frac{1}{4}\pi\rho D^2 L}, \tag{2.12}$$

in which,

$$m_a = C_A m_d, \tag{2.13}$$

is the added mass and $m_d = \pi\rho D^2 L/4$ is the displaced fluid mass. C_A is the potential added mass coefficient in otherwise still fluid. A nominal value for the added mass (C_A) is usually assumed to be 1 based on the potential flow assumption. The effective added mass coefficient is defined as

$$C_{EA} = \frac{1}{2\pi^3}\frac{C_y \cos\phi}{A^*}\left(\frac{U^*}{f^*}\right)^2, \tag{2.14}$$

which includes the effect due to the total transverse fluid force in-phase with the body acceleration ($C_y\cos\varphi$), and

$$\zeta = \frac{\delta}{\sqrt{(2\pi)^2 + \delta^2}}, \tag{2.15}$$

is the structural damping (δ is the logarithmic decrement). Table 2.1 summarizes the parameters used in this Thesis.

Table 2.1. Nomenclature

Amplitude ratio (A*)	$A^* = \frac{A}{D}$
Frequency ratio (f*)	$f^* = \frac{f_{osc}}{f_N}$
Damping ratio (ζ)	$\zeta = \frac{\delta}{\sqrt{(2\pi)^2 + \delta^2}}$
Reynolds number (*Re*)	$\mathrm{Re} = \frac{UD}{\upsilon}$
Strouhal number (*St*)	$St = \frac{f_v D}{U}$
Normalized reduced velocity (U_n*)	$U_n^* = \frac{U\cos\theta}{f_N D}$
Reduced velocity (U^*)	$U^* = \frac{U}{f_N D}$
True reduced velocity (U_r)	$U_r = \frac{U}{f_{osc} D}$
Lift coefficient (C_L)	$C_L = \frac{F_L}{\frac{1}{2}\rho U^2 DL}$
Drag coefficient (C_D)	$C_D = \frac{F_D}{\frac{1}{2}\rho U^2 DL}$
Mass ratio (*m**)	$m^* = \frac{m}{\frac{1}{4}\pi\rho D^2 L}$
Potential added mass coefficient (C_A)	$m_A = C_A m_d$
Effective added mass coefficient (C_{EA})	$C_{EA} = \frac{1}{2\pi^3}\frac{C_Y\cos\phi}{A^*}\left(\frac{U^*}{f^*}\right)^2$
Phase angle (ϕ°)	$\phi° = \tan^{-1}\left[\frac{2\zeta\frac{f}{f_N}}{1-\left(\frac{f}{f_N}\right)^2}\right]$

Previous studies have shown that the dynamic response of the system varies dramatically depending on the mass-damping parameter of the system, which is defined as $m^*\zeta$ (see equations (2.12) and (2.15)). In the following sections, the response of the system with high and low mass-damping parameter is discussed.

2.3.1 Response regimes in one-degree-of-freedom system

The very first VIV experimental studies were conducted in wind tunnels with relatively high mass ratios ($m^*>100$), resulting in large mass-damping parameter. These experiments were mainly focusing on understanding the VIV of the structures in wind such as bridges and chimneys. On the other hand, experiments conducted on structures placed in water are mainly considered as low mass ratio systems. Such structures are more realistic models of marine and offshore structures which are usually in the range of low mass ratios of $m^*<10$ (Khalak and Williamson, 1997a).

In the experimental work conducted by Feng (1968), VIV of a circular cylinder placed in wind tunnel test section with a high mass-damping parameter of $m^*\zeta = 0.36$ was studied. Figure 2.5 shows the non-dimensional amplitude and non-dimensional frequency (non-dimensionalized with diameter of the cylinder and natural frequency of the system in air, respectively) plotted against reduced velocity. As shown in the figure, for very small reduced velocity values ($U^*<5$), the cylinder is stationary and the vortex shedding frequency (f_V) follows the straight line of Strouhal number ($St = 0.198$), similar to the fixed cylinder. By increasing the flow velocity, the vortex shedding frequency (f_V) approaches the natural frequency (f_N) of the system and the vortex shedding frequency substantially departs from the Strouhal frequency of a stationary cylinder. At this velocity ($U^*\approx5$), the

cylinder starts oscillating in the crossflow direction. In fact, the vortex shedding gets locked-in with the natural frequency of the cylinder and collapses into a single frequency. This phenomenon is known as "lock-in" during which the frequency of vibrations can shift considerably away from the natural frequency due to changes in the value of the effective added mass (Williamson and Govardhan, 2004). The maximum amplitude of 0.55D (D is the cylinder diameter) was achieved at a reduced velocity around $U^* \approx 6.3$. A hysteresis effect was observed during which two branches of the cylinder response existed, depending on the initial displacements of the cylinder: the upper branch with higher amplitudes of oscillations was associated with increasing flow velocities, while the lower branch was obtained when the flow velocity was decreased.

The phase difference φ between the flow force and the cylinder displacement in the crossflow direction is also plotted in Figure 2.5 for a uniform cylinder in Feng's experiments. As depicted, by increasing the reduced velocity, the phase difference shifted from 0° to 180° where the phase difference of 0° corresponds to the initial branch response and the phase difference of 180° is associated with the lower branch response.

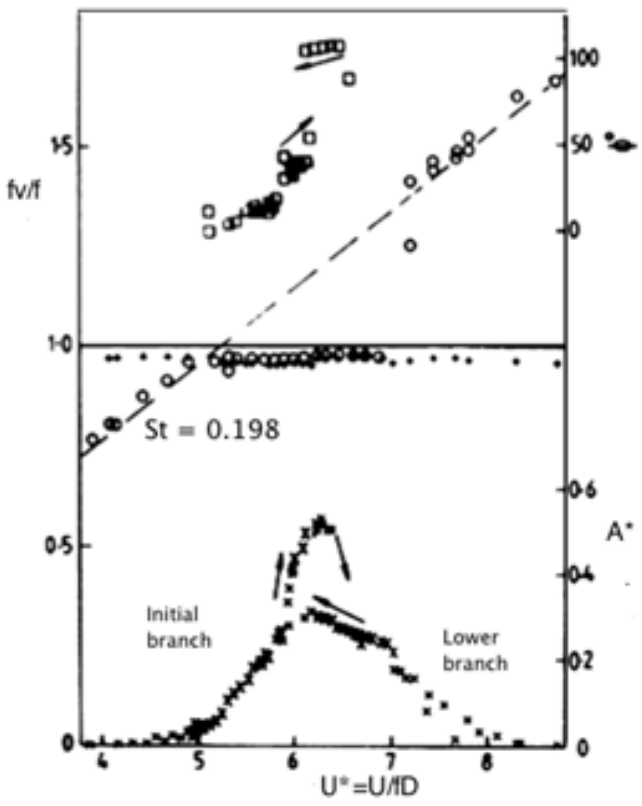

Figure 2.5. Response of a freely vibrating circular cylinder in air with m*ζ ≈ 0.36. o, vortex-shedding frequency; +, cylinder frequency; □, phase angle; ×, amplitude of oscillations (Khalak and Williamson, 1999).

Khalak and Williamson (1997b) studied the VIV of flexibly mounted cylinder with very low mass-damping parameter ($m^*\zeta = 0.013$) - almost an order of magnitude smaller than previously conducted experiments such as Feng (1968). The effect of $m^*\zeta$ on the system's response can be seen in Figure 2.6 where Khalak and Williamson (1997b) and Feng (1968) data are plotted. As $m^*\zeta$ becomes smaller (3% of Feng's value), the lock-in range increases by four fold and higher peak amplitudes are observed (twice the peak amplitude of Feng's experiment). Another important observation is the appearance of a third branch called the "upper branch" in the low mass-ratio case compared to the high

mass-ratio case in which only two branches (initial and lower) were seen as in Feng's results.

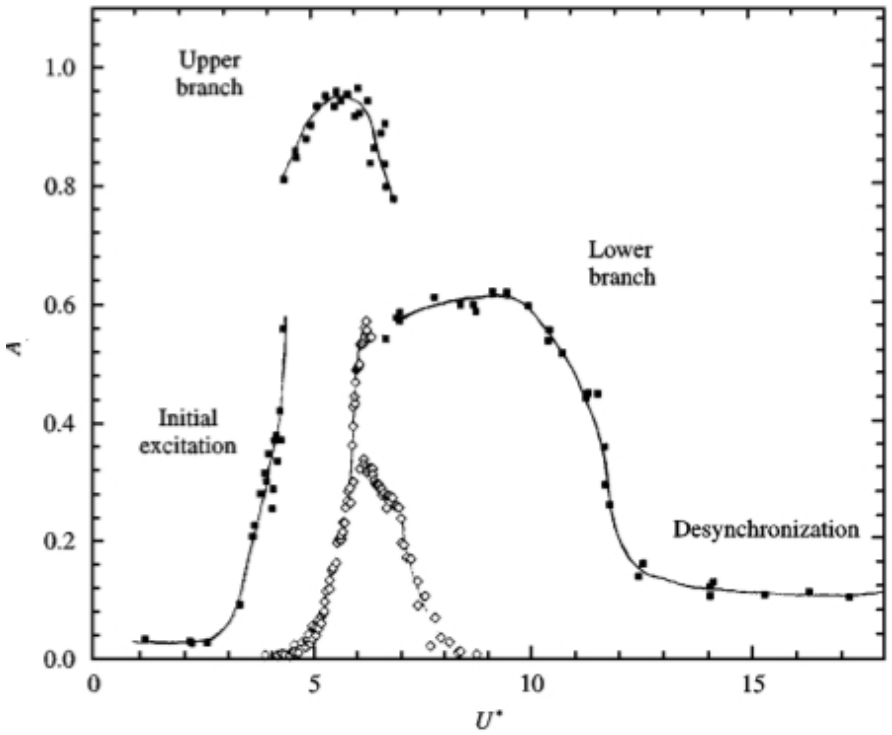

Figure 2.6. The amplitude response of flexibly mounted cylinder (■) Khalak and Williamson (1997b) with m*ζ = 0.013 in water and (◊) Feng (1968) with m*ζ = 0.36 in air (Khalak and Williamson, 1997b).

Khalak and Williamson (1997a) showed that the maximum amplitude of oscillations is influenced by the system properties such as the value of $m^*\zeta$, which controls the magnitude of peak amplitude in the upper branch whereas the lower branch response seems to be independent from the mass-damping parameter.

2.3.2 Fluid forces in low mass-damping systems

The lift and drag forces acting on the cylinder have been measured experimentally by Khalak and Williamson (1997b) as shown in Figure 2.7 for m^*=10.1. Measured flow

forces are made dimensionless by normalizing the forces by $\frac{1}{2}\rho U^2 DL$, where L and D are the immersed length and the diameter of the cylinder respectively, ρ is the fluid density, and U is the flow velocity.

As shown in Figure 2.7 the lift and drag forces are small at low reduced velocities associated with initial branch in amplitude response. For larger reduced velocities, both drag and lift forces reach their maximum values at a reduced velocity around U^*=4.5. The jump between the initial branch and upper branch can be associated with the sharp peak in the lift coefficient, which occurs at the transition from the initial branch to the upper branch. Furthermore, by increasing the reduced velocity, the flow forces decrease gradually and finally at high reduced velocities around U^*=9, where the system exits the lock-in range, the lift force becomes very small. Similar trends have been observed experimentally and numerically for other systems with different mass-ratio values (Bearman, 1984; Sarpkaya, 2004; Williamson and Govardhan, 2004; Wu et al., 2012).

2.3.3 Wake around the cylinder

Different vortex shedding patterns were identified by Williamson (1988) and later by Williamson and Govardhan (2004) in the wake of an oscillating circular cylinder. The amplitude of oscillations has been plotted in Figure 2.8 versus the "true reduced velocity" (Table 2.1) in which the velocity has been normalized with respect to the diameter of the cylinder and the frequency of oscillations. It has been observed that when the amplitude of oscillations is plotted with respect to the true reduced velocity, the response of the systems with different mass-damping parameter values collapse almost to a single plot as shown in Figure 2.8 (Khalak and Williamson, 1999). By plotting the amplitude response on top of

the map of wake modes in Figure 2.8, it was found that there exists a close relation between the vortex shedding patterns and amplitude response branches for circular cylinders. It was mainly concluded that the initial branch in amplitude response corresponds to a 2S vortex shedding (two single vortex sheddings per period of oscillation) and the upper branch corresponds to a 2P pattern (two pairs of vortices per period of oscillation). Figure 2.9 shows the 2S and 2P vortex shedding patterns shown for the first time in experiments of Williamson and Govardhan (2004).

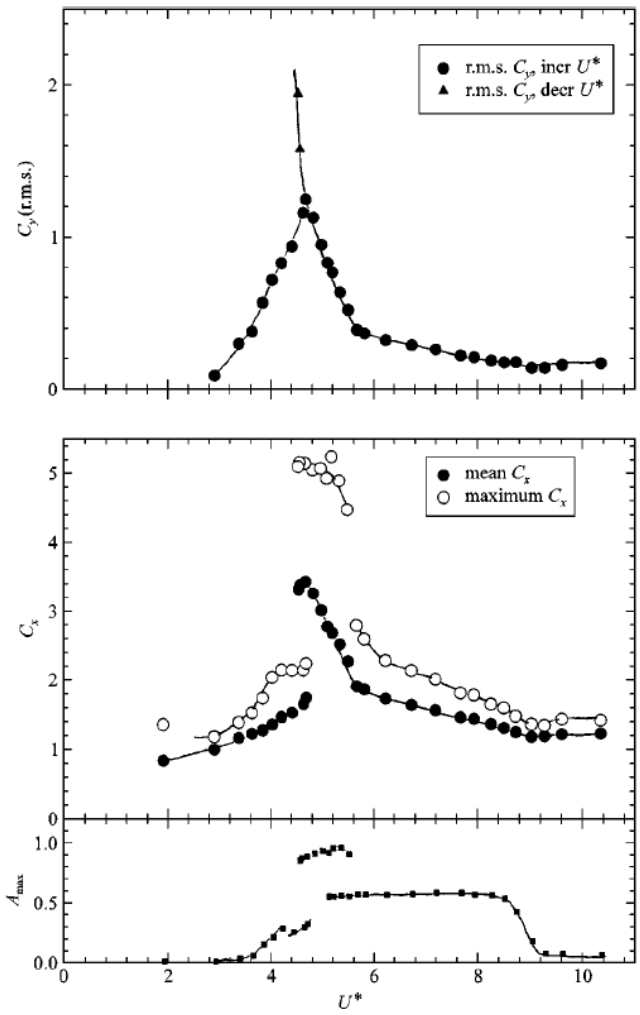

Figure 2.7.Measured lift coefficient CL and drag coefficient CD versus reduced velocity U* for m*=10.1 and m*ζ= 0.013 (Khalak and Williamson, 1997b).

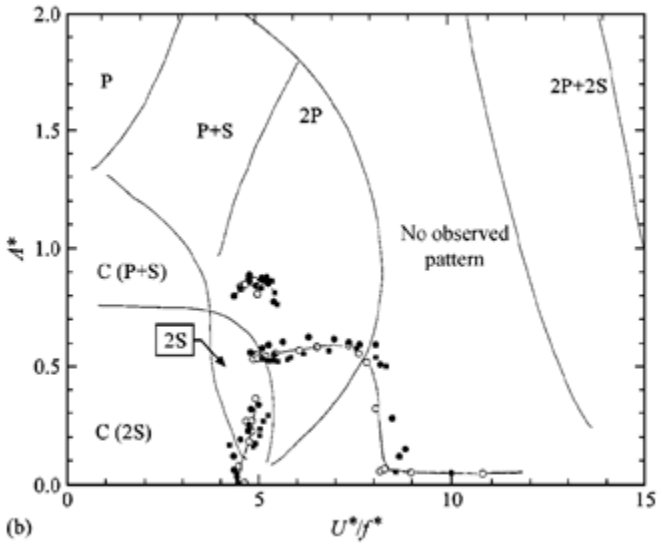

Figure 2.8. Amplitude response on top of the wake mode map versus true reduced velocity (Khalak and Williamson, 1999).

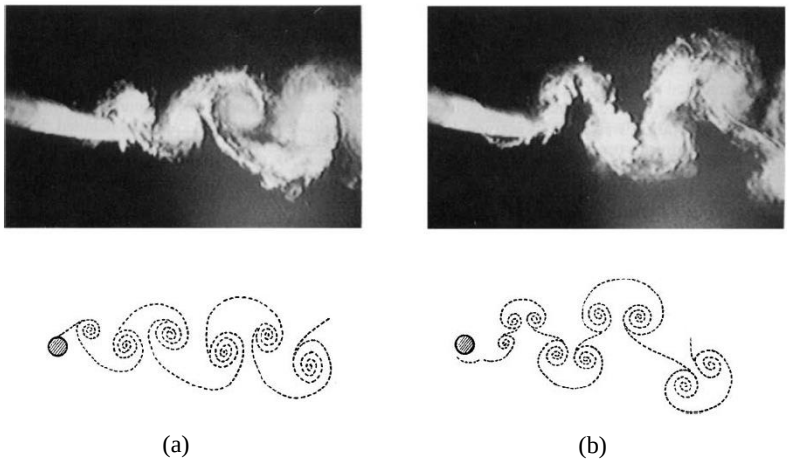

Figure 2.9. Vortex shedding patterns for (a) 2S, (b) 2P pattern (Williamson and Govardhan, 2004).

2.4 Two degree-of-freedom vortex-induced vibrations

Despite the widespread use of the 1 DOF models for VIV, most engineering structures under flow forces are free to oscillate in both the inline and the crossflow

directions. The important question is then how the motion in the inline direction changes the response of the system and the wake of the cylinder? The answer to this question is addressed in studies by Sarpkaya (2004), Dahl et al. (2006), Dahl et al. (2007), Jauvtis and Williamson (2004), Jeon and Gharib (2001) in which they have shown that substantial differences exist when the rigid cylinder is allowed to move in the inline (IL) direction in addition to the crossflow (CF) oscillations. Inclusion of the IL motion leads to significant changes in hydrodynamic forces acting on the rigid cylinder, depending on the phase difference between the IL and the CF vibrations (Dahl et al., 2006; Dahl et al., 2007). It was observed that the forces in the CF direction are substantially different from the case in which the oscillations were limited to the crossflow direction. Fluid forces at high frequencies compared to the oscillation frequency and more specially at frequencies equal to the integer multiples of the vibration frequency, i.e. higher harmonics, have been observed in experimental measurements of rigid circular cylinders (Dahl et al., 2007) which are subjected to VIV in both the CF and the IL directions. Such high frequency loading has a direct impact on the structural fatigue damage and may lead to catastrophic failure of civil or ocean engineering structures (Dahl et al., 2007; Mukundan et al., 2009).

The interesting point about the two-dimensional oscillations is the influence of the ratio of the natural frequencies in these two directions on the observed response of the system. Dahl et al. (2007) has experimentally varied the frequency ratios in the inline and crossflow directions in a range from 1 to 2 and has shown that the perfect vortex shedding resonance in 2D systems occurs when the effective natural frequency of the system in the inline direction is twice that in the transverse direction. This is due to the fact that in the inline direction, the fluid force from the vortex shedding excites the system with the

frequency two times the one in the crossflow direction. In this connection, the cylinder motion follows the orbital shapes with figure-eight patterns or crescent-like shapes with a frequency of oscillations f in the crossflow direction and $2f$ in the inline direction. Figure 2.10 shows different trajectories of the cylinder in 2D domain of varying frequency ratios and nominal reduced velocities. As it is observed, the trajectories are different in shape for different reduced velocities as a consequence of varying phase angles between the inline and crossflow motions. Varying phase between the motions in these two directions can be explained by different added masses achieved in different conditions depending on the system parameters. Fluid force higher harmonic contributions are also observed in this case as shown by colorful contours in Figure 2.10. Large values of fluid force higher harmonics were observed when the dual resonance happens at frequency ratio of 1.9.

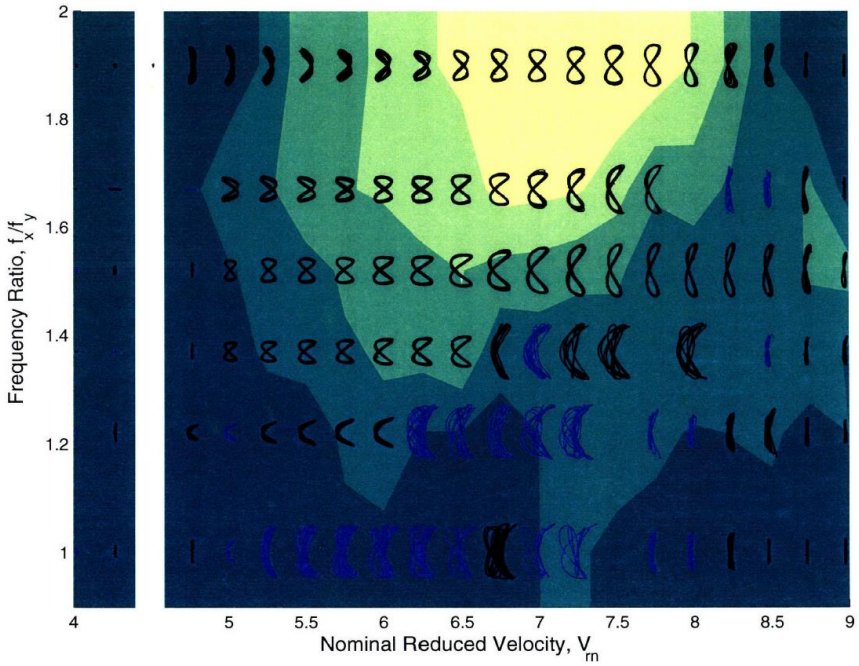

Figure 2.10. Orbital trajectories for a circular cylinder in a 2D set-up with varying crossflow and inline frequencies (Dahl et al., 2007).

2.5 VIV in Flexible cylinder

As mentioned previously, assuming the system to be a rigid cylinder, flexibly mounted and free to oscillate either in one or two directions is a simplified assumption of the flexible structures used in real world applications such as long risers, towing cables and mooring lines in the deep water subjected to ocean currents.

A long slender cylinder with a series of natural frequencies may have different modes excited in the inline (IL) and crossflow (CF) directions, since IL vibrations excited by vortex shedding are at a distinct frequency from that of the CF vibrations. In the lock-in range, the mode might switch as a consequence of fluctuation in the flow speed or changes in the tension along the cylinder (Vandiver et al., 2009). As a consequence of multi-modal and multi-frequency oscillations of long flexible structures subjected to flow, the VIV investigations of such structures are more complex. In recent years, several experimental investigations such as Kaasen et al. (2000), Vandiver et al. (2009), Chaplin et al. (2005a), Chaplin et al. (2005a), Trim et al. (2005), Huera-Huarte and Bearman (2009a) have studied the VIV of vertical circular cylinders. Long slender structures in ocean are subjected to complex flow profiles. The VIV studies of such structures mainly consider a sheared flow profile. Consequently, the lock-in behavior and the VIV response of the system will change along the length of the structure since each location might be excited with a different shedding frequency, resulting in a mode-competition along the length of the cylinder. Studies by Lucor et al. (2001), Mukundan et al. (2009), Bourguet et al. (2011a), Bourguet et al. (2012) have shed light on some VIV aspects of slender structures in sheared flow. Multi-mode resonance, large higher harmonic fluid forces and travelling waves are among the characteristics of such systems. Figure 2.11 shows the

spanwise evolution of the trajectories in a flexible cylinder subjected to sheared flow (Bourguet et al., 2011a). Since each part of the cylinder is subjected to a different flow velocity, there are some parts of the cylinder which are not in lock-in condition as shown by the red-dashed line. The criterion used to study the occurrence of the lock-in is the matching between the vortex shedding frequency and frequency of oscillations. Three-dimensionality introduced to the system and consequently different spanwise responses add to the complexity of VIV study in such structures. More details about the VIV response of flexible cylinders will be discussed in Chapter 7 of this thesis.

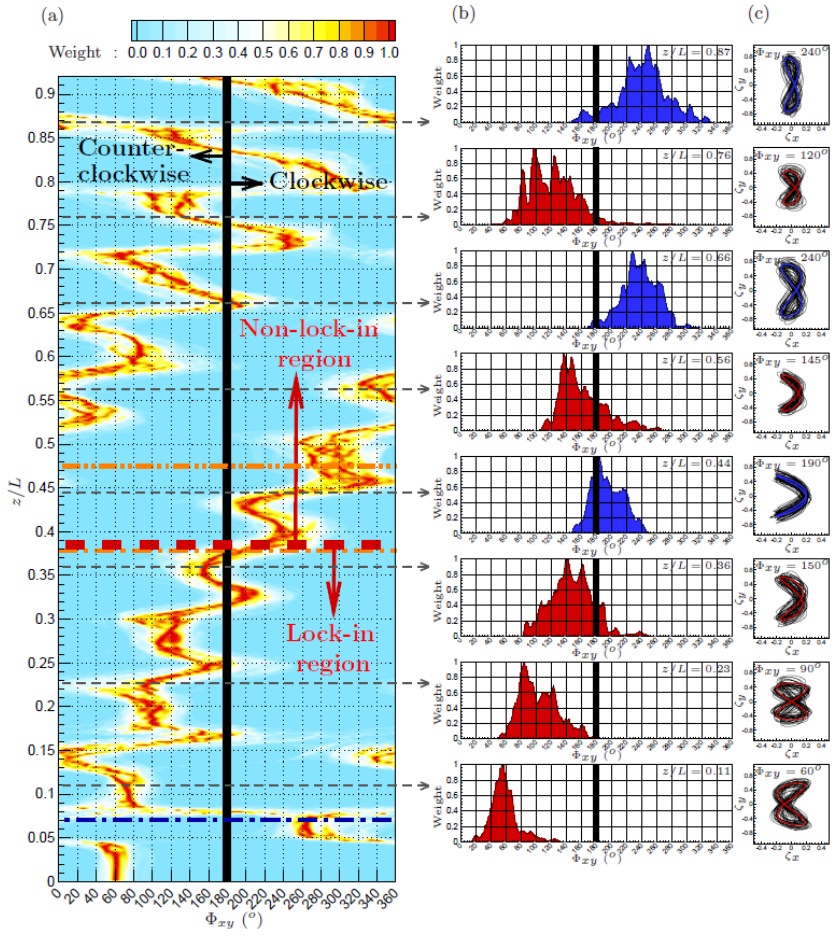

Figure 2.11. Spanwise evolution of phase difference between the IL and CF displacements (a) numerical simulations, (b) experiment (Bourguet et al., 2011b).

2.6 Motivation and objectives

In most VIV studies already discussed, the system under study is symmetric. This symmetry is defined either at the boundary conditions of the structure, the surrounding flow or the geometry of the structure. Such symmetric conditions make the VIV modeling and analysis much easier. However, in most real world applications, system loses its symmetry. For instance, a vertical uniform circular cylinder has symmetric geometry owing to the symmetric circular cross section all along its length. The resulting vortex shedding at each cross-section of the cylinder is also symmetric. If the cylinder is placed at an angle with respect to the incoming flow (an inclined cylinder), if its diameter varies along its length (a tapered cylinder), if its angle of inclination is varied continuously along its length (a curved cylinder) or if it has a triangular cross-section instead of a circular (triangular cylinder), then the geometrical symmetry of the system is broken. This broken symmetry will result in a different shedding in the wake, which in turns results in a different response of the system. If the cylinder is forced to rotate about its long axis, its wake will be pushed sideways, which in turns breaks the symmetry of flow forces that act on the structure.

The goal of this thesis is to study the VIV response of such systems and shed light on the influences of different symmetry breaking conditions on the VIV response of the systems that will be discussed in the following chapters.

CHAPTER 3

THE INFLUENCE OF TAPER RATIO ON THE VORTEX-INDUCED VIBRATIONS OF TAPERED CYLINDERS IN THE CROSSFLOW DIRECTION[1]

3.1 Introduction

Vortex-induced vibration (VIV) of a circular cylinder with a constant diameter placed normal to the flow has been studied extensively for a flexibly-mounted rigid cylinder (Bearman, 1984; Sarpkaya, 2004; Williamson and Govardhan, 2004; Vandiver, 2012). Here, VIV of a tapered cylinder – a cylinder in which the cross-sectional area varies continuously along its length – is considered.

The wake of a tapered cylinder placed in uniform flow has been studied widely for a fixed cylinder in flow. Gaster (1969, 1971) conducted the first series of experiments to study the wake of a fixed tapered cylinder placed in uniform flow. His work was continued by Papangelou (1992), Piccirillo and Van Atta (1993), and later Hsiao and Chiang (1998). Valles et al. (2002) used computer simulations and reproduced the laminar vortex shedding behind a linearly tapered cylinder observed experimentally by Piccirillo and Van Atta (1993). Several studies have used direct numerical simulations to understand the vortex

[1] The results discussed in this chapter have been published in the J. Fluids Struct. B. Seyed-Aghazadeh, D. Carlson, Y. Modarres-Sadeghi, " The influence of taper ratio on the vortex-induced vibrations of tapered cylinders in the crossflow direction".

shedding behind tapered cylinders at low Reynolds numbers (Provansal and Monkewitz, 2006; Parnaudeau et al., 2007; Narasimhamurthy et al., 2009) and some have used stereo-PIV (Visscher et al., 2011). Vortex dislocations, cellular shedding and oblique shedding are the major phenomena discussed in the studies of a fixed tapered cylinder placed in flow.

The dynamics of an oscillating tapered cylinder, however, has received less attention. Techet et al. (1998) conducted a series of tests on a tapered cylinder with a taper ratio of 40:1 where the taper ratio was defined as the ratio of the cylinder length to the difference between the maximum and minimum diameters of the cylinder. The cylinder was forced to oscillate in the transverse direction and towed in a towing tank. They observed both 2S (two single vortices per oscillation) and 2P (two pairs of vortices per oscillation) vortex shedding in the wake of the cylinder as well as a new "hybrid" shedding, which consisted of a 2S shedding in the range of the cylinder with larger diameter, and a 2P shedding in the range of the cylinder with smaller diameter. Hover et al. (1998) continued this work by conducting a series of experiments on a flexibly-mounted tapered cylinder with the same taper ratio, and confirmed the validity of the forced VIV tests to predict the amplitude of oscillations and the phase between the lift and the displacement. They also found that the lock-in range in the tapered cylinder started at a slightly lower value for the nominal reduced velocity (reduced velocity defined based on the natural frequency of the structure).

Balasubramanian et al. (2001) studied VIV of a pivoted tapered circular cylinder placed either in a uniform or sheared flow, and noted the differences of the resulting lock-in range with the case of a pivoted uniform cylinder. Their experimental investigation

revealed the importance of the relative orientation of the sheared flow gradient with respect to the orientation of the tapered cylinder. They also related the different amplitudes of vibrations to the mass distribution of the tapered cylinder along its length. Since the tapered cylinder in their study was hinged with unequal mass distribution along the length, the results were found to be very sensitive to the relative direction of the cylinder with respect to the incoming flow.

Zeinoddini et al. (2013) conducted VIV tests on tapered cylinders with two different taper ratios. A comprehensive study of the influence of the taper ratio was not possible in their tests, since the cylinders with two taper ratios had two different mass ratios. They observed a wider lock-in range for the tapered cylinders, compared with the uniform cylinders. They also tested the tapered cylinders with a pure inline motion and did not observe any significant difference in the amplitude of oscillations compared with the case of a uniform cylinder.

In the present thesis, a series of tests are discussed on four tapered cylinders, placed in flow and free to oscillate in the crossflow direction (i.e., in the transverse direction). Three of the cylinders had linear taper, in which the diameter of the cylinders varied linearly from one end to the other end, with three different taper ratios, and the fourth cylinder had a nonlinear taper. A series of tests on a uniform cylinder were conducted as well, to have a basis for comparison. To be able to draw conclusions on the influence of the taper ratio, the mass ratio and the structural damping were kept constant in all these cases. Tests were conducted with and without end plates and with the cylinder in two

orientations (smaller diameter in the top or in the bottom) to study the influence of the boundary conditions on the resulting response of the cylinder.

3.2 Experimental set-up

Four tapered cylinders were considered in the experiments. Three of them had a linear taper with taper ratios of 29:1 (Cylinder L_1), 17:1 (Cylinder L_2) and 10:1 (Cylinder L_3), where the taper ratio is defined as $\tau = (L/D_{max}–D_{min})$, in which L is the cylinder length, and D_{max} and D_{min} are the maximum and minimum diameters, respectively. The fourth cylinder had a nonlinear taper (Cylinder *N*), in which the cylinder's diameter, D, varied along its length from D_{min} to D_{max} as $z(D) = 0.003D^2–0.0196D+0.201$, where z is the spanwise length of the cylinder. All cylinders had the same length, L = 30 cm. A uniform cylinder (Cylinder *U*) was also used in the experiments in order to have a basis for comparison. Table 3.1 summarizes the properties of the cylinders. The experiments were carried out in a re-circulating water tunnel, with a test section of 1.27 m×0.5 m×0.38 m, a turbulence intensity of less than 1% for up to a flow velocity of V = 0.3 m/s and a velocity uniformity of less than 2%.

The set-up used to hold the cylinder in the test section had two air bearings to reduce the damping and constrain the oscillations of the cylinder to one degree of freedom in the crossflow direction (Figure 3.1). This set-up was used previously by Jain and Modarres-Sadeghi (2013) to study VIV of inclined cylinders. Springs were attached from the supporting plate used for mounting the cylinder to a fixed housing. The top 1 cm of the cylinder was not submerged. A Micro-Epsilon ILD 1402-600 non-contacting motion sensor was used to record displacement data of the oscillating cylinder. Decay tests in water

and air were performed to obtain the natural frequencies in water, f_{nw}, and in air, f_{na}, as well as the damping ratios of the system for each cylinder (Table 3.2). The mass ratio of the cylinder was calculated as $m^* = m/\rho V_{cyl}$, where m is the total moving mass of the system, ρ is the flow density, and V_{cyl} is the total cylinder volume. The total mass of the system included the mass of the cylinder and the moving objects such as the air bearings and the supporting plate. Schematics of the five cylinders used in the experiments are given in Figure 3.2.

Table 3.1. Physical properties of the cylinders used in the experiments

	Average diameter (mm)	*Taper ratio*	*Mass ratio (without the end plate)*	*Mass ratio (with the end plate)*
Linearly tapered cylinder (L1)	15.3	29:1	6.5	7.6
Linearly tapered cylinder (L2)	15.8	17:1	6.2	7.3
Linearly tapered cylinder (L3)	20.4	10:1	6.7	7.3
Nonlinearly tapered cylinder (N)	14.4	–	6.2	7.6
Uniform cylinder (U)	14.6	∞	6.4	7.7

To study the wake dynamics of the cylinder, dye flow visualizations were performed around the cylinder at various reduced flow velocities for the tapered cylinders free to oscillate in the crossflow direction. A mixture of dye and sugar was used to create a caramel-like blend to cover the overall length of the cylinder. The coated cylinder was placed in the test section, and the dye was slowly washed down into the wake of the cylinder.

Table 3.2. Natural frequencies in water, f_{nw}, and in air, f_{na}, as well as the damping ratios of the system for each cylinder

	In Water		*In air*	
	Natural frequency (Hz)	Damping ratio	Natural frequency (Hz)	Damping ratio
Linearly tapered cylinder (L1)	0.47	0.039	0.52	0.004
Linearly tapered cylinder (L2)	0.47	0.029	0.50	0.003
Linearly tapered cylinder (L3)	0.33	0.031	0.37	0.004
Nonlinearly tapered cylinder (N)	0.53	0.021	0.57	0.004
Uniform cylinder (U)	0.5	0.023	0.53	0.005

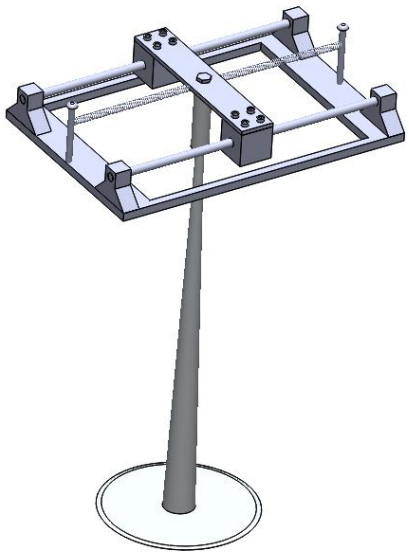

Figure 3.1. Schematic of the experimental set-up.

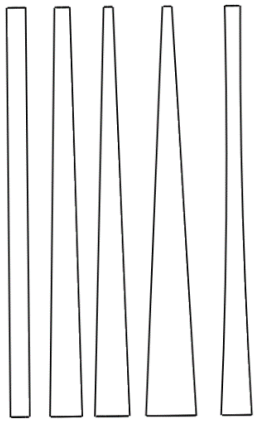

Figure 3.2. Schematic of the cylinders used in the experiments. Cylinders from left to right: U, L_1, L_2, L_3, N.

3.3 Linearly Tapered Cylinders

3.3.1 Amplitude and frequency of oscillations

The first series of tests were conducted using all three cylinders of Figure 3.2 with a linear taper (Cylinders L_1, L_2 and L_3). Each cylinder was placed vertically in the test section in a way that its smaller diameter was placed at the top, close to the water surface. A circular end-plate with a radius of 5.5 cm and a thickness of 2 mm was attached to the lower end of the cylinder, as suggested by Morse et al. (2008). The edges of the end-plate were streamlined to avoid flow separation. The mass ratio for all these cylinders was approximately $m^* = 7.5$ (See Table 3.1 for the exact values). Figure 3.3 shows the dimensionless amplitude, $A^*=A/D$, and frequency, $f^*=f/f_{nw}$, of oscillations versus the reduced velocity, $U^*=U/f_{nw}D_{\text{ave}}$, where f is the measured frequency of oscillations in Hz, U is the dimensional flow velocity in m/s and D_{ave} is the average diameter of the linearly tapered cylinder in m. The linearly tapered cylinders were made such that the average

diameter for all of them was approximately D_{ave} = 15 mm, so the ratio between the length and the average diameter of the cylinders was kept at a constant value of L/D_{ave} = 20.

In order to have a basis for comparison, the amplitude and frequency of oscillations were measured for a uniform cylinder with the same parameters (m^* and L/D) as the linearly tapered cylinders. The results obtained here for the uniform vertical cylinder (Figure 3.3) matched very well with what Khalak and Williamson (1999) have reported in terms of the trend for the amplitude and frequency of oscillations.

Figure 3.3(a) shows the dimensionless amplitude of oscillations versus the reduced velocity for all cases. It is observed that the results for the large taper ratio of 29:1 (the closest case to the uniform cylinder) and the uniform cylinder are very similar. The location of the maximum amplitude as well as the lock-in range was almost the same for these two cases, implying the fact that for larger taper ratios, the cylinder behaves very similarly to a uniform cylinder. As the taper ratio was decreased (i.e., a larger difference between the minimum and the maximum radii), the lock-in range shifted to the right (higher reduced velocities) and its width increased. The maximum amplitude of oscillations stayed at a constant value of around A^*=0.7 for all three taper ratios, close to the maximum amplitude for a uniform cylinder.

The dominant frequency of oscillations normalized by the natural frequency in water, $f^*=f/f_{nw}$ (Figure 3.3b) remained at almost a constant value close to unity during the lock-in range for all cylinders with different taper ratios. For reduced velocities larger than those in the lock-in region, the cylinder did not oscillate, and therefore no frequency of oscillations is reported for these reduced velocities in Figure 3.3(b).

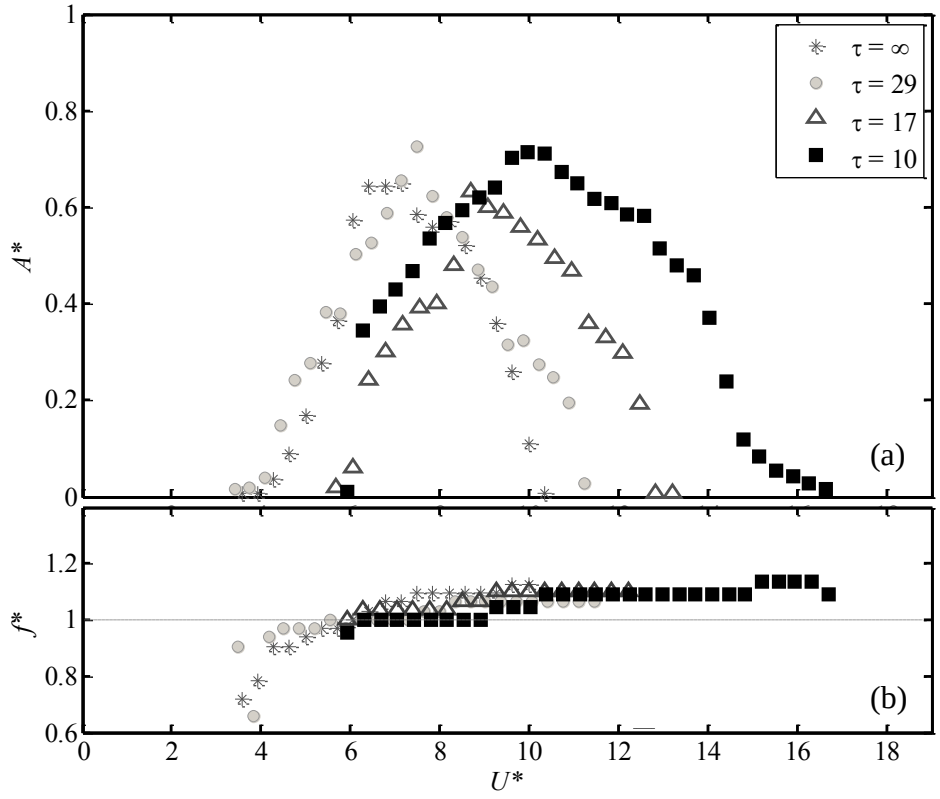

Figure 3.3. Dimensionless (a) amplitude ($A^*=A/D_{ave}$) and (b) frequency ($f^*=f/f_{nw}$) of the crossflow oscillations versus the reduced velocity ($U^*=U/f_{nw}D_{ave}$) for three different tapered cylinders and a uniform cylinder with a circular end-plate attached to their lower end.

3.4 The wake

Figure 3.4 shows the cylinder wake at 6 different reduced velocities within the lock-in range for the linearly tapered cylinder with a taper ratio of 17:1 (L_2). The reduced velocities are chosen such that the entire lock-in range is covered. A hybrid shedding, consisting of 2S vortex shedding in the range with larger diameters, and 2P vortex shedding in the range with smaller diameters was observed for some cases. Figure 3.5 shows the 2S

and 2P vortex shedding, respectively, for the linearly tapered cylinder with taper ratio of 17:1 (L_2) at two different locations along the span of the cylinder at a fixed reduced velocity of V_r =7.1, for which a hybrid vortex shedding pattern was observed. The points were chosen at heights of z/L=0.1 and z/L=0.7 where z is measured from the lower end of the cylinder. The observed hybrid vortex shedding pattern is in agreement with the flow visualizations conducted by Techet et al. (1998) for a cylinder with a tapered ratio of 40:1.

The hybrid shedding was observed for reduced velocities smaller than the reduced velocity at which the maximum amplitude occurred. For higher reduced velocities, 2P vortex shedding was observed for the entire length of the cylinder. Also, as it is shown in Figure 3.4, the splitting point, at which the 2S and 2P vortex patterns collided (highlighted by dashed lines in the figure), changed its location along the length of the cylinder by increasing the reduced velocity. The splitting point shifted downward from the cylinder's midpoint toward its lower end (Figure 3.4a-d). This drift in the splitting point suggests that by increasing the reduced velocity, the spanwise length of the cylinder in which the 2S shedding occurs, becomes smaller and the 2P shedding prevails the vortex shedding mechanism at higher reduced velocities. On this basis, at reduced velocities larger than the value associated with the maximum amplitude of oscillations, the entire length of the cylinder was being excited by the 2P shedding pattern (Figure 3.4e-f). This observation is also consistent with an estimated range for the 2S shedding discussed in the following paragraph.

For a tapered cylinder undergoing VIV, there is a region along the length of the cylinder for which a 2S vortex shedding pattern is observed. This region can be estimated

as the region for which $f^* = f D/U$ (where f is the principal frequency of vibration) is in the neighborhood of $f^* = 0.20$, which corresponds to the region of maximum energy transfer from the flow to the structure. Here, $f_1^* = 0.15$ and $f_2^* = 0.25$ have been considered as the limits for estimating the excitation region. For a tapered cylinder observing a constant incoming flow velocity, U, and oscillating at a constant frequency, f, the dimensionless frequency varies along the length due to the change in the cylinder diameter. The points along the cylinder whose corresponding dimensionless frequencies are equal to f_1^* and f_2^* are then calculated as $L_1 = L\, D_1/(D_{max} - D_{min})$ when $D_1 = f_1^* U / f$ and $L_2 = L\, D_2/(D_{max} - D_{min})$ when $D_2 = f_2^* U / f$. Then, the excitation region can be found as $\Delta L = L_1 - L_2$.

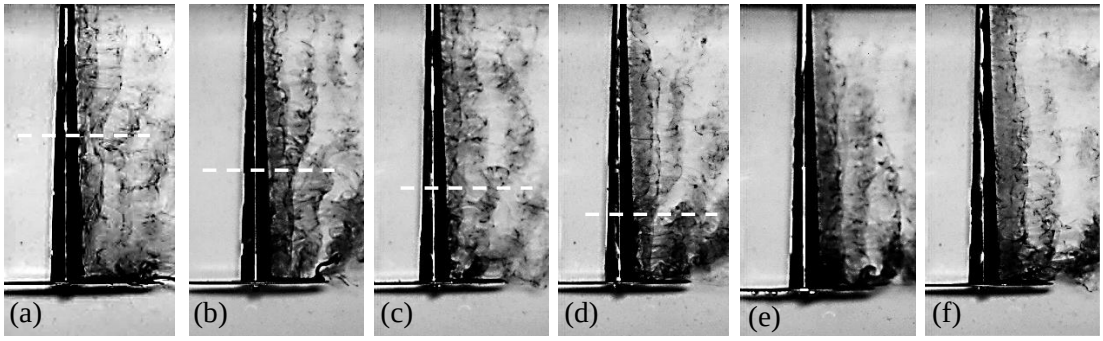

Figure 3.4. Flow visualizations for the linearly tapered cylinder with a taper ratio of 17:1 (Cylinder L_2) at reduced veloicties of (a) U^*=6.4, (b) U^*=7.1, (c) U^*=7.9, (d) U^*=8.7, (e) U^*=9.6 and (f) U^*=11. The dashed lines show the splitting points.

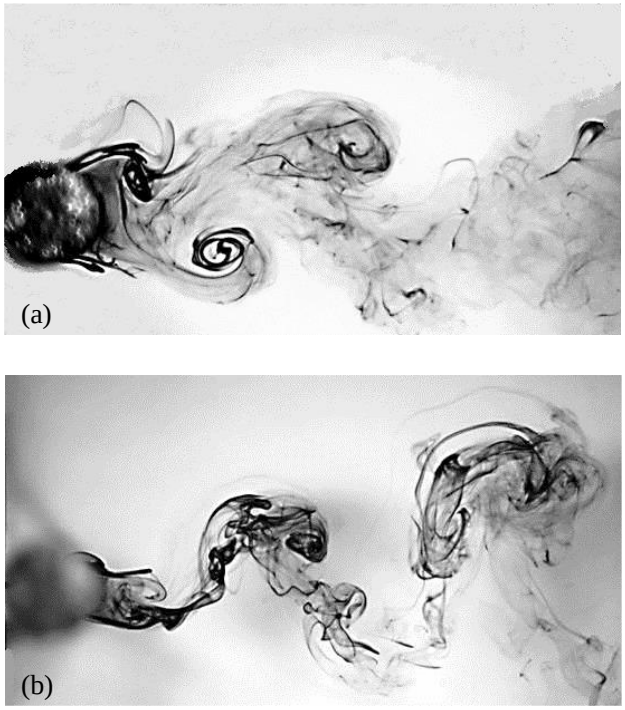

Figure 3.5. The (a) 2S and (b) 2P shedding at two differenet poins along the length of a linearly tapered cylinder (Cylinder L_2) at (a) x=0.1, (b) x=0.7 at the reduced velocity of U^*=7.1, where a hybrid shedding is observed.

Figure 3.6 shows the regions for which a 2S vortex shedding is estimated following this assumption for the three linearly tapered cylinders discussed in this thesis. For all cases, the region for 2S shedding starts at smaller diameters of the cylinder and moves toward regions with larger diameters, at higher reduced velocities. The lock-in regions and the locations of the maximum amplitude for each taper ratio based on the experimental results are shown in the figure as well. In all three cases the predicted 2S shedding starts at the beginning of the lock-in region and vanishes for reduced velocities higher than the values corresponding to the maximum amplitude of oscillations for each cylinder. This was also observed in the flow visualization tests on the tapered cylinders, as discussed above. For the tapered cylinder with a taper ratio of 17:1 (L_2), the observed experimental locations

of splitting points are plotted in Figure 3.6(b). These points follow the upper limit of the predicted 2S shedding very nicely.

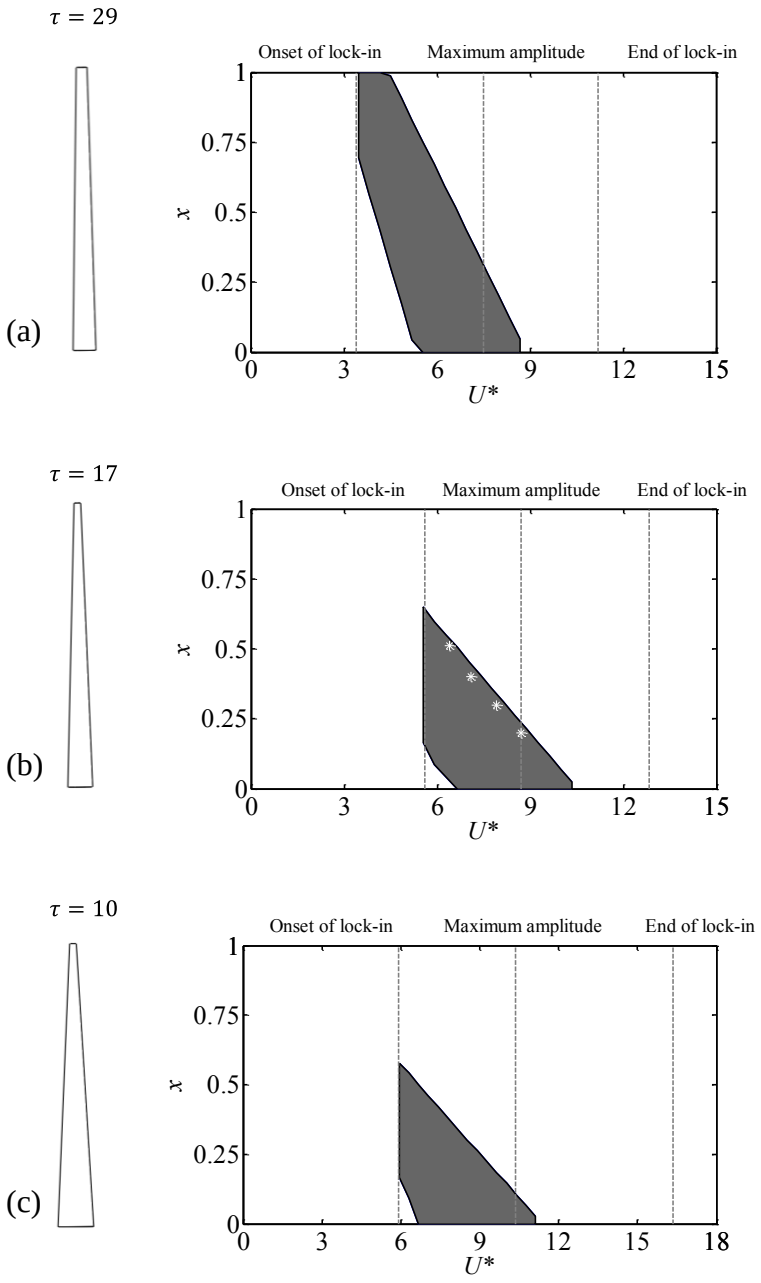

Figure 3.6. Schematic of the ranges of 2S vortex shedding versus the reduced velocity for the three linearly tapered cylinders.

3.5 Forces

In order to calculate the flow forces acting on the cylinder in the crossflow direction, it is assumed that the structure can be modeled as a single-degree-of-freedom system, which is a widely accepted assumption (e.g., Eqn (1) in Khalak and Williamson (1999)):

$$\ddot{y} + 2\zeta\omega_n\dot{y} + \omega_n^2 y = f_y \ , \tag{3.1}$$

in which ζ is the structural damping, ω_n is the natural frequency of the structure measured in air, and *y* is the measured displacement of the cylinder in the crossflow direction. Once the displacement is measured, then the total fluid force can be calculated by calculating the left-hand side of Equation (1). In order to show the validity of this method, forces obtained using Equation (3.1) for a uniform cylinder are compared with forces measured directly from a force sensor. A six-axis force sensor (ATI- Nano17/IP68) was mounted on top of the oscillating cylinder and measured the total flow forces acting on the cylinder in all directions, including the crossflow direction. The measured force from the sensor comprised both the hydrodynamic flow forces and the inertia force due to the motion of the force sensor. Thus, the inertia force was removed from the total measured force by post-processing the experimental data. The force sensor measurements were synchronized with the displacement data from the non-contacting displacement sensor, making it possible to directly compare the measured flow forces with the flow forces calculated using Equation (1). Figure 3.7 shows that the crossflow force coefficient calculated using both methods are in agreement in terms of both the magnitude and the phase difference between flow force and displacement. Also the maximum value for the transverse force coefficient,

C_y, matches very well with the results of Khalak and Williamson (1999) for a uniform cylinder with a similar mass-damping ratio.

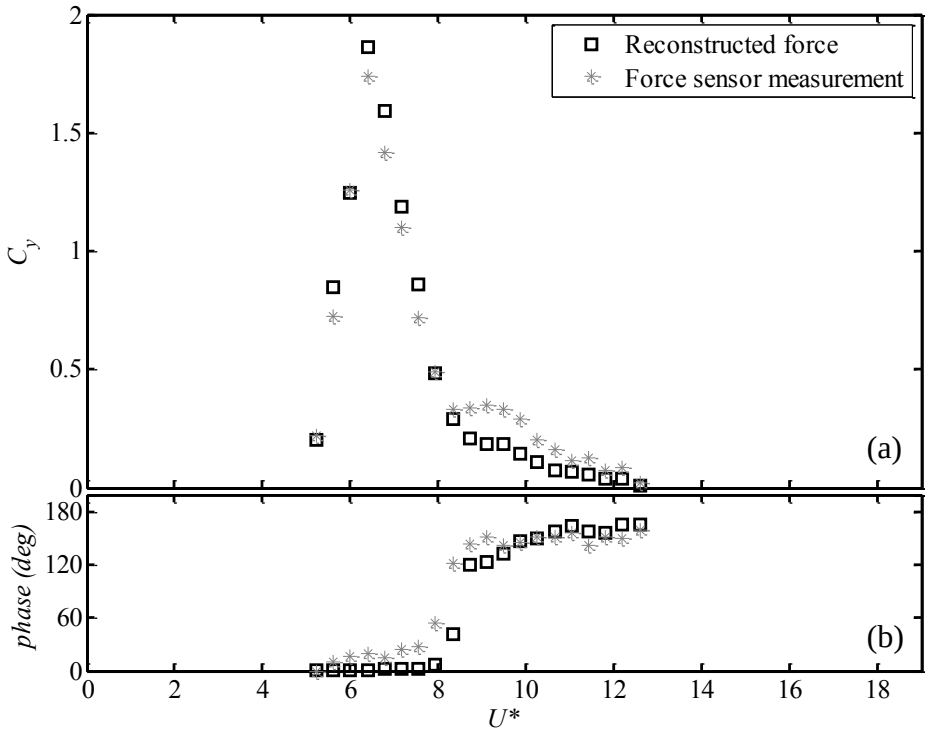

Figure 3.7. The (a) transverse flow force and (b) phase difference between the flow force and the displacement versus the reduced velocity for the uniform cylinder with mass-damping ratio of $m^*\zeta$=0.018: (□) Reconstructed force, (*) direct measurements from the force sensor set-up.

The resulting calculated forces using Equation (3.1) in the crossflow direction for the uniform cylinder (Cylinder *U*) as well as the tapered cylinder with a taper ratio of 17:1 (Cylinder L_2) are plotted in Figure 3.8(a). As shown in the figure, the flow forces on the tapered cylinder followed the same trend as the uniform cylinder, while the lock-in range was shifted to the higher reduced velocities for the tapered cylinder.

The phase differences between the flow force and the cylinder displacement in the crossflow direction are plotted in Figure 3.8(b) for Cylinders *U* and L_2. By increasing the

reduced velocity, the phase difference shifted from 0° to values close to 180° with almost the same trend for both cases. Khalak and Williamson (1999) observed the same trend in phase difference for a uniform cylinder and showed that the phase difference of 0° corresponds to the upper branch response and the phase difference of 180° is associated with the lower branch response. In the current experiment, the phase shift from 0° to 180° occurred at a reduced velocity around $U^*\approx 6$ for uniform cylinder, which coincided with the change from the upper branch response to the lower branch for the uniform cylinder. For the tapered cylinder, the phase shift occurred at $U^*\approx 9.5$, which was the reduced velocity at which the amplitude of oscillations reached its maximum value.

As shown in Figure 3.8(b) the shift in phase differences both for the uniform and tapered cylinder occurred gradually, following almost the same trend. The gradual shift from 0° to 180° is related to the structural damping of the system and the frequency of oscillations. A system with no structural damping would have experienced a sudden jump in phase from 0° to 180°. With a small structural damping, if the frequency ratio stays close to unity over a range of reduced velocities (which is the case here both for the tapered and uniform cylinder as shown in Figure 3.8(c)), the phase shift from 0° to 180° occurs more gradually than the cases in which the frequency ratio is farther from unity[2].

[2] As a reminder, the phase difference can be written as $\theta = \tan^{-1}\dfrac{2\zeta\left(f/f_{na}\right)}{1-\left(f/f_{na}\right)^2}$.

3.6 A Nonlinearly Tapered Cylinder

Besides the linearly tapered cylinders discussed in the previous section, a nonlinearly tapered cylinder, in which the cylinder's diameter varied along its length from D_{min} to D_{max} as $z(D) = 0.003D^2–0.0196D+0.201$, was used to study the influence of the nonlinear taper on the resulting crossflow VIV. The nonlinear cylinder was designed such that the average value of its maximum and minimum diameters, $(D_{max}+D_{min})/2$, was equal to the average diameter of the linearly tapered cylinders discussed in Section 3.3.

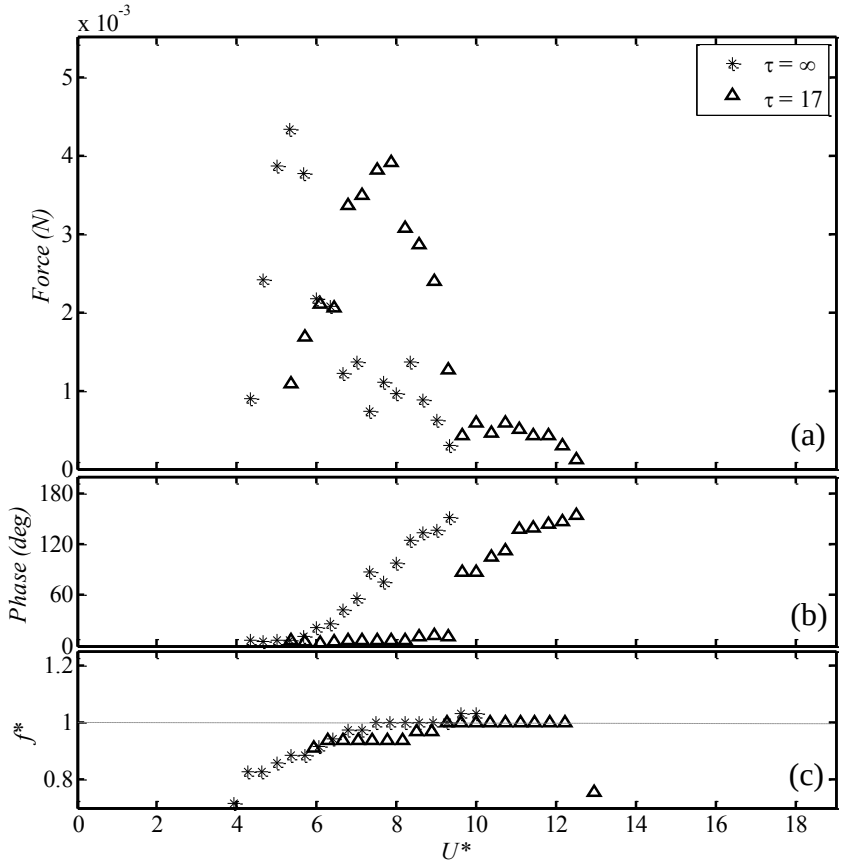

Figure 3.8. The (a) flow forces in the crossflow direction, (b) phase difference between the flow force and the displacement and (c) frequency ($f^*=f/f_{na}$) of the crossflow oscillations versus the reduced velocity for the uniform cylinder U (*) and a linearly tapered cylinder L_2 (Δ).

Tests similar to the ones discussed in the previous section were conducted on this nonlinearly tapered cylinder. The amplitude of oscillations versus the reduced velocity for this cylinder is plotted in Figure 3.9 together with the results for two of the linearly tapered cylinders. The average diameter for the nonlinearly tapered cylinder used in the dimensionless velocity and amplitude of oscillations was calculated by taking the average value of all diameters along the length of the cylinder. The mass ratio of the nonlinearly tapered cylinder was $m^* = 10.2$ and in order to compare its results with the linearly tapered cylinders, a new series of tests were conducted in which a dummy mass was added on top of the linearly tapered cylinders so that the mass ratios of all the cylinders were adjusted to be $m^* = 10.2$. The maximum amplitude of oscillations for the nonlinearly tapered cylinder was about $A^*=0.55$. The maximum amplitudes observed are lower than the ones in the previous section, as a result of a higher mass ratio (10.2 instead of 7.5). The lock-in range for the nonlinearly tapered cylinder was narrower compared with the linearly tapered cylinders and it was shifted toward the higher reduced velocities.

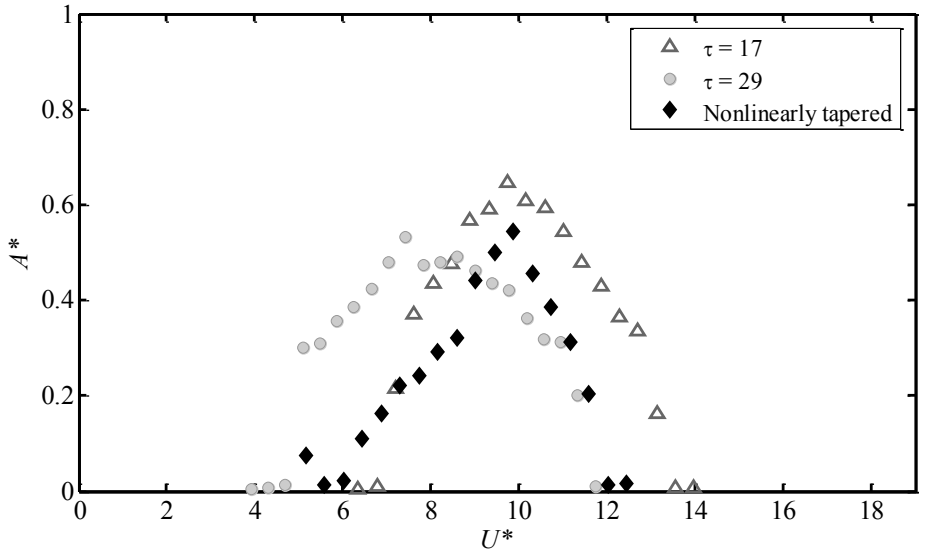

Figure 3.9. Dimensionless amplitude of the crossflow oscillations ($A^*=A/D_{ave}$) versus the reduced velocity ($U^*=U/f_{nw}D_{ave}$) for the cylinder with a nonlinear taper and two of the linearly tapered cylinders (Cylinders L_1 and L_2) with a circular end-plate attached to their lower end.

3.7 Inverted Configurations

In the tests discussed in the previous sections, the tapered cylinder was placed in the test section of the water tunnel such that its upper end had the smaller diameter and its lower end, the larger diameter. The tests were repeated with inverted configurations (the larger diameter in the top) in other to study if the boundary conditions were affecting the observed vortex shedding and the corresponding oscillations. Figure 3.10 shows the lock-in ranges for the tapered cylinders in their inverted configurations. For convenience, negative taper ratios are used for these cases. For example, τ = –17 corresponds to the inverted configuration of the cylinder with a taper ratio of 17:1 (τ = 17). As shown in Figure 3.10, the amplitudes of oscillations for the negatively tapered cylinders followed a

trend similar to those for the positively tapered cases: For smaller taper ratios, the onset of lock-in range was shifted to the higher values of reduced velocities and the lock-in width was larger.

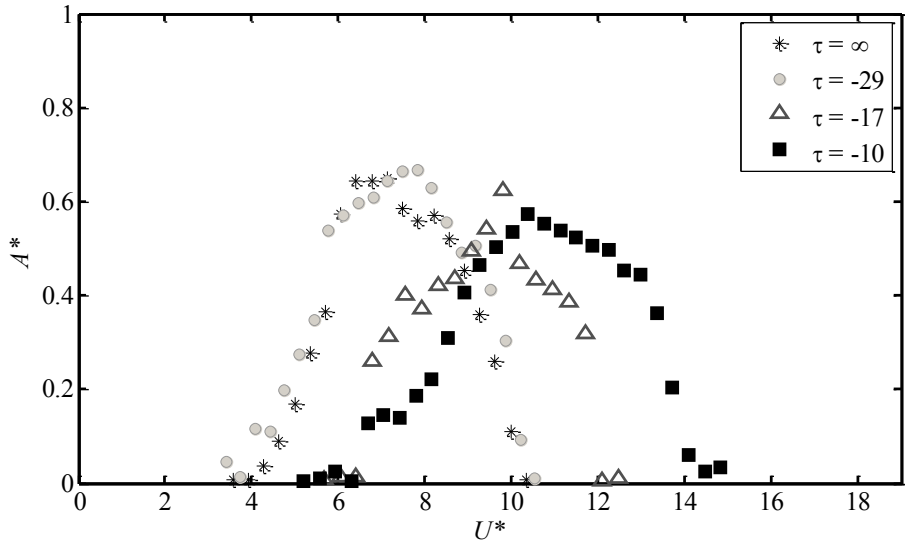

Figure 3.10. Dimensionless amplitude ($A^*=A/D_{ave}$) of the crossflow oscillations versus the reduced velocity ($U^*=U/f_{nw}D_{ave}$) for three different negatively tapered cylinders with a circular end-plate attached to their lower end.

There was a slight decrease in the maximum amplitude of oscillations for the cylinders with a negative taper compared with the cylinders with a positive taper (Figure 3.11). This deviation increased by decreasing the taper ratio, and can be addressed by looking at the excitation regions along the length of the cylinder for the positive and negative taper ratios as follows. For the inverted cylinder (negative taper), at higher reduced velocities, the 2S excitation region was located close to the water surface, while for the positively tapered cylinders, it was located close to the lower end of the cylinder (Figure 3.6). The upper 1 cm of the cylinder was out of the water in the tests discussed here, which means that the cylinder's excitation region in water was smaller for the

negatively tapered cylinders compared with the positively tapered cases, which leads to the decrease in the maximum amplitude of oscillations for the inverted cylinders observed in Figure 3.11.

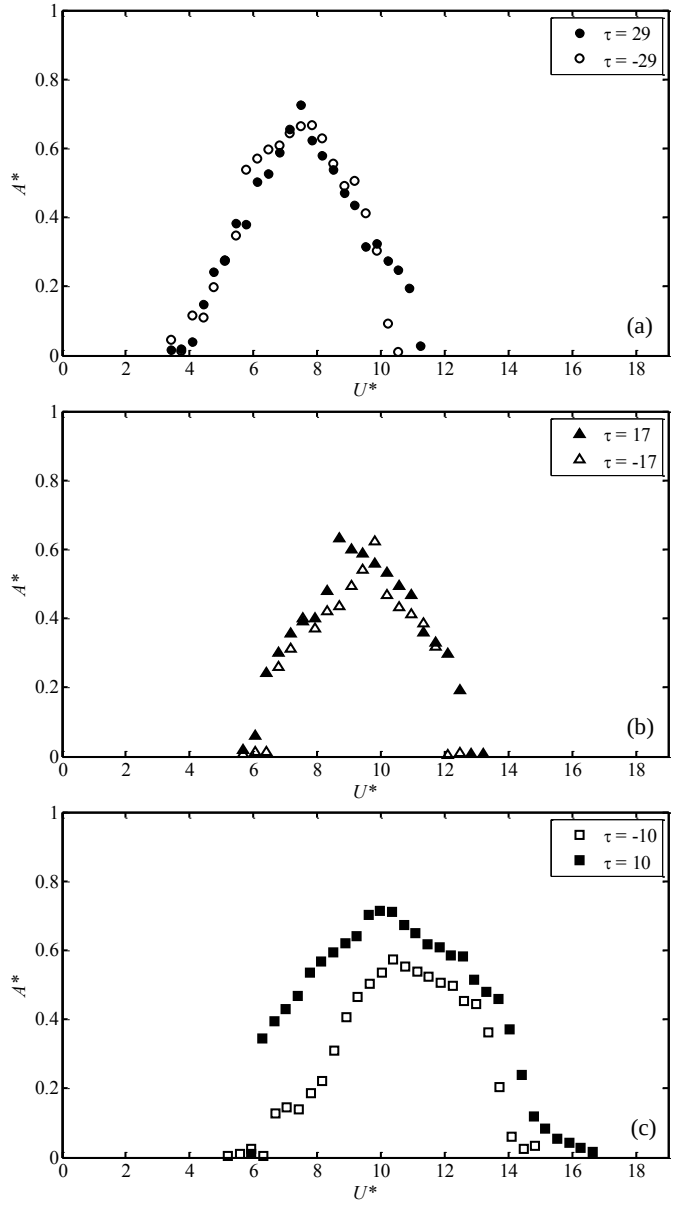

Figure 3.11. Dimensionless amplitude ($A^*=A/D_{ave}$) of the crossflow oscillations versus the reduced velocity ($U^*=U/f_{nw}D_{ave}$) for positive and negative tapers for (a) tapered cylinder, L_1, (b) tapered cylinder, L_2, and (c) tapered cylinder, L_3, with a circular end-plate attached to their lower end.

Flow visualizations were conducted for several cases of the inverted configuration. Figure 3.12 shows a sample result for a cylinder with a taper ratio of 17:1 at a reduced velocity of U^*=7.1 for both the positive and negative configurations. The hybrid shedding mode was observed for the inverted configuration as well as the positively tapered cylinder. The splitting point occurred at the same location (measured from the small-diameter end) for both positive and negative taper configurations. These results confirm that the hybrid mode is not a result of the cylinder's end effects; it is a generic feature of the VIV response of tapered cylinders at reduced velocities smaller than that corresponding to the peak amplitude of the response.

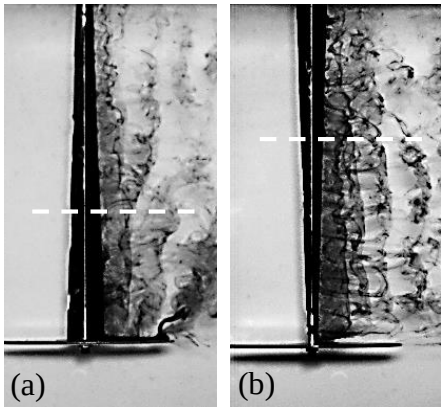

Figure 3.12. Flow visualizations for the linearly tapered cylinder L_2 at U^*=7.1 for (a) $\tau = 17$, (b) $\tau = -17$.

3.8 The Influence of the Lower End

In order to study the end effects, the response of the system was studied for cylinders with a free lower end (i.e., no end-plate was attached to the cylinder). Figure 3.13 shows the lock-in range for a uniform cylinder with and without the end-plate for a mass

ratio of $m^* = 7.5$. A dummy mass was added to the moving part of the cylinder with no end plate, so that the mass ratio of the two cases remained at a constant value of $m^* = 7.5$. As shown in Figure 3.13, adding the end-plate results in two distinct regions for the upper and lower branches, while in the case of a cylinder with no end-plate, the upper and lower branches appear as one single branch. This is in agreement with what Khalak and Williamson (1999) observed.

The tests then were extended to the tapered cylinders. Figure 3.14 shows the amplitude of oscillations versus the reduced velocity for two different tapered cylinders together with the uniform cylinder with no end-plate. There is no clear trend for the influence of the taper ratio on the resulting lock-in range, as opposed to the cases with an end-plate discussed in Section 3.3 and Figure 3.3. It seems that the lower end effects are so severe that they override the influence of the taper ratio, and no clear influence of the taper ratio can be observed in these cases.

Figure 3.15 shows flow visualizations for a uniform cylinder as well as a tapered cylinder at a reduced velocity of $U^*=7.1$, with and without the end plate. For both cylinders, without an end-plate, the vortex columns were disturbed at regions close to the lower boundary and relatively large tip vortices were formed at the lower end of the cylinder. By adding the end-plate, in the uniform cylinder vortex columns were shed parallel to its long axis for its entire length, and for the tapered cylinder, the disturbed shedding pattern at the lower end diminished.

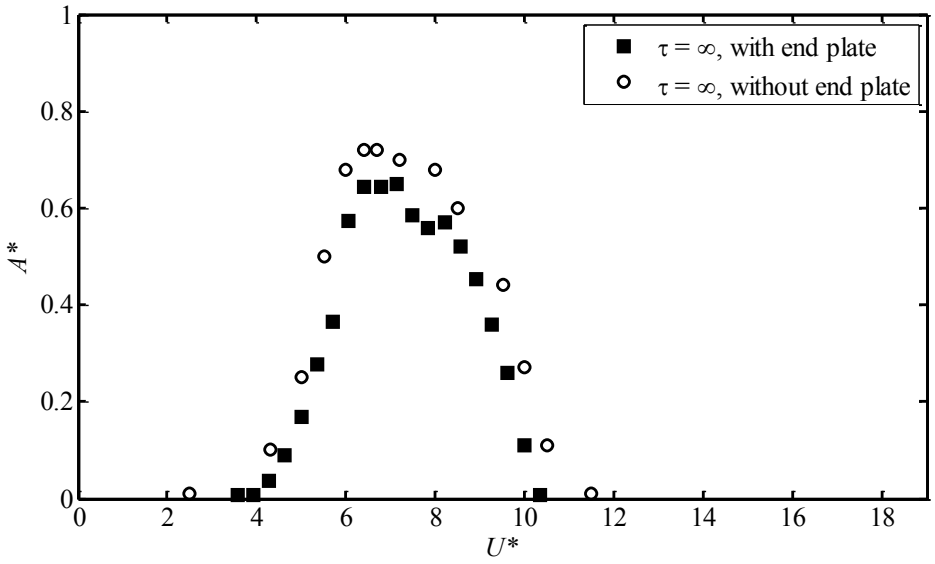

Figure 3.13. Dimensionless amplitude ($A^*=A/D_{ave}$) of the crossflow oscillations versus the reduced velocity ($U^*=U/f_{nw}D_{ave}$) for the uniform cylinder U with and without a circular end-plate attached to the lower end.

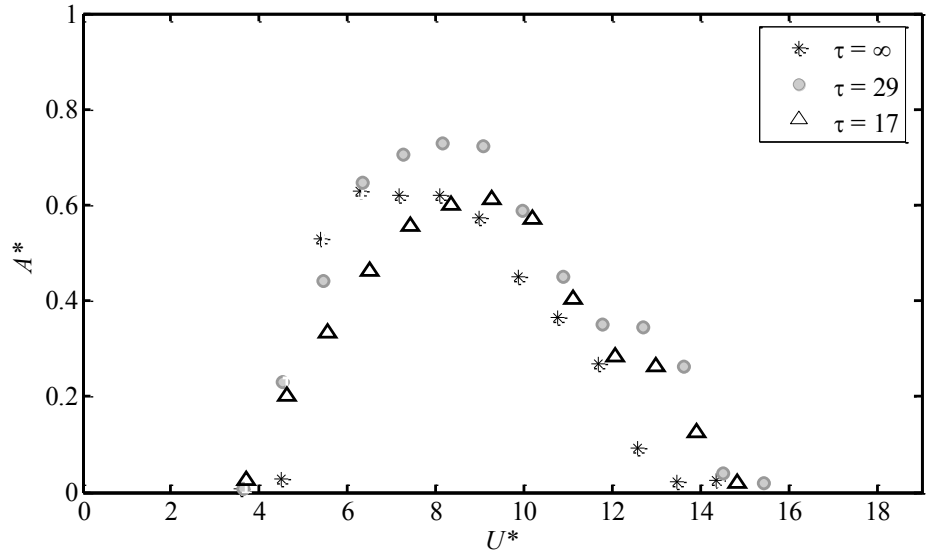

Figure 3.14. Dimensionless amplitude ($A^*=A/D_{ave}$) of the crossflow oscillations versus the reduced velocity ($U^*=U/f_{nw}D_{ave}$) for different tapered cylinders with no end-plate attached to their lower end.

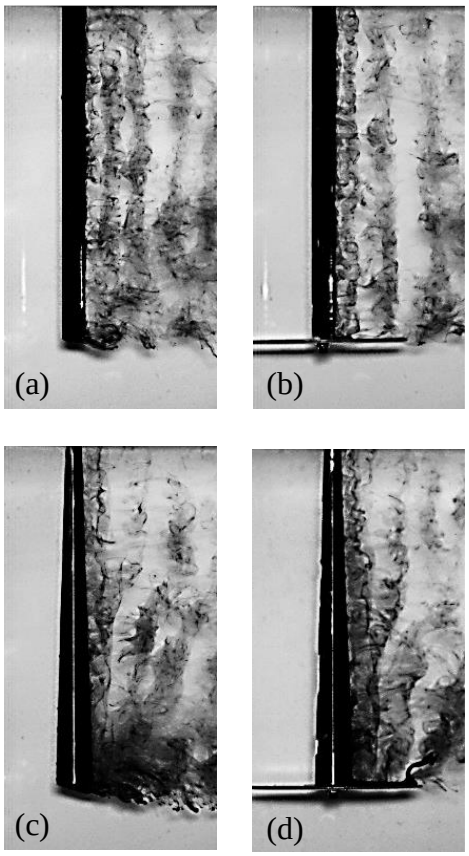

Figure 3.15. The wake of a (a) uniform cylinder without and (b) with an end-plate, as well as the wake of a (c) tapered cylinder, L_2, without and (d) with an end-plate at the reduced velocity of U^*=7.1.

3.9 Conclusions

Vortex-induced vibration of tapered cylinders free to oscillate in the crossflow direction was studied experimentally. The previous studies on tapered cylinders were focused on large taper ratios (cases closer to a uniform cylinder). By considering smaller taper ratios (cases with larger deviations from a uniform cylinder) in the present work, the influence of the taper ratio was more noticeable in the results. Three linearly and one nonlinearly tapered cylinders were considered. For linearly tapered cylinders, wider lock-

in ranges were observed compared with a uniform cylinder, and the lock-in range was shifted toward higher reduced velocities as the taper ratio of the cylinder decreased (i.e., a larger deviation from a uniform cylinder). The amplitude of oscillations for tapered cylinders stayed at a constant value around A^*=0.7. Hybrid vortex shedding modes, consisting of 2S shedding from the parts of the cylinder with larger diameters and 2P shedding from the parts of the cylinder with smaller diameters, were observed. It was observed that the splitting point, the point at which the 2S and 2P vortex columns collided, changed its position along the length of the cylinder at different flow velocities, starting from smaller diameters at lower reduced velocities to larger diameters at higher reduced velocities. The hybrid vortex shedding mode was observed for flow velocities up to the reduced velocity corresponding to the peak amplitude of oscillations. For larger flow velocities, 2P shedding was observed for the entire length of the tapered cylinders. In the range where the hybrid shedding was observed, the contribution of the 2S shedding decreased with increasing reduced velocity. It was shown that the region along the length of the cylinder with 2S vortex shedding can be estimated as a region in the neighborhood of $f^* = 0.20$.

The phase difference between the flow forces and the crossflow displacements for the tapered cylinders followed a trend similar to that for a uniform cylinder, shifting from 0º at low reduced velocities close to 180º at higher reduced velocities until the cylinder exited the lock-in range.

The tests were conducted both for the positively and negatively tapered cylinders. For the positively tapered cylinders, the vertical cylinder was placed such that its minimum

diameter was at its upper end, and it was inverted for the negatively tapered cylinder. The hybrid modes did exist for both configurations of the tapered cylinders; the splitting point occurred at the same location for both cases, and similar amplitudes of oscillations and lock-in ranges were obtained for the two orientations, suggesting that the observed results are independent from the boundary conditions and are intrinsic features of the tapered cylinders. Minor discrepancies in the amplitudes of oscillations for the positively and negatively tapered cylinders were related to the small part of the cylinder which was not immersed in flow.

CHAPTER 4

VORTEX-INDUCED VIBRATIONS OF A CURVED CIRCULAR CYLINDER IN THE CROSSFLOW DIRECTION[3]

4.1 Introduction

Vortex-induced vibration of a cylinder placed normal to the flow has been studied extensively, both for a flexibly-mounted rigid cylinder (Bearman, 1984; Sarpkaya, 2004; Williamson and Govardhan, 2004; Vandiver, 2012) and a flexible cylinder (Vandiver, 1993; Modarres-Sadeghi et al., 2011; Bourguet et al., 2012; Wu et al., 2012). In many real world applications, however, the cylinder is not placed perfectly perpendicular to the direction of the oncoming flow. In some cases, the cylinder makes a fixed angle with respect to the oncoming flow (an inclined cylinder) and in some other cases, the angle that the cylinder makes with the oncoming flow varies continuously along its length (a curved cylinder). There are several studies on a fixed (Vanatta, 1968; Ramberg, 1983; Thakur et al., 2004; Zhao et al., 2009) or a free-to-oscillate (Lucor and Karniadakis, 2003; Franzini et al., 2009; Jain and Modarres-Sadeghi, 2013) inclined cylinder placed in flow.

In a curved cylinder, the angle of inclination varies continuously along the length of the cylinder. The work by Takamoto and Izumi (1981) is among the first experimental

[3] The results discussed in this chapter have been submitted for publication in the J. Sound Vib. B. Seyed-Aghazadeh, C. Budz, Y. Modarres-Sadeghi**, "**The Influence of Higher Harmonic Flow Forces on the Response of a Curved Circular Cylinder Undergoing Vortex-Induced Vibration".

studies in which flow passing a curved structure was considered. Stable vortex rings were observed downstream of a fixed axisymmetric circular ring. Ahmed (2010) studied the wake dynamics of a cylinder with a mid-span curvature, experimentally. His observations showed that depending on the orientation of the structure with respect to the oncoming flow direction, varying vortex shedding patterns could be observed. A symmetric vortex shedding pattern was observed when the flow direction was toward the inner part of the curved structure (saddle attachment). Also, wake velocity profiles showed that the drag forces acting on the curved structure were highly dependent on the configuration of the curved section. For the saddle attachment, the drag forces were maximum and for nodal attachment, in which the flow first saw the outer part of the curved cylinder, the drag forces were minimum.

A curved cylinder (a quarter of a ring) can be considered in two different orientations: the convex orientation in which the upper end of the cylinder sees the flow first and the concave orientation in which the lower end of the cylinder sees the flow first (Figure 4.1(a)). Miliou et al. (2003), in their numerical study based on a spectral/*hp*-element Navier Stokes solver, investigated the dynamics of the flow past a quarter of a ring fixed in flow. Their results matched well the empirical findings of Takamoto and Izumi (1981) in terms of the vortex shedding patterns. Fully three-dimensional wake dynamics were observed for both the concave and the convex configurations. de Vecchi et al. (2009) performed a three-dimensional simulation for a curved cylinder in the convex orientation, forced to oscillate in the crossflow direction at a Reynolds number of Re=100. They showed that the flow was highly three dimensional as a result of the curvature of the structure. The cylinder used in their simulations featured a long horizontal extension

attached to the lower part of the cylinder. This part of the cylinder was parallel to the flow and acted as a slender body, rather than a bluff body, and therefore experienced drag-type forces. The component of the lift coefficient in phase with velocity, C_{Lv}, was negative for the entire length of the cylinder. They concluded that the horizontal extension acted like a hydrodynamic damper, ultimately resulting in a negative energy transfer, and therefore suppressing VIV. When they applied a rotating motion to the horizontal extension, the hydrodynamic damping was greatly reduced and the net energy transfer from the flow to the structure became positive ($C_{Lv}>0$), indicating that the flow could excite the structure. In the wake of the cylinder, the vortex columns were bent according to the curvature of the cylinder contrary to the case of the stationary cylinder in which the vortex columns remained straight (de Vecchi et al., 2008). Vortex dislocations were observed for the convex orientation at mid-span of the curved cylinder as a consequence of different shedding frequencies at the lower and upper parts of the cylinder. Assi et al. (2014) conducted a series of tests on a curved cylinder, placed in flow and free to oscillate in two perpendicular directions. Their set-up had a horizontal extension attached to the lower end of the curved cylinder, similar to the cylinder used by de Vecchi et al. (2009). They observed a reduction in the amplitude of oscillations both for the convex and the concave orientations, while the resulting amplitudes in the convex orientation were smaller than the amplitudes in the concave direction. They also conducted a series of flow visualizations on a fixed curved cylinder and observed that the distributed flow around the horizontal extension highly affects the response of the system.

In the present thesis, for the first time evidences of the higher harmonic flow forces in an oscillating curved cylinder are presented both for the concave and the convex

orientations. It is also shown how these higher harmonic forces influence the amplitude of the VIV response. These studies are based on a series of experiments on a curved circular cylinder free to oscillate in the crossflow direction for both the convex and the concave configurations. In the previous studies, often a horizontal extension was added to the lower end of the curved cylinder, mainly in the convex orientation, and sometimes even in the concave orientation. de Vecchi et al. (2009) showed that this axial extension introduces a flow-induced damping in the system, which affects the total response of the system. In the present experiments, we did not include this axial extension to avoid the resulting flow-induced damping.

4.2 Experimental set-up

A curved cylinder with a diameter of D=1 cm, which was a quarter of a ring with a radius of curvature of R=47 cm, was tested in the convex and the concave orientations (Figure 4.1(a)). The cylinder was built using 3D-printing technique. It was 3D printed out of ABS plastic in 4 pieces, assembled using epoxy, and coated. Dowel pins inserted between the pieces allowed the assembly to be aligned into a perfect quarter circle when laid on a flat surface. The cylinder was sanded and coated to ensure a smooth surface finish.

The experiments were carried out in a re-circulating water tunnel, with a test section of 1.27 m×0.5 m×0.38 m and a turbulence intensity of less than 1% for up to a flow velocity of U=0.3 m/s. The set-up used to hold the cylinder in the test-section had two air bearings to reduce the damping and to constrain the oscillations of the cylinder to one degree of freedom in the crossflow direction (Figure 4.1(b)). The curved cylinder was totally immersed in water such that the submerged part was exactly a quarter of a ring. Springs

were attached from the cylinder to a fixed housing. This set-up was used previously by Jain and Modarres-Sadeghi (2013) to study VIV of inclined cylinders in which the response of a straight vertical cylinder was shown to be in agreement with the results from Khalak and Williamson (1999).

A Micro-Epsilon ILD 1402-600 non-contacting motion sensor was used to record displacement data of the oscillating cylinder. The displacements were measured at one point on the top of the cylinder and outside water. Since the cylinder was rigid, this displacement represents the motion of the entire curved cylinder. A six-axis force sensor (ATI- Nano17/IP68) was attached to the upper end of the oscillating cylinder and measured the total flow forces acting on the cylinder in three perpendicular directions.

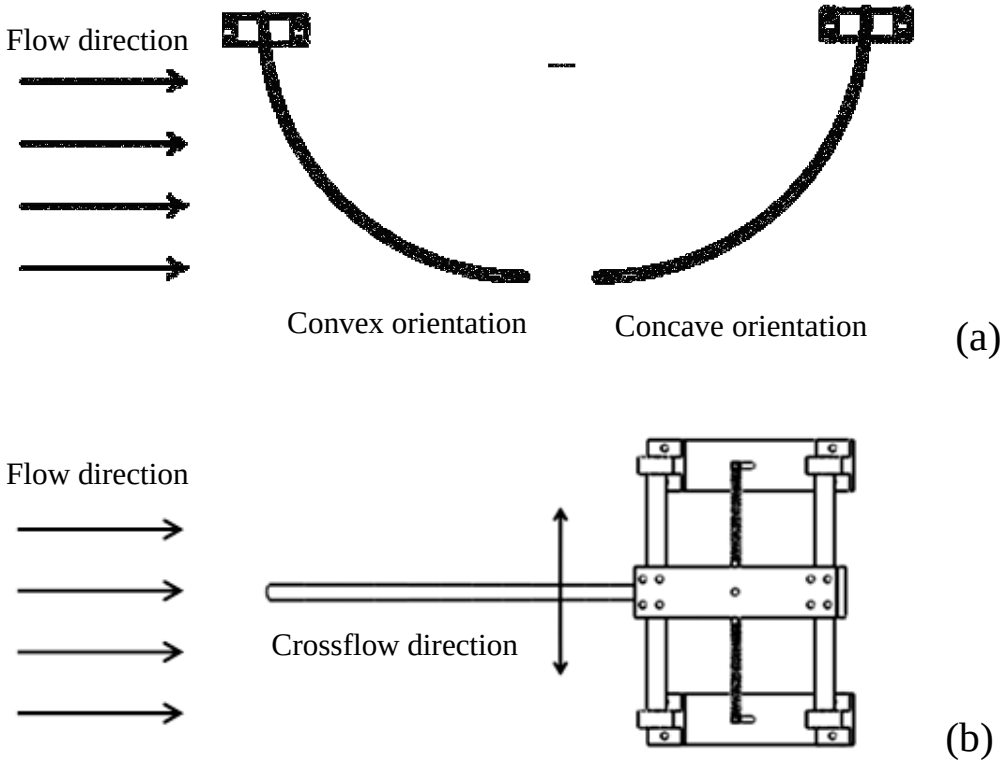

Figure 4.1. (a) The side view and (b) the top view of the schematic of the experimental set-up.

Decay tests in water and air were performed to obtain the natural frequency and damping ratio of the system. The natural frequency in water was f_{nw}=0.95 Hz, the natural frequency in air was f_{na}=1.1 Hz and the structural damping was ζ=0.01. The mass ratio of the cylinder calculated to be m^*=4.5 ($m^* = 4m/\pi\rho D^2 L$, where m is the total moving mass of the system, L the cylinder length, D its diameter, and ρ the flow density). The total mass of the system included the mass of the cylinder and the moving objects such as the air bearings, force sensor and the supporting plate used for mounting the cylinder.

4.3 The amplitude and frequency of oscillations

4.3.1 The convex orientation

First, the curved cylinder in the convex orientation was considered. During the course of these experiments, the water level was held constant and the flow velocity was increased from zero in small steps in a Reynolds number range of Re=300–2300. At each step, the amplitude and frequency of oscillations were calculated using the recorded displacement time series.

Figure 4.2(a) shows the dimensionless amplitude, A*=A/D, and frequency, f*=fos/fna, of oscillations versus the reduced velocity, U*=U/fosD, where fos is the dimensional measured frequency of oscillations and U is the dimensional flow velocity. This dimensionless velocity is referred to as the "true reduced velocity" in the literature (Khalak and Williamson, 1999), but for the sake of simplicity in this study we will call it the "reduced velocity". In order to have a basis for comparison, tests were conducted for a vertical cylinder with a mass ratio of m^*=4.5 (i.e., the same mass ratio as the curved

cylinder). The amplitude and frequency of oscillations for the vertical cylinder are plotted versus the reduced velocity in Figure 4.2. For the curved cylinder in the convex configuration, the lock-in range started at a reduced velocity of U*≈5, reached its maximum amplitude at a reduced velocity of U*≈6, remained almost constant over a range of reduced velocities and then dropped as the response exited the lock-in range around a reduced velocity of U*≈13. As depicted in Figure 4.2(a), the maximum amplitude of oscillations decreased dramatically from A*≈0.7 for a vertical cylinder to A*≈0.35 for the convex configuration. For the convex orientation, the lock-in range fell exactly in the same range of the reduced velocities as for the vertical cylinder (U*≈5–14).

The dominant frequency of oscillations normalized by the natural frequency in air (fos/fna) presented in Figure 4.2(b) remained at smaller values than unity during the lock-in range. This behavior in the convex orientation is different from the case of the vertical cylinder in which the frequency of oscillations exceeds unity at the reduced velocities at which the response switches from the upper branch to the lower branch (Khalak and Williamson, 1999).

The amplitude and frequency of oscillations are comparable with the results of de Vecchi et al. (2009) for a curved cylinder forced to oscillate at Re=100. They obtained a net positive C_{Lv} (lift coefficient in phase with velocity) for the convex orientation at a dimensionless amplitude of oscillations of around A^*=0.25, and a dimensionless frequency of f=1.1f_s where f_s is the Strouhal number for a fixed straight cylinder at Re=100.

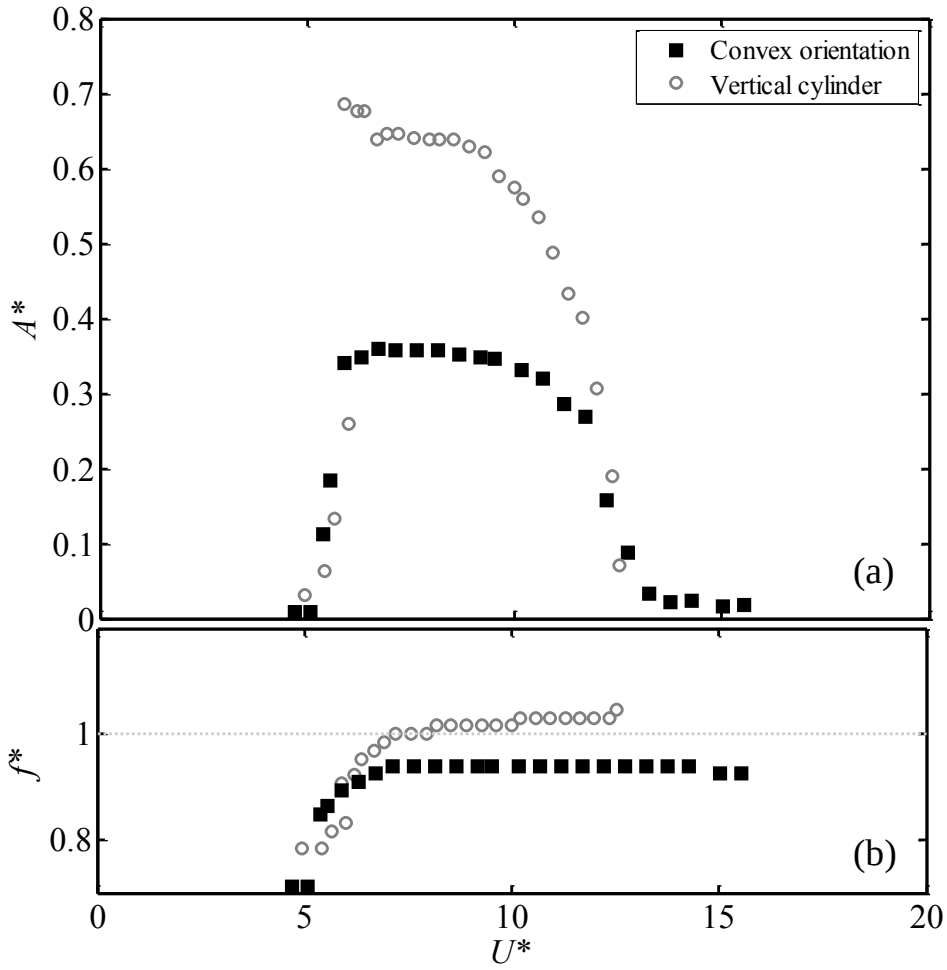

Figure 4.2. Dimensionless (a) amplitude ($A^*=A/D$) and (b) frequency ($f^*=f_{os}/f_{na}$) of the crossflow oscillations versus the reduced velocity for a curved cylinder in the convex configuration (■) and a vertical cylinder (○).

4.3.2 The concave orientation

A similar study was carried out for the same curved cylinder, but placed in the concave orientation. Figure 4.3(a) shows the dimensionless amplitude of oscillations versus the reduced velocity for this orientation.

Similar to the convex orientation, for the concave orientation, the amplitude of oscillations was smaller than the vertical cylinder. While in the convex orientation the amplitude remained constant in the lock-in range, in the concave orientation, initially the

amplitude increased to a maximum around a reduced velocity of $U^*\approx8$. Then it decreased smoothly until a reduced velocity of $U^*\approx13$, after which the amplitude remained almost constant until the cylinder exited the lock-in range around the reduced velocity of $U^*\approx18$. Compared with both the vertical cylinder and the curved cylinder in the convex orientation, an extended branch was observed at higher reduced velocities ($U^*\approx13–18$) in the concave orientation. The lock-in range began around the same reduced velocity for both the convex and the concave orientations, but the lock-in range for the concave orientation was significantly wider (ending at $U^*\approx18$ instead of $U^*\approx13$). This difference in response will be addressed in section 4.5 by looking at the flow forces acting on the cylinder. The decrease in the amplitude of oscillations for the curved cylinder (both orientations) compared to the vertical cylinder is in agreement with the experimental results of Assi et al. (2014). However, a direct quantitative comparison cannot be made since the set-up used in their work had a pendulum-like motion in two directions and also the cylinder had a horizontal extension, while the set-up used here had pure transitional motion with no extension in either end.

Similar to the convex orientation, in the concave orientation the dominant frequency of oscillations in the lock-in range (Figure 4.3(b)) remained at values smaller than the natural frequency of the system in air.

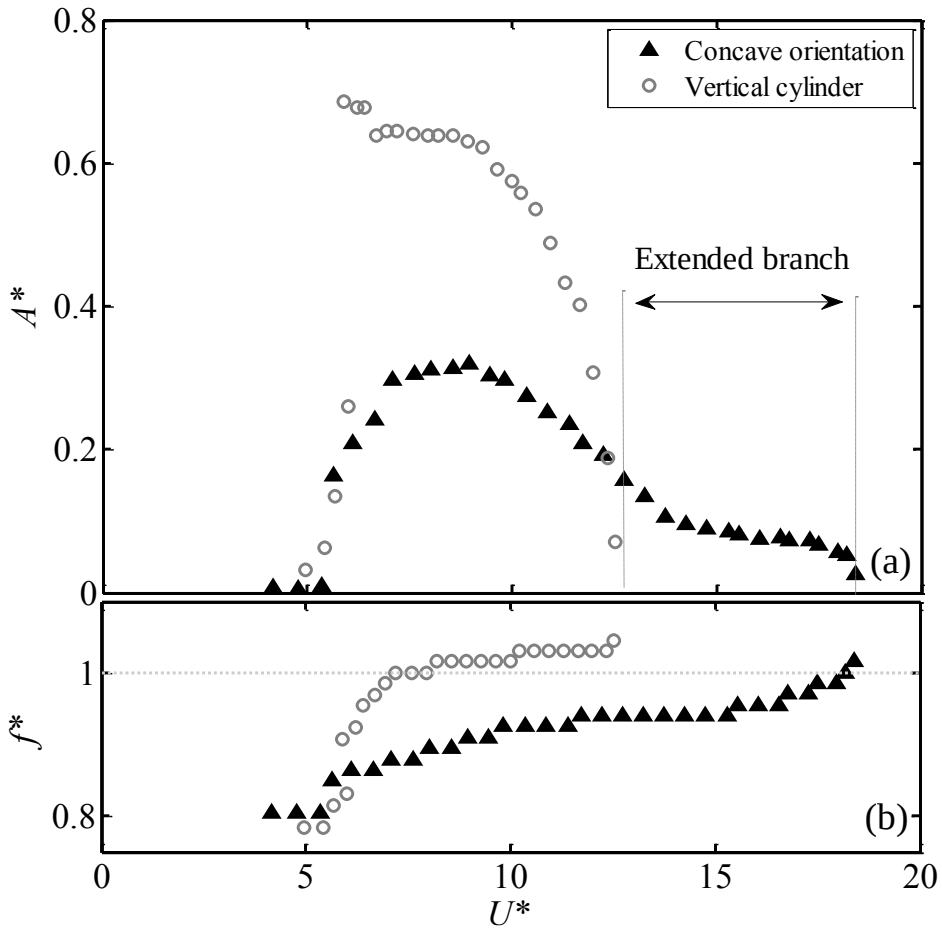

Figure 4.3. Dimensionless (a) amplitude ($A^*=A/D$) and (b) frequency ($f^*=f_{os}/f_{na}$) of the crossflow oscillations versus the reduced velocity for a curved cylinder in the concave configuration (▲) and a vertical cylinder (○).

4.4 The wake

In their numerical solution of the flow past a fixed concave cylinder, Miliou et al. (2007) observed shedding only at a small region in the upper part of the cylinder. No shedding was observed in the lower part of the cylinder. For a fixed curved cylinder in the convex orientation, experimental and numerical results of Miliou et al. (2007) showed that the vortex streets were shed vertically, independent from the curvature of the cylinder. In the current work, dye flow visualizations were performed at Re=500 for both stationary and free-to-oscillate cylinders in the convex and the concave configurations. A caramel-

like blend of dye was used to cover the overall length of the cylinder. The coated cylinder was placed in the test section, and the dye was slowly washed down into the wake of the cylinder.

Figure 4.4(a) shows the vortices in the wake of a fixed cylinder in the convex configuration. In this configuration, vortices were shed all along the cylinder and the vortex columns did not follow the cylinder's curvature exactly, but instead made a constant angle with respect to the oncoming flow. However, in the concave orientation (Figure 4.4(b)), the wake can be divided into two regions: in the lower part of the cylinder, no vortex shedding was observed but in the upper part of the cylinder, where the cylinder was mainly perpendicular to the oncoming flow, vortex shedding was observed with mainly vertical vortex columns. These observations are in agreement with the numerical results of Miliou et al. (2007) and the experimental results of Assi et al. (2014) for stationary curved cylinders.

When the curved cylinder was free to oscillate in the crossflow direction, the vortex columns were shed parallel to the curvature of the cylinder in both the convex and the concave configurations (Figure 4.4(c,d)). This is in agreement with the vortex shedding pattern in numerical study of de Vecchi et al. (2008, 2009) for the convex orientation. The axial component of the flow moved downward in the convex configuration and upward in the concave orientation. This is also similar to the wake behavior in the positive and negative angles of inclination in a flexibly-mounted inclined cylinder [13,15]. The flow visualizations suggest that the cylinder's oscillations forced the vortices to shed parallel to the cylinder's curvature, which is also similar to the behavior observed for an inclined cylinder. While for a fixed inclined cylinder placed in flow, the shedding does not follow

the angle of inclination, the cylinder's oscillations result in a shedding parallel to the cylinder's long axis.

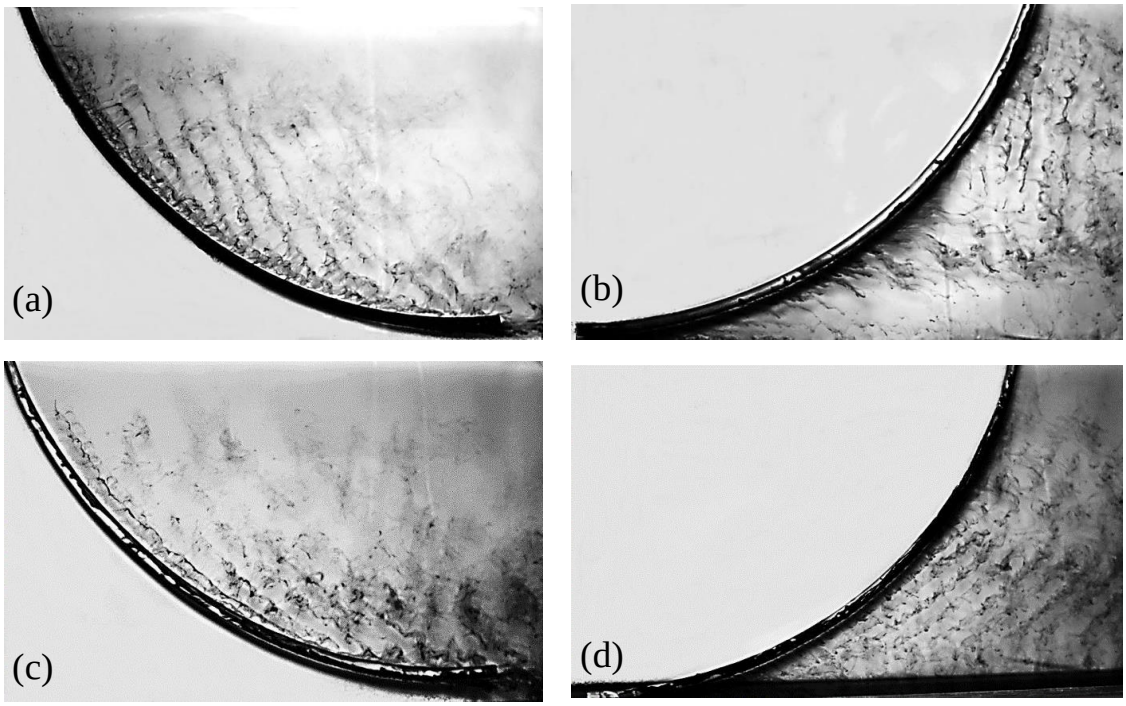

Figure 4.4. Flow visualizations in the wake of a curved cylinder for the fixed (a) convex and (b) concave configurations, and free-to-oscillate (c) convex and (d) concave configurations. Flow is from left to right.

4.5 Force measurement, phase difference and higher harmonic forces

Flow forces acting on the cylinder in the crossflow direction were measured directly using a six-axis force sensor attached to the upper end of the oscillating cylinder. The force sensor measured the total flow forces acting on the cylinder in the crossflow direction, which comprised both the hydrodynamic flow forces and the inertia force due to the motion of the force sensor. Thus, the inertia force was removed from the total measured force by post-processing the experimental data. The force sensor measurements were synchronized

with the displacement data readings from the non-contacting displacement sensor, making it possible to directly obtain the phase difference between the measured flow forces and the displacement of the cylinder in the crossflow direction.

Before discussing the force measurements for the curved cylinders, a series of tests on vertical cylinders are discussed in order to have a basis for comparison. Figure 4.5(a) shows the transverse force coefficients for a vertical cylinder within the lock-in range. The values for the first harmonic force coefficient (with a frequency close to the system's natural frequency), C_{y1}, are in agreement with the previously measured values as discussed, e.g. in (Khalak and Williamson, 1999). Besides the 1st harmonic component, both the second and the third harmonic force components (with frequencies twice and trice the system's natural frequency, respectively) were observed in the flow forces acting on the cylinder: C_{y2} and C_{y3}, respectively, in Figure 4.5(a). Sample FFT plots are shown later in Figure 4.9. The third harmonic force components have been observed in the previous studies on VIV of a straight cylinder, rigid or flexible, placed in flow, when the system had two degrees of freedom (Wang et al., 2003; Dahl et al., 2007; Modarres-Sadeghi et al., 2010; Bourguet et al., 2011b). The third harmonic component in the present vertical cylinder case, however, is observed for a case with only a crossflow displacement. This is due to the fact that the relative velocity of the cylinder moving in the crossflow direction makes an angle with respect to the oncoming flow. Assuming a sinusoidal motion for the cylinder in the crossflow direction as

$$y(t) = y_0 \sin(\omega_{os} t), \tag{4.1}$$

in which, ω_{os} is the frequency of cylinder oscillation, and for a small angle between the flow velocity and the relative velocity, θ, the flow forces acting in the crossflow direction can be expressed as

$$F_y(t) = F_L(t) - F_D\dot{Y}(t), \tag{4.2}$$

where F_L and F_D are the lift and drag forces with frequencies of f and $2f$, respectively and $\dot{Y}$ is the dimensionless velocity of the cylinder in the crossflow direction. Substituting the lift and drag forces as well as $\dot{Y}(t)$ in Eqn. (4.2), the flow force in the crossflow direction can be obtained as

$$F_y(t) = C_1 \sin\omega_{os}t + C_2 \cos\omega_{os}t + C_3 \sin 3\omega_{os}t + C_4 \cos 3\omega_{os}t, \tag{4.3}$$

in which C_1, C_2, C_3 and C_4 are functions of the lift and drag coefficients, frequency of oscillation and the phase difference between the flow force and the cylinder displacement. As expressed in Eqn.(4.3), the flow force in the crossflow direction consists of the 1st harmonic (terms with ω_{os}) as well as the 3rd harmonic (terms with $3\omega_{os}$) components. Wang et al. (2003) have discussed the existence of the 3rd harmonic component in the crossflow direction with some details.

The existence of the second harmonic component in the crossflow direction, however, is due to an asymmetric vortex shedding. At low reduced velocities, the wake consists of perfectly symmetric 2S shedding and therefore no contribution of the second harmonic component exists in that range of reduced velocities as shown in Figure 4.5(a). When the maximum amplitude of oscillation is reached, vortex shedding pattern follows an S+P shedding (a single vortex and a pair of vortices are shed in each period of oscillations), in agreement with the shedding pattern map presented by Williamson and Govardhan (2004). For larger reduced velocities, the vortex shedding pattern exhibits a 2P

shedding (two pairs of vortices are shed in each period of oscillation), in which the P shedding from each side is not necessarily exactly the mirror image of the P shedding of the opposite side. These asymmetric wakes result in flow forces both with the first and the second harmonics in the crossflow direction. The occurrence of the second harmonic in the crossflow direction for a vertical cylinder undergoing VIV has been recently observed and discussed by Du et al. (2014).

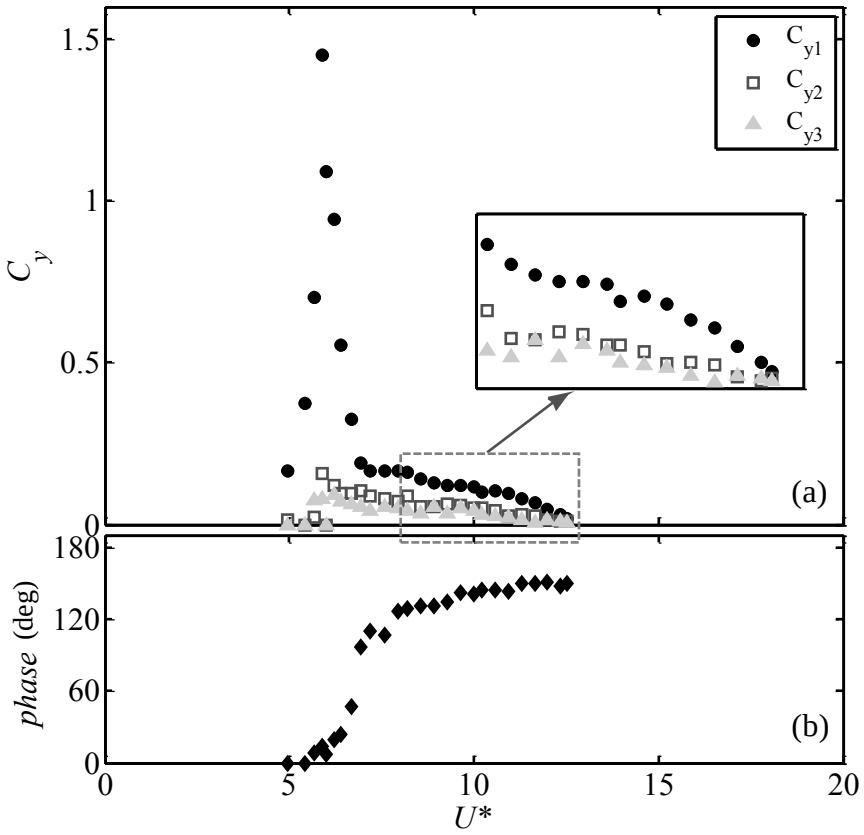

Figure 4.5. (a) The first (●), the second (□) and the third (▲) harmonic components of the transverse force and (b) the phase difference between the crossflow force and displacement versus the reduced velocity for vertical cylinder.

The phase difference between the flow force filtered around the fundamental frequency of oscillations and the cylinder displacement is plotted in Figure 4.5(b). For a vertical cylinder, a phase jump from 0° to 180° occurred at a reduced velocity of $U^*\approx 7$.

Khalak and Williamson (1999) observed this phase jump and showed that the phase difference of 0° corresponds to the upper branch response and the phase difference of 180° to the lower branch response. This is also observed in the present results.

The transverse force coefficients for a curved cylinder in the convex orientation are depicted in Figure 4.6(a). As shown in this figure, the maximum value for the main transverse force coefficient has decreased from $C_{y1}\approx1.5$ for the vertical cylinder to $C_{y1}\approx0.4$ for the convex orientation. This decrease in the maximum value of the flow force is in agreement with the decrease in the maximum amplitude of oscillations shown in Figure 4.2(a). The higher harmonic components of the flow force exist for the convex orientation as well. At higher reduced velocities, the higher harmonic contributions had larger values in the convex orientation compared to the vertical cylinder. As shown in the zoom box in Figure 4.6(a), both the second and the third harmonic components have values comparable to the first harmonic components at high reduced velocities.

The phase difference between the first harmonic component of the flow force and the cylinder displacement shown in Figure 4.6(b) for the convex orientation stayed at values smaller than 40º for reduced velocities smaller than $U^*\approx12$. At higher reduced velocities, where the magnitude of the force itself was very small, the phase difference reached the values of around 120º. These results show that compared to the vertical cylinder, in the convex orientation, no sudden phase jump occurred, but instead the phase difference increased gradually from zero to values close to 120º.

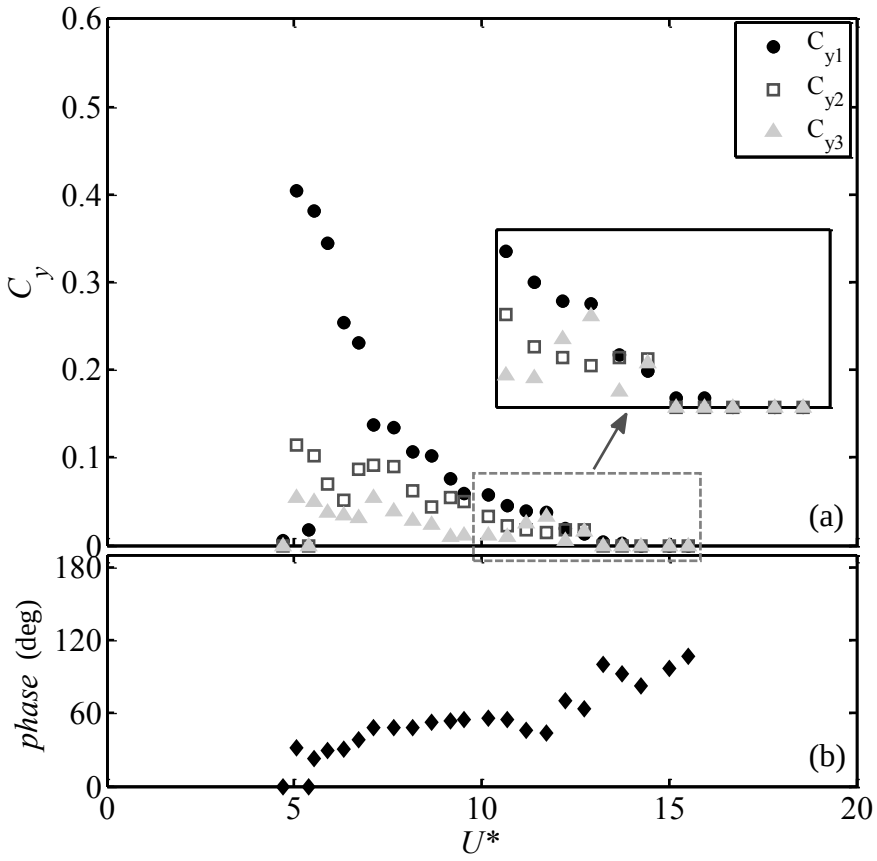

Figure 4.6. (a) The first (●), the second (□) and the third (▲) harmonic components of the transverse force and (b) the phase difference between the crossflow force and displacement versus the reduced velocity for the convex orientation.

Flow forces acting on the cylinder in the concave orientation are presented in Figure 4.7(a). As presented in this figure, the first harmonic components were dominant at the beginning of the lock-in range and the higher harmonics of the flow forces prevailed at higher reduced velocities. The phase difference between the first harmonic flow force and the cylinder displacement in the concave orientation (Figure 4.7(b)) follows almost the same trend as that for the convex orientation (Figure 4.6(b)) in which no sudden jump was observed within the lock-in range.

From Figure 4.7(a) it is observed that the contribution of the second and the third harmonic components of the force increased for the reduced velocities larger than $U^* \approx 13$.

Higher harmonic forces within this region have magnitudes up to 7 times the magnitude of the first harmonic component. Sample FFTs are shown later in Figure 4.9. This increase suggests that for reduced velocities larger than $U^* \approx 13$, the oscillation of the structure was being ruled by the second and the third harmonic components, which had frequencies 2 and 3 times the natural frequency of the system. In order to investigate whether these higher harmonic components contribute to the excitation of the structure or the dampening of the response, the lift force coefficients in phase with the cylinder velocity (C_{Lv}) have been calculated.[4] The magnitude of energy transferred to the structure can be determined by this dimensionless coefficient as

$$C_{Lv} = \frac{F_L \sin(\phi)}{1/2\, \rho L D U^2}, \tag{4.4}$$

where F_L is the lift force and φ is the phase difference between the lift force and the cylinder oscillation. Positive values of C_{Lv} represent the region where the energy is transferred from the flow to the cylinder and the structure is excited by the surrounding flow.

Figure 4.8 shows the C_{Lv} plots for the second and the third harmonic components of the flow force in the concave orientation. The lift coefficients in phase with velocity have positive values all along the lock-in range suggesting that these higher harmonic components of the flow force contribute to the excitation of the cylinder. Large contributions of the higher harmonic components (especially the 2nd harmonics) compared

[4] It ought to be mentioned here that we use the force measured in the crossflow direction in calculating C_{LV}, as this is the way C_{LV} is defined in the literature. This force is different from the lift force the way we have defined it in Eqn. (2), which makes an angle with respect to the force in the crossflow direction.

to the first harmonic force, at higher reduced velocities, led to the extended lock-in range in the concave orientation discussed previously in Section 4.3.2. In fact, in this part of the lock-in range, the cylinder was being excited by flow forces with mainly a frequency twice the system's natural frequency and therefore the structure's response had a smaller but non-zero amplitude as previously seen in Figure 4.3(a) for $13<U^*<18$. This means that the existence of the relatively large higher harmonic flow forces makes the lock-in range wider for the concave cylinder compared with the lock-in range for the convex and the vertical cylinder.

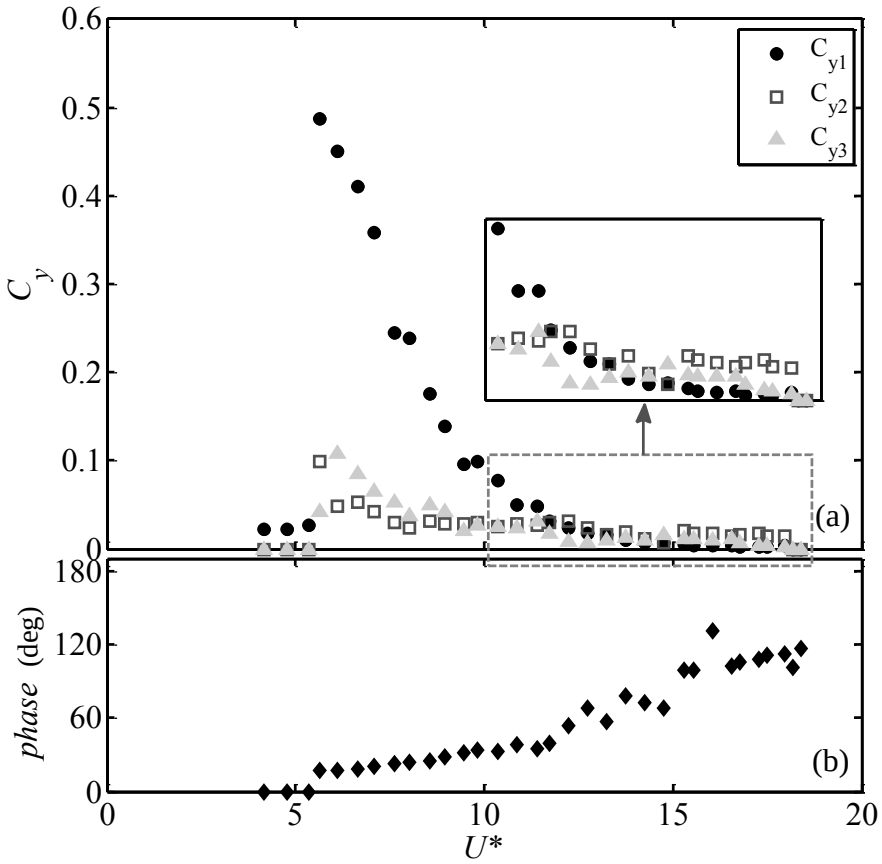

Figure 4.7. (a) The first (●), the second (□) and the third (▲) harmonic components of the transverse force and (b) the phase difference between the crossflow force and displacement versus the reduced velocity for the concave orientation.

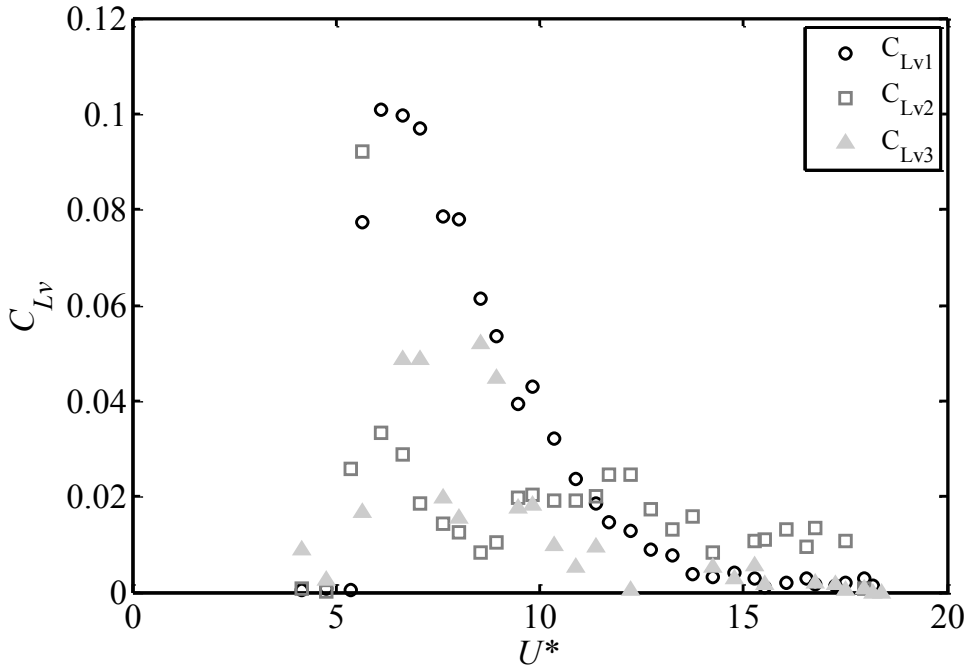

Figure 4.8. The first (●), the second (□) and the third (▲) lift force coefficients in phase with the cylinder velocity in the concave orientation.

It is worth mentioning that although these higher harmonic components existed in the convex orientation as well, since their relative contribution was smaller than the first harmonic flow force, the excitation mechanism was mainly ruled by the first harmonic component of the flow force in the convex orientation. For instance, a point with C_{y1}=0.003 in the convex orientation (for U^*=14.5) was placed out of the lock-in range while in the concave orientation, a point with the same value for C_{y1} (for U^*=17) was still in the extended lock-in range, because the higher harmonic components were larger than the 1st harmonic component in that case.

Figure 4.9 presents sample FFT plots at different reduced velocities in the lock-in range for the vertical, convex and concave cylinders. The reduced velocities have been chosen so that they cover the entire lock-in range. The first column (Figure 4.9(a-e)) represents the frequency contents at different reduced velocities for a vertical cylinder. The

higher harmonic components of the flow forces existed in the entire lock-in region but the first harmonic component was always the dominant one for the vertical cylinder. For the convex orientation (Figure 4.9(f-j)) the contributions of the higher harmonics of the flow forces increased and at higher reduced velocities, their contributions were comparable to the first harmonics. For the concave cylinder (Figure 4.9(k-o)), at the beginning of the lock-in range the first harmonic of the force dominated the forcing mechanism, while at reduced velocities larger than $U^*\approx13$, the contributions from the higher harmonics prevailed and the cylinder was excited by the higher harmonic flow forces.

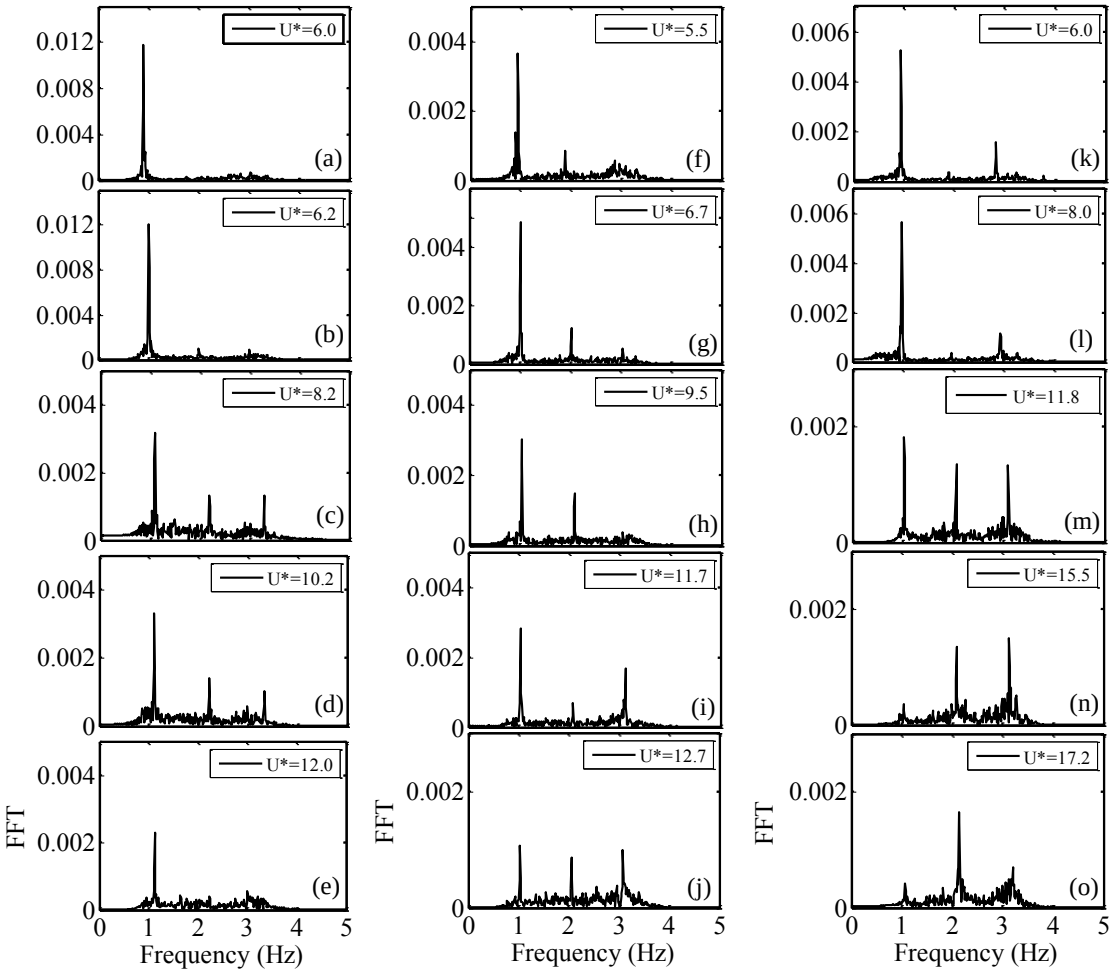

Figure 4.9. Sample FFT plots of the flow forces for (a-e) the vertical cylinder, and a curved cylinder in (f-j) the convex orientation and (k-o) the concave orientation.

4.6 Conclusions

Vortex-induced vibration of a curved cylinder free to oscillate in the crossflow direction was studied experimentally in the convex and the concave orientations. The curved cylinder was a quarter of a ring with a dimensionless radius of curvature of R/D = 47, with no horizontal or vertical extension, and free to oscillate in the crossflow direction. As expected, the amplitude of oscillations was decreased for both the convex and the concave orientations compared with a vertical cylinder. In the convex configuration, the amplitude of oscillations in the lock-in range stayed almost constant at A^* = 0.35 for the entire lock-in range. In the concave orientation, however, an extended branch was observed for the amplitude of oscillations at higher reduced velocities. For the curved cylinder, in both the concave and the convex orientations, no jump was observed in the phase difference between the crossflow displacement and flow force, contrary to the phase jump from 0° to 180° for a vertical cylinder.

Flow visualizations were carried out for both fixed and free-to-oscillate curved cylinders, in both orientations. For the fixed curved cylinder, in the concave orientation, no vortex shedding was observed in the lower part of the cylinder and vertical shedding was observed in the upper part of the cylinder in agreement with previous studies. In the convex configuration, the vortices were shed in parallel and at a constant angle with respect to the oncoming flow. When the cylinder was free to oscillate in the crossflow direction, however, parallel vortex shedding, following the curvature of the cylinder, was observed in both configurations.

In addition to the crossflow force at a frequency close to the natural frequency of the system, higher harmonic components of the flow force, both the second and the third

harmonic components, were observed. The existence of the second harmonic component was related to an asymmetric vortex shedding pattern and the third harmonic component was related to the relative velocity of the moving cylinder with respect to the oncoming flow. The higher harmonic contributions stayed less than the first harmonic for the vertical cylinder in the entire lock-in range. In the convex orientation, the higher harmonic contribution had smaller values at lower reduced velocities but reached values close to the first harmonics at higher reduced velocities toward the end of the lock-in range. In the concave orientation, the higher harmonic contributions became even larger than the first harmonic at the higher reduced velocities. It was shown that the higher harmonic components of the flow force contributed to the excitation of the cylinder. Therefore, the wider lock-in range in the plot of the amplitude of oscillations in the concave orientation was related to the increased contribution of the higher harmonic forces at larger reduced velocities.

CHAPTER 5

AN EXPERIMENTAL INVESTIGATION OF VORTEX-INDUCED VIBRATION OF A ROTATING CIRCULAR CYLINDER IN THE CROSSFLOW DIRECTION[5]

5.1 Introduction

Flow past spinning cylinders placed in flow has been studied extensively from the wake dynamics point of view and with a focus on flow control methods. Early experimental studies by Tokumaru and Dimotakis(Tokumaru and Dimotakis, 1991, 1993) are among the first studies that showed how the wake can be controlled by subjecting the cylinders in tandem arrangements to rotatory oscillations at different positions in flow. Earlier studies in this area have shown that when rotating cylinders are placed in flow, the symmetry of the wake is disturbed, which can significantly delay the boundary layer separation and result in significant pressure drag reduction.(Modi, 1997) Previous investigations have also shown that depending on different values of the rotation rate, α, defined as the ratio of the surface velocity and free stream velocity, different flow regimes can be observed.(Badr et al., 1990; Lie and Kaasen, 2006; Rao et al., 2013) While for the non-rotating circular cylinders, vortex shedding associated with the von-Kármán instability is observed, by increasing the rotation rate, α, the vortex shedding diminishes at $\alpha \approx 2$. The wake becomes

[5] The results discussed in this chapter have been submitted for publication to Phys. Fluids. B. Seyed-Aghazadeh, Y. Modarres-Sadeghi**, "**Vortex-induced vibrations of a curved circular cylinder in the crossflow direction".

unstable once again for a small range of $4.4<\alpha<4.75$ in which low-frequency one-sided vortex shedding is observed. This second instability appears to be stronger than the first instability in terms of the amplitude of unsteady forces acting on the cylinder.(Coutanceau and Menard, 1985; Badr et al., 1990; Chew et al., 1995; Kang et al., 1999; Stojkovic et al., 2002; Mittal and Kumar, 2003; Pralits et al., 2010; Kumar et al., 2011) Three-dimensional wake modes, same as the ones observed for non-rotating cylinders,(Williamson, 1996) have been observed for a rotating cylinder. Some new unstable three-dimensional wake modes are introduced in this case which are dependent on the Reynolds number and the rotation rate.(Rao et al., 2013) A recent review on the flow past a rotating cylinder by Rao et al. (summarizes the details of different steady and unsteady regions and also two and three dimensional transitions that occur by increasing the rotation rate at low Reynolds numbers. The review comprises of the results both from the numerical solutions based on linear stability analysis and experiments on the rotating cylinders for $\alpha<7$ and $Re<400$.

The question that is considered in the present work is how the system will behave if it is given a degree of freedom to oscillate in the transverse direction. When a circular cylinder (with no imposed rotation) is placed in flow and is free to oscillate with one or two degrees of freedom, oscillations with amplitudes close to the cylinder's diameter are observed in the range of flow velocities in which the frequency of vortex shedding gets locked into the frequency of oscillations (lock-in range). This is called Vortex-Induced Vibration (VIV). VIV of a uniform non-rotating circular cylinder placed normal to flow has been studied extensively, both for a flexibly-mounted rigid cylinder(Bearman, 1984; Sarpkaya, 2004; Williamson and Govardhan, 2004; Vandiver, 2012) and a flexible

cylinder.(Vandiver, 1993; Modarres-Sadeghi et al., 2011; Bourguet et al., 2012; Wu et al., 2012) How will the VIV response of a non-rotating cylinder change due to an imposed rotation? How will the rotation rate affect the response? Will there be a range of rotation rates for which VIV can be suppressed?

This problem, in which the symmetry of the surrounding wake is broken due to an imposed rotation along the long axis of the cylinder, has received relatively limited attention. In an experimental work by Stansby and Rainey (2001b) large amplitudes of oscillations (higher than 10 diameters) have been reported for $0.25<\alpha<0.5$ and $200<Re<4700$ for a rotating cylinder free to oscillate in both the crossflow and inline directions. These large-amplitude oscillations had frequencies much lower than the structural natural frequency and did not occur in a range of reduced velocities which would have been a characteristic of VIV. On this basis, the system was believed to be undergoing galloping. Computational simulations have been conducted(Stansby and Rainey, 2001a) for a two-degree-of-freedom cylinder free to oscillate both in the inline and crossflow directions placed in two-dimensional laminar flow. It was shown that large-amplitude oscillations at several times the cylinder diameter can occur at $\alpha=0.3$ and a reduced velocity of $U^*=14$ that corresponds to a reduced velocity where VIV does not usually occur. The large orbital motion at this point was accompanied by low-amplitude, high-frequency motion originated from vortex formation. In the studies discussed so far, the influence of rotation rate was not considered for the range of reduced velocities corresponding to the lock-in range of a non-rotating cylinder.

Bourguet and Lo Jacono (2014) have studied the flow-induced instability of a rotating circular cylinder free to oscillate in the crossflow direction by means of two- and three-dimensional numerical simulations using spectral/hp method at Re=100. Based on these simulations, the rotating cylinder undergoes flow-induced instability for rotation rates less than α=4. These oscillations were observed both within the range of reduced velocities for which a non-rotating circular cylinder would undergo VIV and for higher reduced velocities. The maximum amplitude of oscillations observed for this cylinder was close to 1.9 times the cylinder diameter. This maximum amplitude was found to be associated with a new wake pattern T+S (A triplet of vortices and a single vortex shed per cycle). Also it was concluded that the rotating cylinder can oscillate even in the range of flow velocities for which no vortex shedding was observed (U pattern). The large-amplitude oscillations corresponding to the U pattern were found to be different from VIV since no vortex shedding was observed in this range. In another recent numerical work by Zhao et al. (2014), one- and two-degree-of-freedom VIV of a rotating cylinder has been studied for three rotation rates: α=0, 0.5, 1 at Re=150. In the one-degree-of-freedom VIV, it was concluded that the general trend of the amplitude and frequency of oscillations for rotation rates α=0.5 and 1 follows the same trend as a non-rotating cylinder. It was observed that the lock-in range became wider and the amplitude of oscillations increased at higher rotation rates. At all the reduced velocities in the lock-in range, 2S vortex shedding was observed for α=0, 0.5, 1 in the one-degree-of-freedom VIV. For the two-degree-of-freedom VIV, P+S vortex shedding pattern was found in the reduced velocities corresponding to the higher boundaries of the initial branch and 2S shedding pattern was observed in all the other reduced velocities in the lock-in range.

While the previous studies on VIV of a rotating cylinder with one-degree-of-freedom have been numerical, in the current work, for the first time, an experimental investigation of the problem is presented. The rotating cylinder was free to oscillate in the crossflow direction and was studied over a range of rotation rates of $0<\alpha<2.6$, reduced velocities of $4<U^*<11$, and Reynolds numbers of $350<Re<1000$.

5.2 Experimental set-up

The experiments were carried out in a re-circulating water tunnel, with a test section of 1.27 m×0.5 m×0.38 m and a turbulence intensity of less than 1% for up to a flow velocity of U=0.3 m/s. A uniform circular cylinder with a diameter of D=1.3 cm was tested. The set-up was designed such that the cylinder could be forced to rotate at variable rotation speeds using a variable low-speed electric motor. A combination of two bearings and a universal joint, which connected the motor shaft to the cylinder, were incorporated (Figure 5.1(a)). The motor had a variable rotation speed in a range of 0-500 RPM, which covered the range of desired rotation rates in the experiment. The cylinder rotated in the counter-clockwise direction when the flow direction was from left to right (Figure 5.1(b)). A major challenge in designing this set-up was to minimize the unbalance of the rotating cylinder to avoid any influence of the unbalance on the dynamics of the wake. Toward this end, a universal joint was used to connect the shaft from the motor to the cylinder, and the cylinder was supported by two ball bearings at different heights outside of water. The set-up was suitable for tests in which the rotating cylinder was constrained from moving in the crossflow and inline directions, as well as tests in which the rotating cylinder was mounted

on a 1D air-bearing set-up and was free to oscillate in the crossflow direction. The 1D air-bearing set-up had two air bearings to reduce the damping and to constrain the oscillations of the cylinder to one degree of freedom in the crossflow direction (Figure 5.1(a)). Springs were attached from the cylinder to a fixed housing. This set-up was used previously by Jain and Modarres-Sadeghi (2013) and Chaplin et al. (2005b) to study VIV of inclined and tapered cylinders in which the response of a straight non-rotating vertical cylinder was shown to be in agreement with the results of Khalak and Williamson (1999)

A Micro-Epsilon ILD 1402-600 non-contacting motion sensor was used to record displacement data of the oscillating cylinder. The displacements were measured at one point at the top of the cylinder and outside water. A six-axis force sensor (ATI-Nano17/IP68) was attached to the upper end of the oscillating cylinder and measured the total flow forces acting on the cylinder in three perpendicular directions. The rotation rate of the cylinder was measured using a non-contacting laser tachometer.

Decay tests in water and air were performed to obtain the natural frequency and damping ratio of the system. The natural frequency in water was f_{nw}=0.53 Hz, the natural frequency in air was f_{na}=0.55 Hz and the structural damping was ζ=0.01. The mass ratio of the cylinder calculated to be m^*=11.5 ($m^* = 4m/\pi\rho D^2 L$, where m is the total moving mass of the system, L the cylinder length, D its diameter, and ρ the flow density). The total mass of the system included the mass of the cylinder and the moving objects such as the air bearings, the DC motor, the force sensor and the supporting plate used for mounting the cylinder.

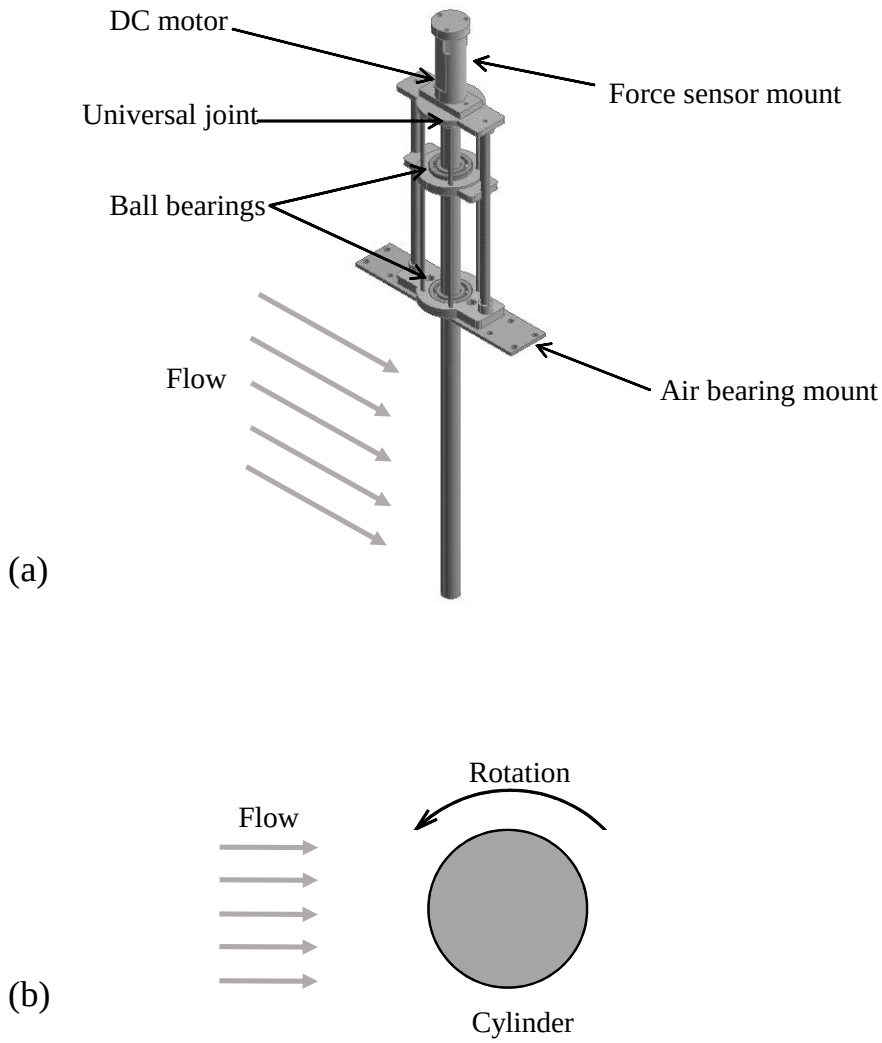

Figure 5.1. Schematics of the set-up.

5.3 The wake of a non-oscillating cylinder

The first series of tests were conducted on a rotating cylinder without the degree of freedom to oscillate in the crossflow direction. The goal was to observe the cylinder's wake at different rotation rates and compare that with the existing results in the literature. Observing similar vortex shedding patterns as those previously reported in the literature

would ensure that the set-up worked properly and the rotating cylinder did not suffer from any major unbalance. Flow visualizations using dye tubes were performed on the non-oscillating cylinder at varying rotation rates: $0<\alpha<4.6$. Figure 5.2 shows the cylinder's wake for varying rotation rates at a constant Reynolds number: Re=560. The von Kármán street was observed for rotation rates smaller than α=1.8. Mittal and Kumar (2003) also observed a periodic vortex shedding pattern for rotation rates of $0<\alpha<1.9$ at Re=200 in their numerical study. The imposed rotation of the cylinder introduced asymmetry in the vortex shedding pattern as it can be observed in Figure 5.2 where the symmetric 2S vortex shedding pattern at α=0 became asymmetric at larger rotation rates. Also, as previously discussed by Kumar et al. (2011), as a consequence of the cylinder rotation, the vortex street was deflected for large rotation rates as shown in Figure 5.2(c-h). At rotation rates larger than α=1.8, the vortex shedding stopped, and no shedding was observed in the range of $1.8\leq\alpha\leq4.2$ (Figure 5.2(i-j)). In an experimental study by Kumar et al. (2011) they observed that vortex shedding was suppressed at α=1.95 for Re=200 and reported a "snake shape" pattern for rotation rates of $2<\alpha<4.45$. The range of rotation rates in which no vortex shedding was observed and also the pattern observed in the wake for this range ($1.8\leq\alpha\leq4.2$) was similar to their results. This wake pattern and vortex shedding suppression had also been observed previously for the same range of rotation rates.(Rao et al.; Badr et al., 1990; Mittal and Kumar, 2003; Huera-Huarte et al., 2006) The flow became unstable again for α=4.4, and low-frequency one-sided vortex shedding was observed (Figure 5.2(k)). Such a one sided vortex shedding pattern was first observed in the two-dimensional numerical solutions of Mittal and Kumar (2003) in the range of $4.4<\alpha<4.8$ at Re=200. The vortex shedding disappeared again for higher rotation rates as shown for α=4.6 in Figure 5.2(l).

Overall, the observed wake patterns were completely in agreement with the previously-reported results based on numerical as well as experimental studies at different Reynolds numbers.(Mittal and Kumar, 2003; Kumar et al., 2011) This agreement implied that the experimental set-up was reliable and therefore could be used to study the behavior of a rotating cylinder free to oscillate in the crossflow direction, which will be discussed in what follows.

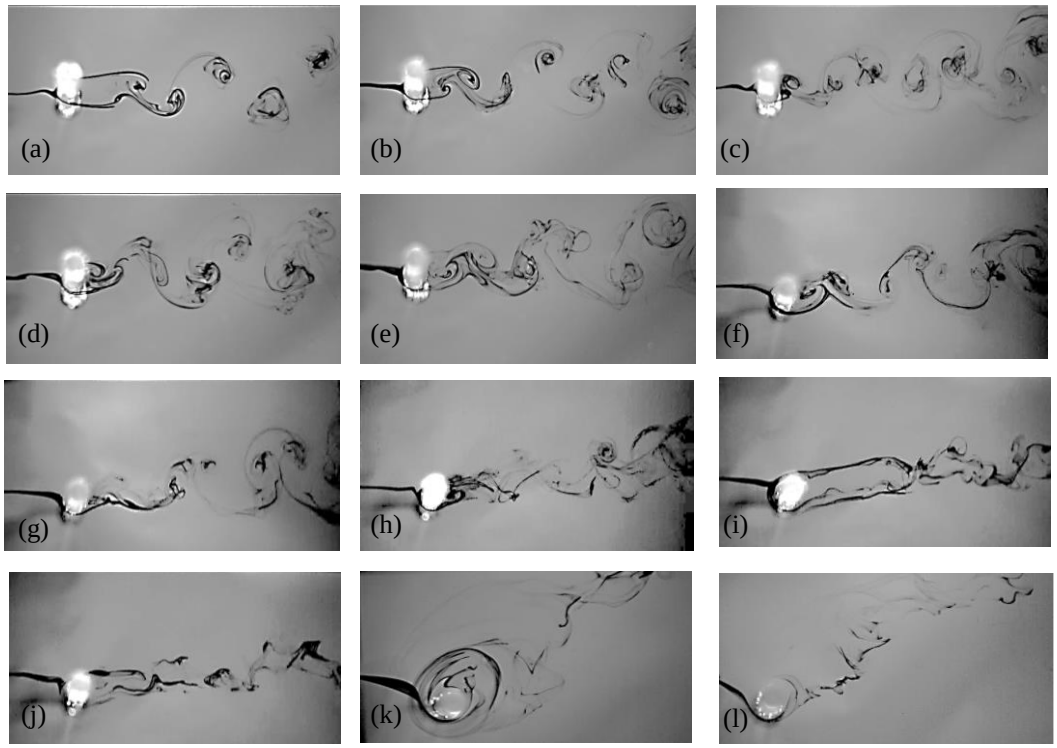

Figure 5.2. Flow visualizations for the non-oscillating rotating cylinder at a reduced veloicty of U^*=5.2 and varying rotation rates: (a) α=0.0, (b) α=0.4, (c) α=0.6, (d) α=0.8, (e) α=1.0, (f) α=1.2, (g) α=1.4, (h) α=1.6, (i) α=1.8, (j) α=2.0, (k) α=4.4, (l) α=4.6.

5.4 An oscillating cylinder

The main series of experiments were conducted to study the influence of rotation rate on the VIV response of a circular cylinder. Thirteen different rotation rates in the range

of $0 \leq \alpha \leq 2.6$ with increments of 0.2 were tested in the reduced velocity range of $4 < U^* < 11$. During the course of these experiments, the water level was held constant and the flow velocity was increased from zero in small steps in a Reynolds number range of Re=350–1000. To keep the rotation rate at a constant value at different reduced velocities, the rotation speed of the motor was varied at small steps so that the ratio between the surface velocity and the incoming flow velocity was kept constant. At each step, the amplitude and frequency of oscillations were measured using the recorded displacement time series of the cylinder.

5.4.1 Amplitude and frequency of oscillations

The amplitude of the response in the crossflow direction is plotted in Figure 5.3(a) for varying rotation rates at different reduced velocities. The dimensionless amplitude of oscillations is defined as $A^* = A/D$ and the reduced velocity is defined as $U^* = U/f_{nw}D$, where A is the amplitude of oscillations, f_{nw} is the measured dimensional natural frequency in water and U is the dimensional flow velocity. The amplitudes of oscillations were obtained using the time histories of the cylinder oscillations covering at least 100 periods of oscillations.

As shown in Figure 5.3(a), for α=0, which is the classical one-degree-of-freedom VIV for a non-rotating uniform circular cylinder, the lock-in range started at a reduced velocity of $U^* \approx 5$, reached a maximum amplitude of $A^* \approx 0.5$ and exited the lock-in range at a reduced velocity of $U^* \approx 10.5$. This behavior was in agreement with the previously reported results for VIV response of non-rotating uniform circular cylinders. By increasing the rotation rate slightly, the general behavior of the system stayed similar to a non-rotating

case; i.e., there was a range of reduced velocities for which a lock-in range was observed. The maximum amplitude of oscillations, however, increased slightly for higher rotation rates, and reached $A^* \approx 0.6$ for $\alpha=2.4$. Also, as observed in Figure 5.3(a), the lock-in range became narrower by increasing the rotation rate: for the non-rotating case, $\alpha=0$, the lock-in range was $5<U^*<10.5$, while for a larger rotation rate of $\alpha=2.4$, the oscillations occurred at a range of $6<U^*<7.8$. The oscillations ceased at rotation rates larger than $\alpha=2.4$. Figure 5.3(b) shows the contour map of the displacement at varying rotation rates in the lock-in range. The narrower lock-in range and the larger amplitudes of oscillations at higher rotation rates are observed clearly in this plot.

Figure 5.4 shows the dominant frequency of oscillations normalized by the natural frequency in air (f_{os}/f_{na}) versus the reduced velocity for varying rotation rates. For a non-rotating circular cylinder ($\alpha=0$), the dimensionless frequencies stayed below unity for small reduced velocities corresponding to the initial branch in the amplitude of oscillations ($5<U^*<6$). The dimensionless frequency then exceeded unity at larger reduced velocities ($6<U^*<10.5$), where the amplitude of oscillations corresponded to the lower branch response, as expected.(Khalak and Williamson, 1999) By increasing the rotation rate, the dimensionless frequencies decreased and beyond $\alpha=2.0$ the dominant frequency of oscillations, all along the lock-in range, remained at values smaller than the system's natural frequency in air. Overall, it was observed that the imposed rotation of the cylinder decreased the frequency of oscillations of the cylinder compared with a non-rotating cylinder.

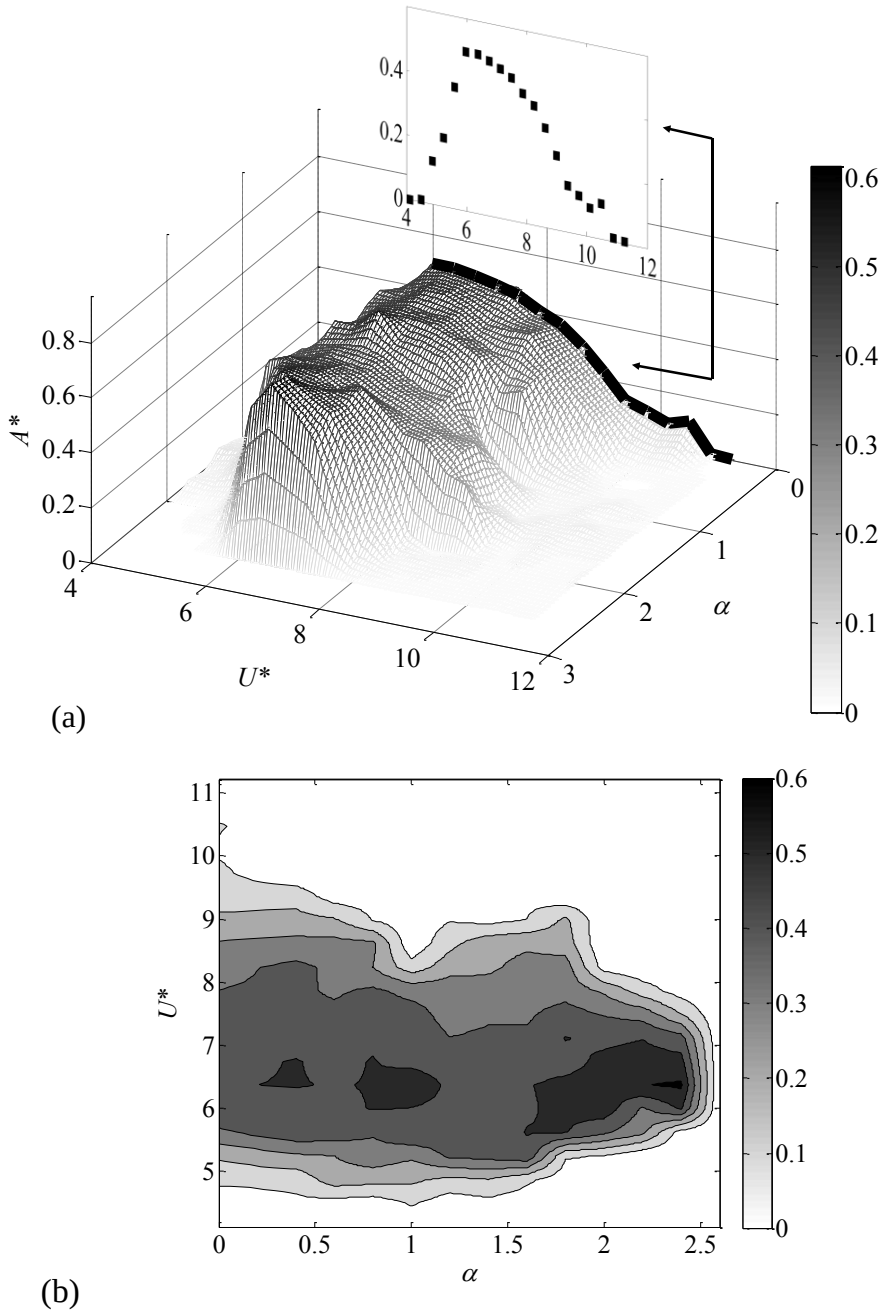

Figure 5.3. (a) Three-dimensional and (b) contour plots of the dimensionless amplitude of the crossflow oscillations ($A^*=A/D$) versus the reduced velocity, U^*, and the rotation rate, α.

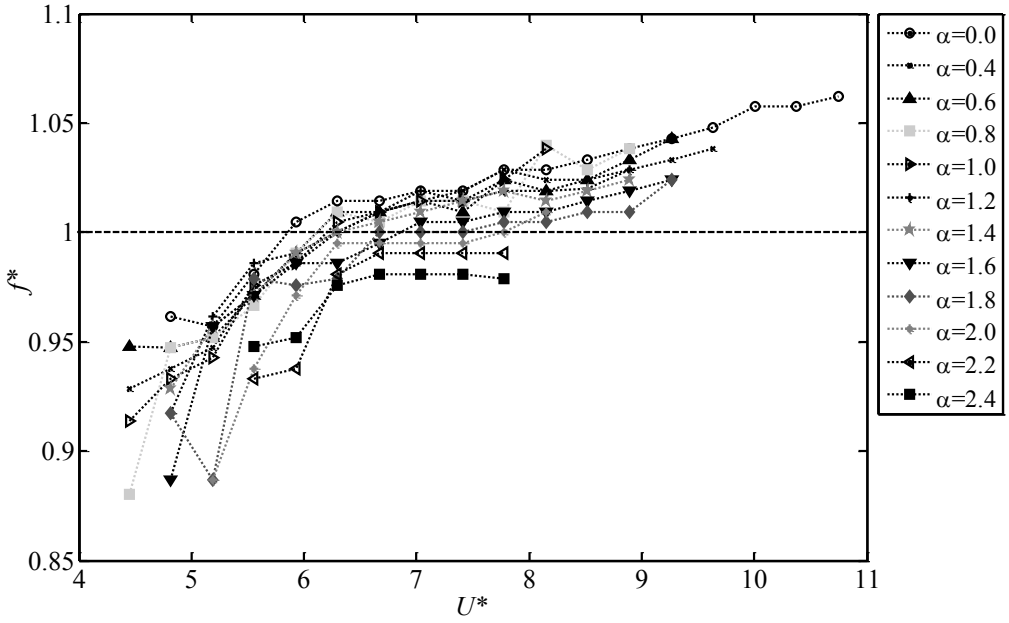

Figure 5.4. Dimensionless frequency of the crossflow oscillations ($f^*=f_{osc}/f_{na}$) versus the reduced velocity ($U^*=U/f_{nw}D$) at different rotation rates α.

Figure 5.5 shows the cylinder's mean displacement values versus the reduced velocity for different rotation rates. As it was previously shown in Figure 5.2 for a non-oscillating rotating cylinder, increasing rotation rate led to an increasing deflection of the vortex street in the wake of the cylinder (Magnus effect)(Mittal and Kumar, 2003). A similar behavior was observed for the oscillating cylinder, as a result of which the cylinder experienced a large mean displacement in the crossflow direction at each reduced velocity for large rotation rates. The mean displacement of the cylinder also increased by increasing reduced velocity.

Similar amplitudes of oscillations and lock-in ranges were observed in the numerical study of the rotating cylinder by Zhao et al. (2014), where the rotation rates of α=0, 0.5 and 1 were tested at a Reynolds number of Re=150. In their numerical simulation of the flow past a rotating cylinder, Bourguet and Lo Jacono (2014) observed larger

maximum amplitudes of oscillations at higher rotation rates (close to 1.9 times the cylinder diameter at α=3.75). Also they observed the oscillations over a wider range of rotation rates $0 \leq \alpha \leq 3.75$. The differences between their numerical results and the results obtained from the current experiments are possibly due to the differences in the Reynolds number, end conditions and the structural damping (0.01 in the current experiments versus zero in their numerical simulations).

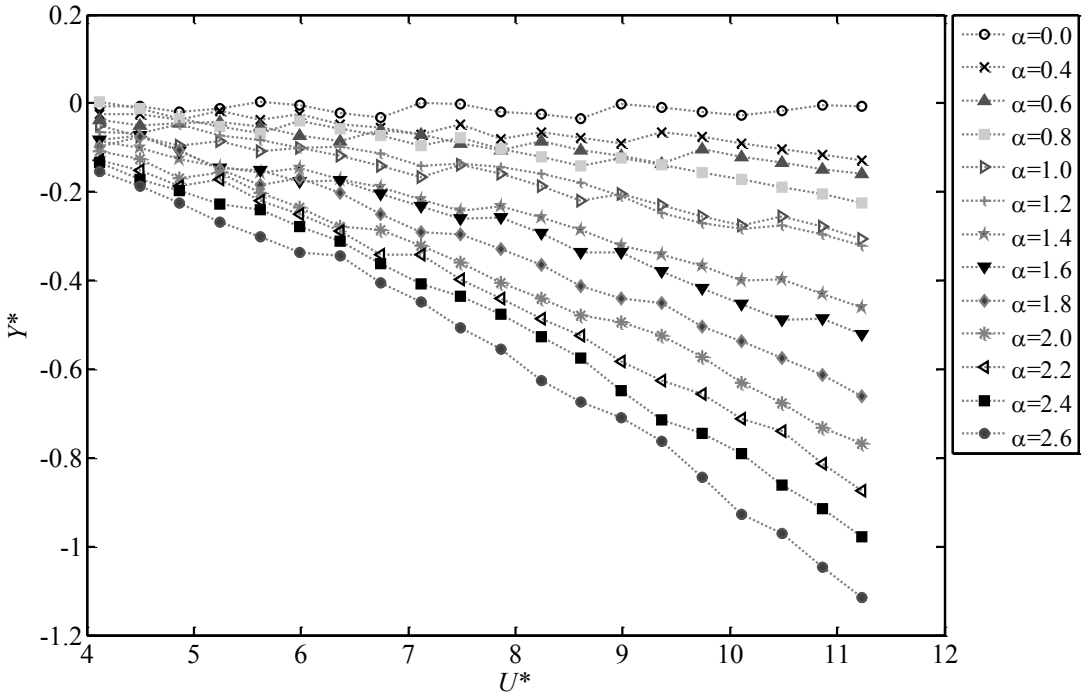

Figure 5.5. Dimensionless mean amplitude of the crossflow oscillations ($Y^*=Y_{mean}/D$) versus the reduced velocity ($U^*=U/f_{nw}D$) at different rotation rates, α.

5.5 The wake

As shown in Figure 5.2 for a non-oscillating rotating cylinder, vortex shedding was observed first at rotation rates of $0 \leq \alpha \leq 1.6$ and then at α=4.4. For a rotating cylinder with a

degree of freedom to oscillate in the crossflow direction, dye flow visualizations were conducted to investigate how the oscillations of the cylinder influenced the vortex shedding pattern. Figure 5.6 shows the wake of the cylinder at a constant reduced velocity of U^*=5.2 for varying rotation rates. The Reynolds number corresponding to this reduced velocity was Re=560, same as the Reynolds number used for the case of a non-oscillating cylinder (Figure 5.2). Shown in Figure 5.6(a) is the symmetric 2S vortex shedding for a non-rotating cylinder (α=0). Increasing the rotation rate resulted in a symmetry breaking in the vortex shedding pattern. As a consequence of the rotation, the general pattern of the vortex street deviated from the classical von Kármán street (2S shedding) to an asymmetric P shedding at larger rotation rates (Figure 5.6(b-i)): For α<1.4, 2S shedding was observed and for 1.4≤α≤1.8, asymmetric P shedding. Figure 5.7 shows the snapshots taken for one cycle of the cylinder's oscillations at α=1.8. The dashed line is the mean displacement line. At the beginning of the cycle, when the cylinder was at its upper extreme position, a vortex started to form from the upper side of the cylinder. The vortex was then shed when the cylinder passed the mean displacement line (Figure 5.7(b)). When the cylinder reached its lower extreme position, the shear layer from the lower side of the cylinder was entrained into the vortex that had already been shed from the upper side, forming a P vortex. This observation of P vortex pattern was similar to that reported in the numerical results of Bourguet and Lo Jacono (2014) for the rotation rate of α=1.5 at U^*=10. As shown in Figure 5.6(j–l), for larger rotation rates, i.e., α=2.0 – 2.6, no vortex shedding was observed at this reduced velocity (U^*=5.2), which is in line with the very small amplitudes of oscillations observed at this point (Figure 5.3).

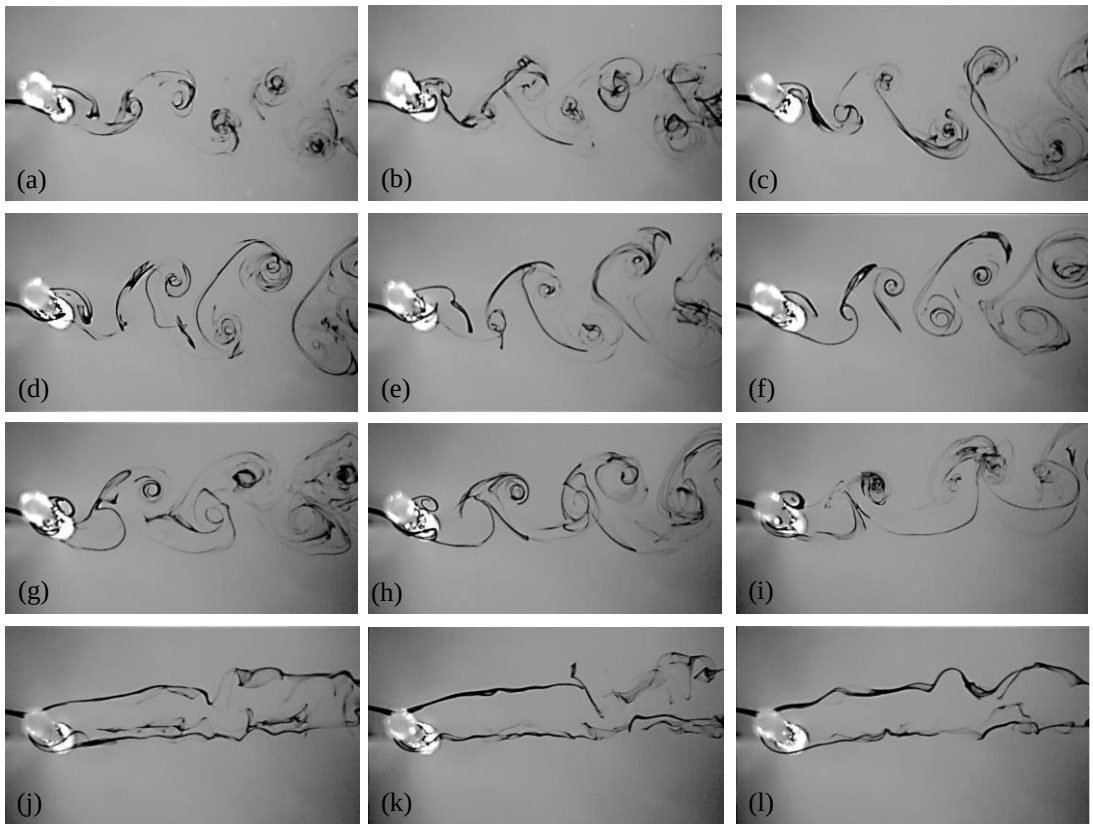

Figure 5.6. Flow visualizations for the oscillating cylinder at a reduced veloicty of U^*=5.2 and varying rotation rates: (a) α=0.0, (b) α=0.4, (c) α=0.6, (d) α=0.8, (e) α=1.0, (f) α=1.2, (g) α=1.4, (h) α=1.6, (i) α=1.8, (j) α=2.0, (k) α=2.4, (l) α=2.6.

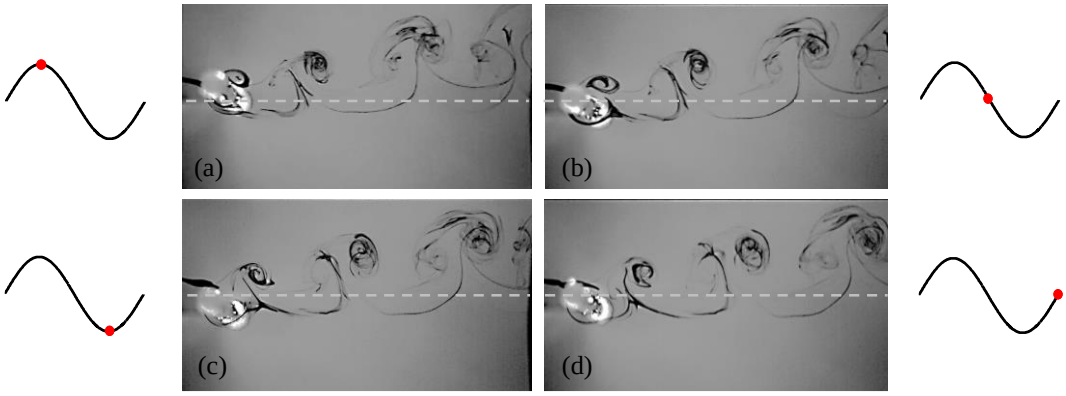

Figure 5.7. Flow visualizations for the oscillating cylinder in one cycle of oscillations at a reduced veloicty of U^*=5.2 and a rotation rate of α=1.8.

As it was shown in Figure 5.6, at a constant reduced velocity, vortex shedding was suppressed for high rotation rates. Then the case of a constant rotation rate, α=0.6, was considered and the influence of increasing reduced velocity on the shedding pattern was studied (Figure 5.8). The 2S vortex shedding was observed at all reduced velocities along the lock-in range and beyond (up to the maximum reduced velocity tested, U^*=10.8. Similar to the classical VIV of a non-rotating cylinder, the vortex shedding frequency was locked into the frequency of oscillations within the lock-in range (Figure 5.8(a–f)). At reduced velocities out of the lock-in range (Figure 5.8(g-i)), the von Kármán street was still observed, and the shedding frequency followed the Strouhal line. The vortex street slightly deviated from the zero mean line in the crossflow direction as a consequence of the Magnus effect, as expected.

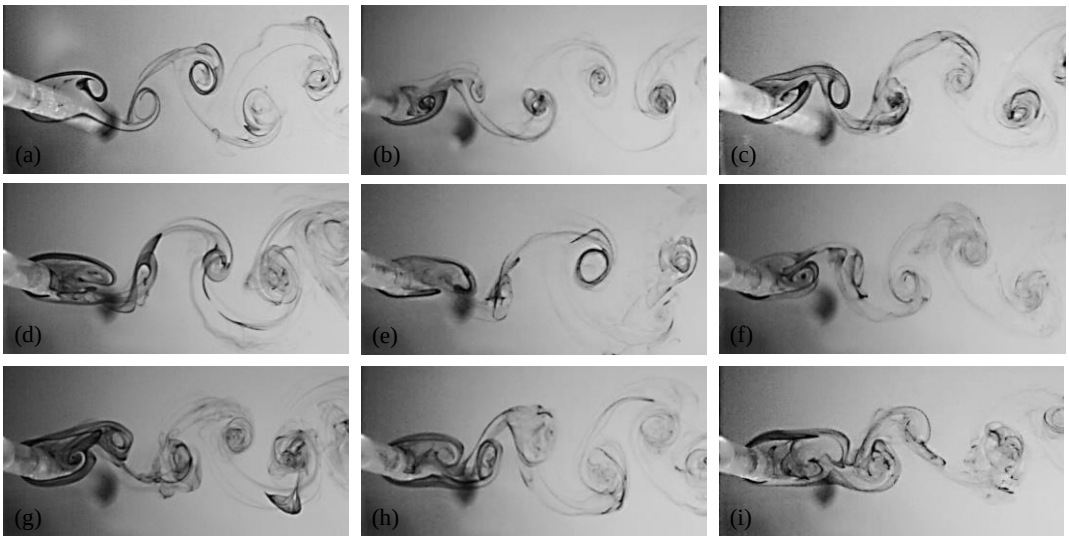

Figure 5.8. Flow visualizations for the oscillating cylinder at a constant rotation rate of α=0.6 and varying reduced velocities: (a) U^*=4.1, (b) U^*=4.8, (c) U^*=5.6, (d) U^*=6.7, (e) U^*=7.4, (f) U^*=8.9, (g) U^*=9.3, (h) U^*=10.1, (i) U^*=10.8.

5.6 Flow forces

Flow forces acting on the cylinder in the crossflow direction were measured using a six-axis force sensor attached to the upper end of the oscillating cylinder. It was of interest to investigate how the cylinder's rotation influenced the flow forces acting on the cylinder at varying reduced velocities in the lock-in range. The force sensor measured the total flow forces acting on the cylinder in both the crossflow and inline directions. The measured force in the crossflow direction comprised both the hydrodynamic flow forces and the inertia force due to the motion of the force sensor. Therefore, the inertia force was removed from the total measured transverse force by post-processing the experimental data. The force sensor measurements were synchronized with the displacement data readings from the non-contacting laser displacement sensor, making it possible to directly obtain the phase difference between the measured flow forces and the displacement of the cylinder in the crossflow direction. Figure 5.9 shows sample time histories and frequency plots of the measured lift and drag forces at a rotation rate of α=0.4 and a reduced velocity of U^*=5.6. As shown in Figure 5.9(b), the frequency content of the lift force consisted of a main harmonic (at a frequency close to the natural frequency of the system) as well as a contribution from a higher harmonic (a frequency three times the first harmonic). The existence of higher harmonics of the flow forces in a rotating cylinder is in agreement with the results reported previously by Bourguet and Lo Jacono (2014). For a non-rotating cylinder, previous studies have shown that due to the oscillations of the cylinder, the relative velocity of the cylinder makes an angle with respect to the oncoming flow. As a consequence of such a relative velocity, higher harmonic components of the flow forces

can exist in the crossflow direction. The existence of the higher harmonic components in the crossflow direction has been discussed with some details by Wang et al. (2003) for a non-rotating cylinder and by Bourguet and Lo Jacono (2014) for a rotating cylinder.

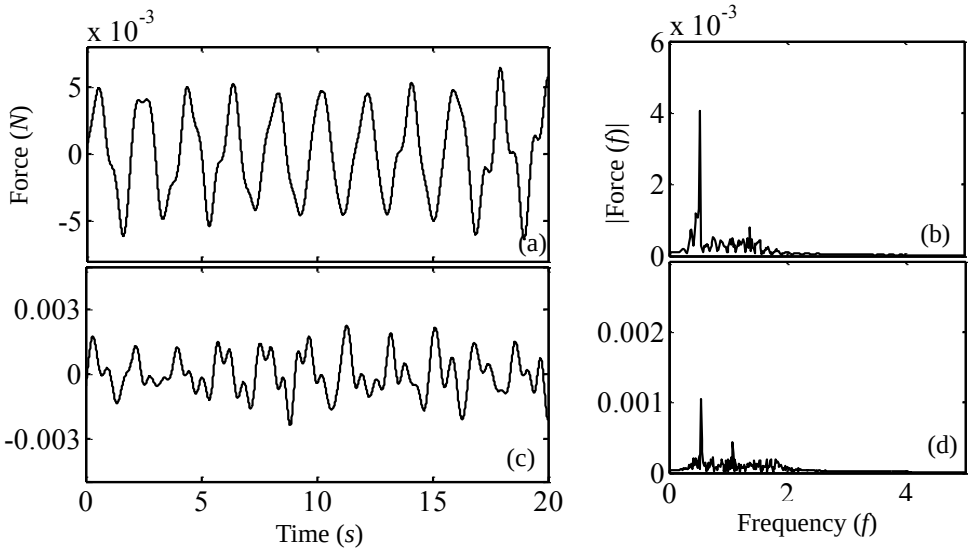

Figure 5.9. Sample time histories and frequency contents of the flow forces in the (a, b) crossflow and (c, d) inline directions.

Figure 5.10(a) shows the fluctuating lift versus the reduced velocity at varying rotation rates (contour plot in Figure 5.10(b)). For a non-rotating cylinder (α=0), the bell-shaped force contribution matched well the previously reported data.(Khalak and Williamson, 1999) As depicted in Figure 5.10, for increasing rotation rates, the range of reduced velocities for which the flow forces excited the cylinder became narrower and the maximum value of the dimensional flow force shifted toward larger reduced velocities at larger rotation rates. The range of reduced velocities for which the flow forces were non-zero matched the lock-in ranges shown in Figure 5.3, as expected.

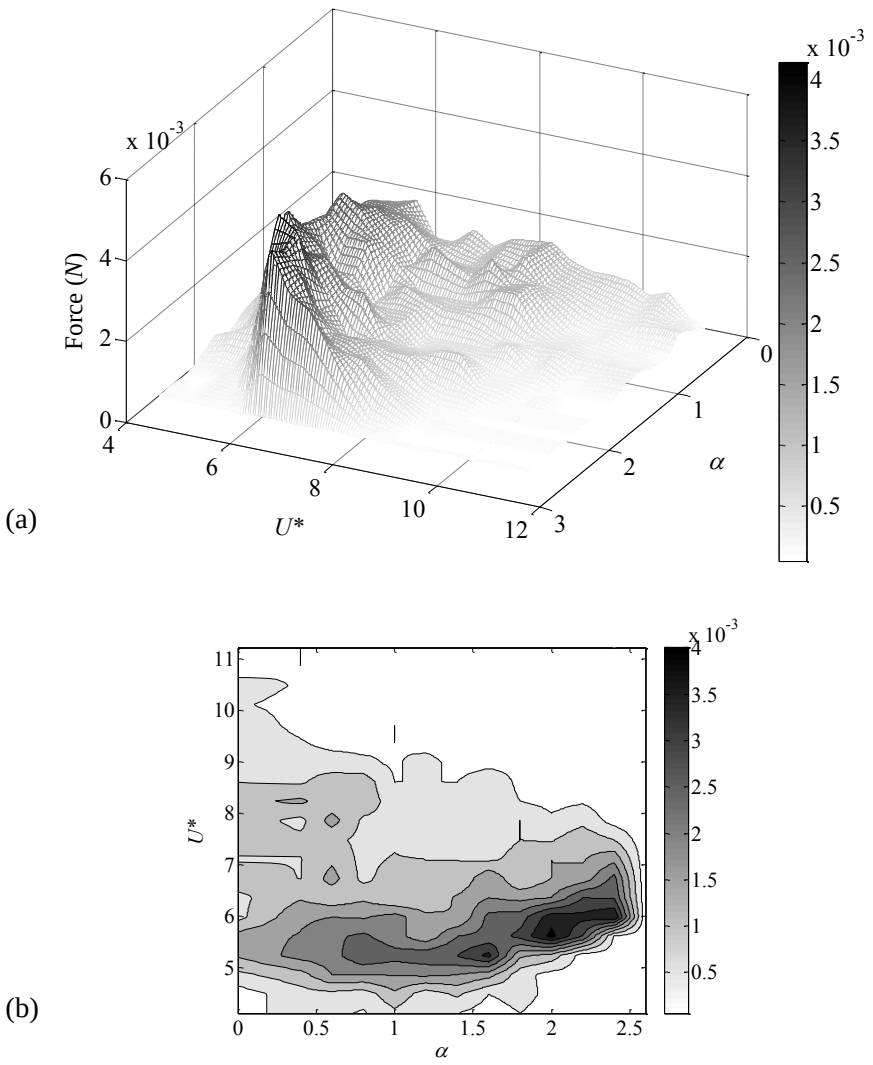

Figure 5.10. (a) Three dimensional and (b) contour plots of flow forces acting on the cylinder in the crossflow direction, versus the reduced velocity, *U**, and the rotation rate, α.

Figure 5.11 shows the mean values of the lift forces. At larger reduced velocities and larger rotation rates, the mean value component of the lift increased. This is in agreement with the plot of mean value of the cylinder displacement shown in Figure 5.5 and also with the wake of the cylinder shown in Figure 5.6, in which a drift in the vortex street existed in the wake of the cylinder at large rotation rates.

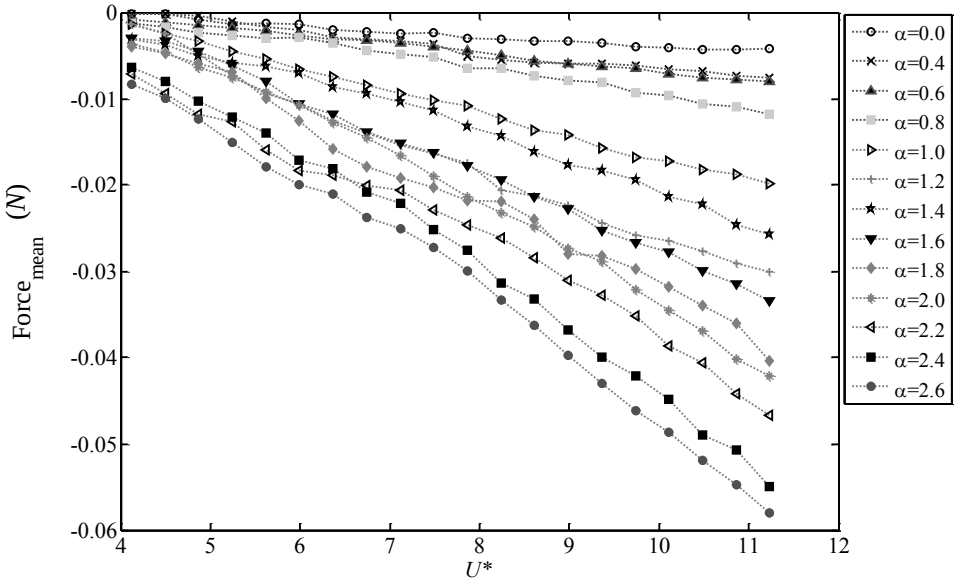

Figure 5.11. Mean value of the flow forces acting on the cylinder in the crossflow direction versus the reduced velocity ($U^*=U/f_{nw}D$) for different rotation rates, α.

The phase differences between the flow force in the crossflow direction and the cylinder displacement are plotted in Figure 5.12. For a non-rotating cylinder (α=0), a phase jump from 0° to 180° occurred at a reduced velocity of $U^*\approx6$. Khalak and Williamson (1999) also observed this phase jump and showed that the phase difference of 0° corresponds to the upper branch response and the phase difference of 180° to the lower branch response. For larger rotation rates, $0.4\leq\alpha\leq1.8$, while the phase difference was still 0° for lower values of reduced velocity, it had values less than 180° after the jump. By increasing the rotation rate, the phase difference at larger reduced velocities decreased. At rotation rates larger than α=1.8, the phase did not show any jump and remained at values less than 90°. The trend observed for the phase difference between the flow forces and displacement of the cylinder can be directly related to the frequency of oscillations: As seen in Figure 5.4, at high rotation rates where the phase jump did not occur, the frequency

of oscillations stayed below the natural frequency of the cylinder. The reason for a decrease in the frequency of oscillations for large rotation rates can be explained by considering the added mass coefficient value at different rotation rates in the lock-in range.

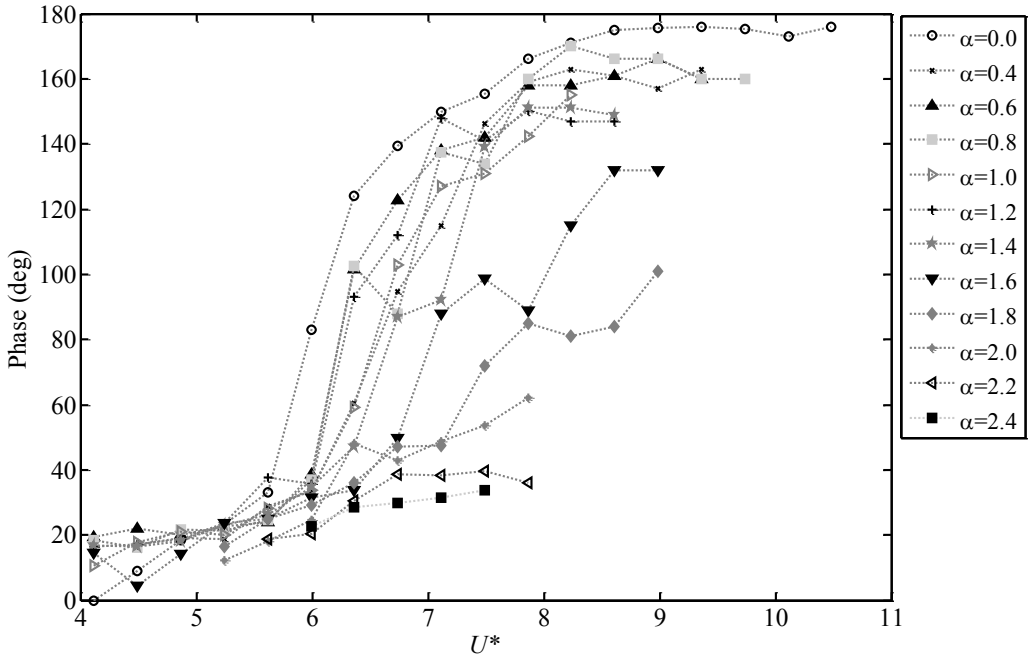

Figure 5.12. Phase difference between the flow force and the displacement in the crossflow direction versus the reduced velocity ($U^*=U/f_{nw}D$) for different rotation rates, α.

The added mass coefficient, C_{ma}, is defined as the added mass normalized with respect to the displaced mass of the surrounding fluid, i.e.

$$C_{ma} = \frac{M_a}{\rho V}, \tag{5.1}$$

where ρ is the flow density, V is the volume of surrounding fluid, and M_a is the added mass. The added mass is defined as the lift force in phase with the cylinder acceleration divided

by the magnitude of acceleration(Huera-Huarte and Bearman, 2009b) and can be calculated for a rotating cylinder as

$$M_a = \frac{F_L \cos(\phi)}{Y_0 (2\pi f_0)^2}, \tag{5.2}$$

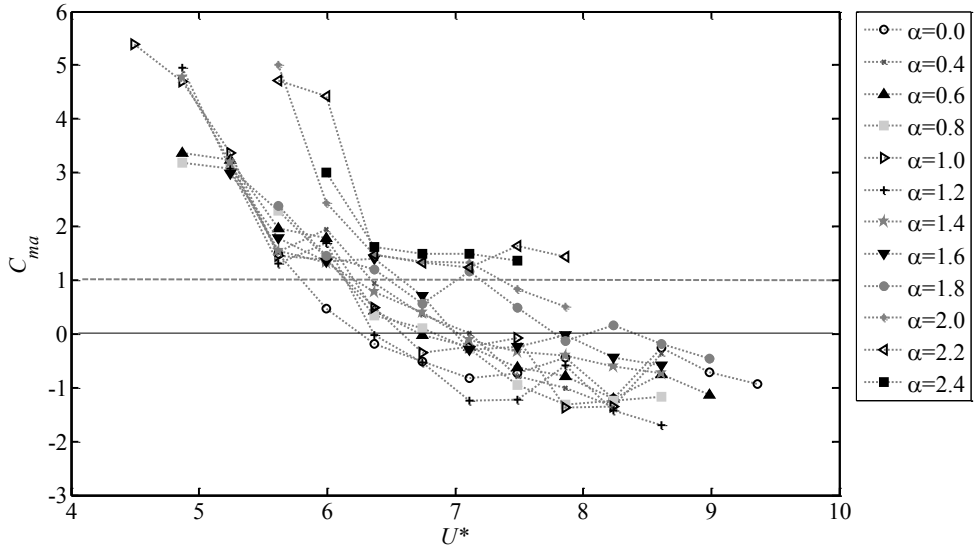

Figure 5.13. Added mass coefficient values versus the reduced velocity ($U^*=U/f_{nw}D$) for different rotation rates, α.

where F_L is the lift force, φ is the phase difference between the lift force and the cylinder oscillations, and Y_0 and f_0 are the magnitude and frequency of oscillations. Figure 5.13 shows the variation of the added mass coefficient for different rotation rates at reduced velocities corresponding to the lock-in range. While the added mass coefficient was negative for low rotation rates at the reduced velocities corresponding to the initial branch, by increasing the rotation rate, the added mass coefficient became positive all along the lock-in range. The unity line corresponds to the added mass coefficient for a non-rotating cylinder based on the potential flow assumption. The positive added mass coefficient at high rotation rates explains why the frequency of oscillations stayed below the natural

frequency of the system (Figure 5.4), and also why smaller phase differences were measured at those high rotation rates (Figure 5.12).

As shown in Figure 5.6, the rotation of the cylinder led to the change in the vortex shedding pattern from 2S vortex shedding for a non-rotating cylinder to P shedding at larger rotation rates of the cylinder. In order to investigate how the flow forces in the inline direction are related to different shedding patterns, here both the magnitude and the dominant frequency of the drag forces are discussed. Drag forces are shown in Figure 5.14 versus reduced velocity at varying rotation rates. For a non-rotating cylinder, the components from the first and the second harmonic (frequencies close to the natural frequency and twice that, respectively) were observed in the lock-in range. The contributions from the first harmonic were originated from the asymmetric vortex shedding of the cylinder.(Du et al., 2014) Overall, the dominant frequency was the second harmonic in the inline direction for a non-rotating cylinder. The change from 2S vortex shedding at low rotation rates to asymmetric P shedding at high rotation rates of the cylinder (shown in Figure 5.6) caused a shift in the dominant frequency in the inline direction from the 2^{nd} harmonic to the 1^{st} harmonic (Figure 5.14). This was also observed numerically by (Bourguet and Lo Jacono (2014)). The contributions from the second harmonic diminished at rotation rates larger than α=1.8, where the entire flow forces in the inline direction had a frequency close to the natural frequency of the system. Also the range of reduced velocities in which the fluctuating flow forces were acting on the cylinder became narrower at larger rotation rates, same as what was observed in the crossflow direction. As shown in Figure 5.14, the magnitude of the inline flow force became larger at higher rotation rates.

This increase in the magnitude of the inline force was in agreement with the vortex shedding pattern where a relatively large pair of vortices was shed during one cycle of cylinder oscillations at higher rotation rates (Figure 5.6).

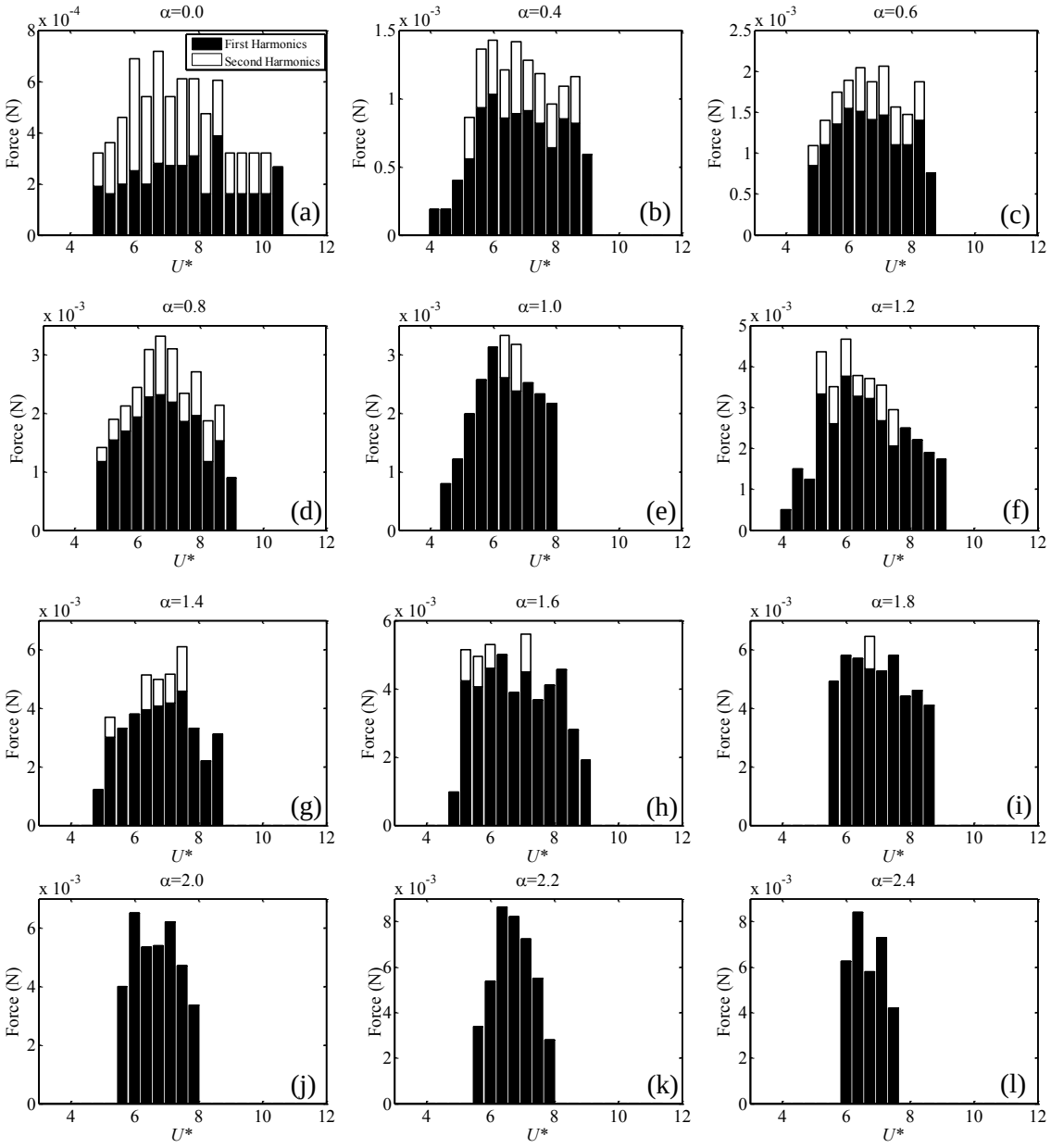

Figure 5.14. Flow forces acting on the cylinder in the inline direction versus the reduced velocity ($U^*=U/f_{nw}D$) at varying rotation rates: (a) α=0.0, (b) α=0.4, (c) α=0.6, (d) α=0.8, (e) α=1.0, (f) α=1.2, (g) α=1.4, (h) α=1.6, (i) α=1.8, (j) α=2.0, (k) α=2.2, (l) α=2.4.

5.7 Conclusions

A series of experiments were conducted to study vortex-induced vibration of a rotating cylinder free to oscillate in the crossflow direction. The cylinder was forced to rotate about its long axis and the influence of different rotation rates on the response of the system was studied in terms of the amplitude and frequency of oscillations as well as the flow forces acting on the cylinder.

The dimensionless amplitude of oscillations for the rotating cylinders stayed around the same value as for the non-rotating cylinders undergoing VIV, implying that the rotation of the cylinder did not significantly influence the amplitude of oscillations. As the rotation rate was increased, the lock-in range became narrower and at the rotation rates beyond α=2.4, the oscillations of the cylinder stopped. As a consequence of the Magnus effect, the mean displacement of the cylinder increased at higher rotation rates and for high reduced velocities. The dimensionless frequency of oscillations stayed around the natural frequency of the system in the lock-in range for all rotation rates of the cylinder.

The asymmetry introduced into the wake was visualized using the dye visualization technique for different rotation rates. At a constant reduced velocity, the von Kármán street for the non-rotating cylinder (2S shedding pattern) was shifted to an asymmetric P shedding pattern at higher rotation rates in which a pair of vortices was shed from one side in every cycle of the cylinder's oscillations. It was also shown that at a constant rotation rate, for a wide range of reduced velocities, the vortex shedding did not cease, but instead, similar to the classical VIV for a non-rotating cylinder, the frequency of vortex shedding was locked into the frequency of oscillations in the range of velocities for which oscillations were

observed. Beyond this range, vortex shedding still existed in the wake of the cylinder but the shedding frequency followed the Strouhal law.

The flow forces acting on the cylinder in the crossflow direction were measured. The maximum flow force at varying rotation rates did not change much compared with the maximum value measured for the non-rotating cylinder. The range of non-zero flow forces also matched the lock-in ranges in the amplitude plots. Similar to the mean displacement of the cylinder, the mean value of the flow forces in the crossflow direction increased at higher reduced velocities and high rotation rates.

The frequency of fluctuating flow forces acting on the cylinder in the inline direction followed the observed shedding frequencies. At low rotation rates, the dominant frequency of flow forces in the inline direction was close to a value twice the natural frequency of the system. This was the region where a 2S vortex shedding was observed. By increasing the rotation rate, the dominant frequency of the inline forces shifted from a value close to twice the natural frequency to a value close to the natural frequency. This shift occurred for the range of rotation rates in which a P vortex shedding was observed.

CHAPTER 6

FROM VORTEX-INDUCED VIBRATIONS TO GALLOPING IN PRISMS WITH TRIANGULAR CROSS-SECTIONS PLACED IN WATER

6.1 Introduction

Flow past a circular cylinder has been studied extensively for a flexibly-mounted rigid cylinder (Bearman, 1984; Blevins, 1990; Sarpkaya, 2004; Williamson and Govardhan, 2004; Vandiver, 2012). Typically, a flexibly-mounted rigid circular cylinder is placed in water or air flow and when the frequency of vortex shedding locks in with the system's natural frequency, as a result of increasing flow velocity, a range of relatively large amplitude oscillations, called the lock-in range, is observed. This is called vortex-induced vibration (VIV). Some other studies have focused on cases in which the cylinder has different cross-section than circular. Most experimental and numerical studies have focused on the square cross-section (Parkinson and Wawzonek, 1981; Obasaju et al., 1990; Naudascher and Wang, 1993; Deniz and Staubli, 1997; Su et al., 2007; Zhao et al., 2013). Early studies by Parkinson and Smith (1964) showed the existence of galloping instability in a square cross section at zero angle of attack (α=0º). Later in an experimental study, Bokaian and Geoola (1984) discussed the existence of mixed modes of vortex-induced vibration (VIV) and galloping in such structures. Recently, in a comprehensive experimental study by Nemes et al. (2012) on a flexibly-mounted square cross-section

cylinder, it has been shown that depending on the angle of attack, the cylinder can undergo either vortex-induced vibration (VIV) or galloping. It was shown that for angles of attack smaller than α=7.5º, the square cylinder experiences galloping. Also, it was observed that the transition from VIV to galloping occurred in a narrow range of angles of attacks, α=7.5º-10 º, mainly due to the jump in the location of the separation point.

While a full map of flow-induced instabilities in square cross-section cylinders has been provided in recent years, there are limited studies in which the flow instability of triangular cylinders has been studied. Most studies on flow past a triangular cross-section cylinder have focused on a fixed cylinder. Mainly the effects of flow (wind) direction as well as the cross-sectional shape have been studied (Kumar De and Dalal, 2006; De and Dalal, 2007; Bao et al., 2010). In a recent study by Tu et al. (2014), two dimensional flow past a stationary cylinder was studied numerically for a wide range of angle of attack in the range of α=0º-60º and Reynolds number range of *Re*=50-160. It was concluded that depending on the incidence angle, the location of separation point changed: for angles of α<30º, the Reynolds number changed the location of separation points while at higher angles, the separation points were located at the rear corners, independent from the Reynolds number. A topological map of flow patterns was also summarized in their work for a stationary triangular cylinder in flow.

Among the studies on triangular cylinders, the rotational oscillations of such prisms have been studied, both numerically and experimentally (Srigrarom and Koh, 2008; Wang et al., 2011). Lock-in region was observed in the numerical study by Tu et al. (2014) for

rotational oscillations of a triangular cross-section cylinder in which 2S and P+S flow patterns were observed to be dominant in the lock-in region at angle of attack of α=0º.

There has been little research into the flow-induced instabilities that occur in pure crossflow oscillations of a triangular cylinder. In an experimental study conducted by Alonso and Meseguer (2006), a two-dimensional triangular cross-section body was placed at different angles of attack in a wind tunnel at a constant flow velocity of V=20 m/s, which resulted in a high Reynolds number of values larger than Re=10^5. Galloping instability of the structure was studied at varying angles of attack as well as different angles of the main vertex of the triangular cross-section. Based on the experimental observations, it was concluded that both of the two parameters studied (angle of attack and cross-section geometry) affected the translational galloping of the triangular cross-section cylinder. A map of potential instability zones was provided that showed the regions in which the body could experience instability based on the variation of the two influencing parameters studied. Three main zones of instability were introduced based on the angle of attack and main vertex angle; the first instability occurred when the base of the triangular faced the wind flow. The second instable zone was observed when the flow reached the sharp main vertex and the third instability was observed when the wind was aligned to the lateral sides of the triangular. Alonso et al. (2012) also studied the existence of hysteresis in the galloping of triangular cross-section cylinders in wind tunnel experiments. Hysteresis was found to exist at the angles of attack where there were inflection points in the lift coefficient curve (Alonso et al., 2012). In a numerical simulation of laminar flow (Re=100) past an oscillating triangular cylinder, the influence of different frequencies of oscillations as well

as oscillating amplitudes on the lift and drag forces acting on a triangular cylinder were studied (Alawadhi, 2013). It was concluded that when the frequency of oscillation is close to the Strouhal number of a stationary triangular cylinder, the RMS value of lift coefficient reaches its maximum values.

Due to the limited studies conducted on a triangular cylinder free to oscillate in the crossflow direction, there still exists a need to cover a full map of different responses of the triangular cylinder at varying angles of attack and different flow velocities. In the present work, we experimentally investigate the influence of different angles of attack as well as varying flow velocities on the pure translational oscillations of a triangular cylinder. The experiments took place in a re-circulating water tunnel. The triangular cylinder was free to oscillate in the crossflow direction and its behavior was studied over a range of angles of attack of $0^o<\alpha<60^o$, reduced velocities of $4<U^*<22$, and Reynolds numbers of $488<Re<2682$. Dye flow visualization was conducted in the course of these experiments to capture different wake patterns and map them with different observed instabilities.

6.2 Experimental set-up and method

An equilateral triangular cylinder with sides of D=16 mm and a length of L=29.2 cm (L/D=18.25) was tested for several angles of attack, from 0^o to 60^o, with increments of 5^o (Figure 6.1). The cylinder was machined out of Aluminum 6061 and each side was further grounded, yielding a smooth surface. The recirculating water tunnel used featured a test-section of 1.27m×0.5m×0.38m and a turbulence intensity of less than 1% for flow velocities up to 0.3 m/s. Attached to the bottom of the cylinder was a 115 mm diameter circular endplate with a thickness of approximately 2 mm and tapered edges. This plate

reduced end effects while maintaining a streamlined profile. The cylinder was then attached to an air bearing set-up, free to oscillate in the transverse direction (crossflow direction), as seen in Figure 6.2. The 1D air-bearing set-up had two air bearings to reduce the damping and to constrain the oscillations of the cylinder to one degree of freedom in the crossflow direction (Figure 6.2). Springs were attached from the cylinder to a fixed housing. This set-up was used previously by Seyed-Aghazadeh et al. (2014) to study VIV of tapered cylinders in which the response of a uniform circular cylinder was shown to be in agreement with the results of Khalak and Williamson (1999).

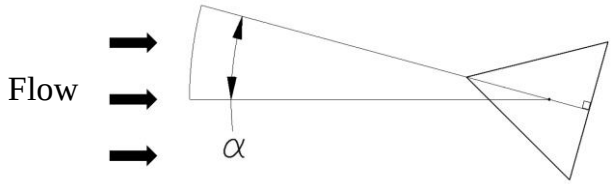

Figure 6.1. Flow direction and the angle of attack.

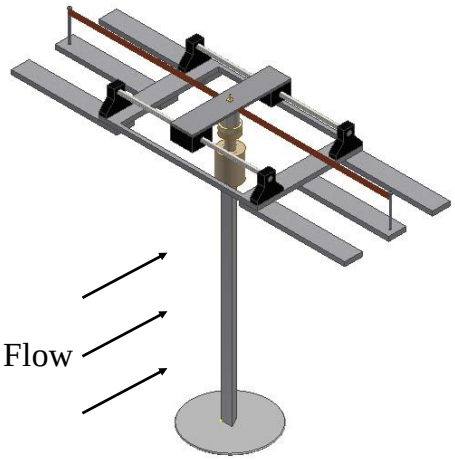

Figure 6.2. Schematic of the experimental set-up.

For comparison, a circular cylinder was also manufactured. Made of Aluminum 6061, the piece was lathed down to diameter of D=16 mm and the same length L=29.2 cm.

A 200 g dummy mass was used to adjust the mass ratio of the circular cylinder to that of the triangular cylinder, $m^* = 9.24$ ($m^* = 4m/\pi\rho D^2 L$, where m is the total moving mass of the system, L the cylinder length, D its diameter, and ρ the flow density). All moving parts were accounted for in this calculation, including the dummy mass, air bearings, mounting bracket, force sensor and various cabling.

Data were recorded for this experiment via two different sensors. The first, a Micro-Epsilon ILD 1402-600 non-contacting displacement sensor, recorded the transverse displacements. This sensor ran in tandem with an ATI-Nano17/IP68 six-axis force sensor that was attached to the upper end of the oscillating cylinder and measured the total flow forces acting on the cylinder in three perpendicular directions. This set-up enabled a complete measurement of the lift and drag forces acting on the cylinder. For the entire assembly, decay tests in water yielded a natural frequency of $f_{nw\text{-}T}$=0.466 Hz and $f_{nw\text{-}C}$=0.5 Hz for the triangular and uniform cylinder, respectively. The damping coefficient was found to be ζ=0.01.

6.3 Experimental Results

6.3.1 The amplitude and frequency response

Figure 6.3 shows the amplitude of oscillations versus reduced velocity for a triangular cylinder at varying angles of attack. The amplitude of oscillations for a uniform circular cylinder, free to oscillate in the crossflow direction with the same mass ratio as the triangular cylinder, is plotted in the figure as well. At angles of attack smaller than α=25º, no oscillation was observed in the entire reduced velocity range tested. At an angle of attack

of α=25º, oscillations with very small amplitudes were observed were observed for reduced velocity of 8.7<*U**<10.7. At slightly larger angles of attack, α=30º and α=35º, there existed a range of reduced velocities, 7<*U**<14.5, where the cylinder oscillated with amplitudes that reached a maximum value of *A**~0.6. This oscillation within a range of reduced velocities resembled the lock-in region observed in the VIV response of a circular cylinder. No oscillation was observed in the reduced velocity range of 14.5<*U**<19.5. At higher reduced velocities, in the range of 19.5<*U**<22, the cylinder started to oscillate again and the amplitude of oscillations increased by increasing reduced velocity. For angles of attack larger than α=35º, when the cylinder started to oscillate, the amplitude of oscillations increased continuously with increasing reduced velocities up to the maximum values tested. For these angles no lock-in range was observed. This continuous increase of amplitudes resembled those seen in galloping of asymmetric structures. These large amplitude oscillations reached a value of A*~3.7 for the case when the base plane of the cross-section was completely perpendicular to the incoming flow direction (α=60º).

Figure 6.4 shows the sample displacement time histories and their corresponding FFT plots at three different reduced velocities of *U**=10.7, 16.7 and 20.7 for two angles of attack: α=30º and 55º (marked with larger symbols in Figure 6.3). While the mean peak in all of these FFT plots corresponds to a frequency close to the natural frequency of the system in water, small contributions of the second harmonic is observed in some cases. This second harmonic contribution is due to the asymmetry in the shedding vortices, as discussed later in Section 6.3.3.

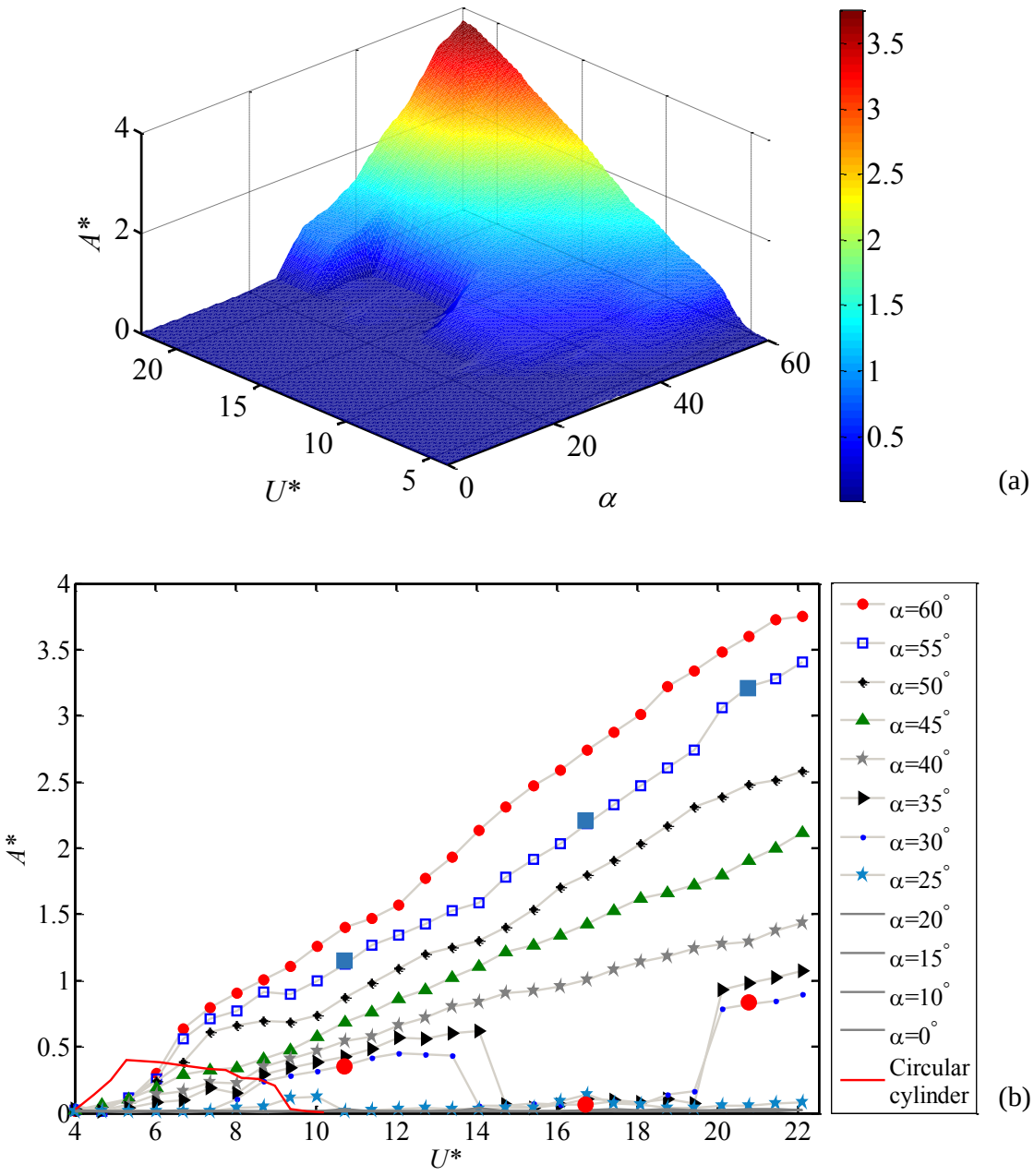

Figure 6.3. (a) Three-dimensional and (b) projected plots of the dimensionless amplitude of the crossflow oscillations ($A^*=A/D$) versus the reduced velocity, U^*, and the angle of attack, α.

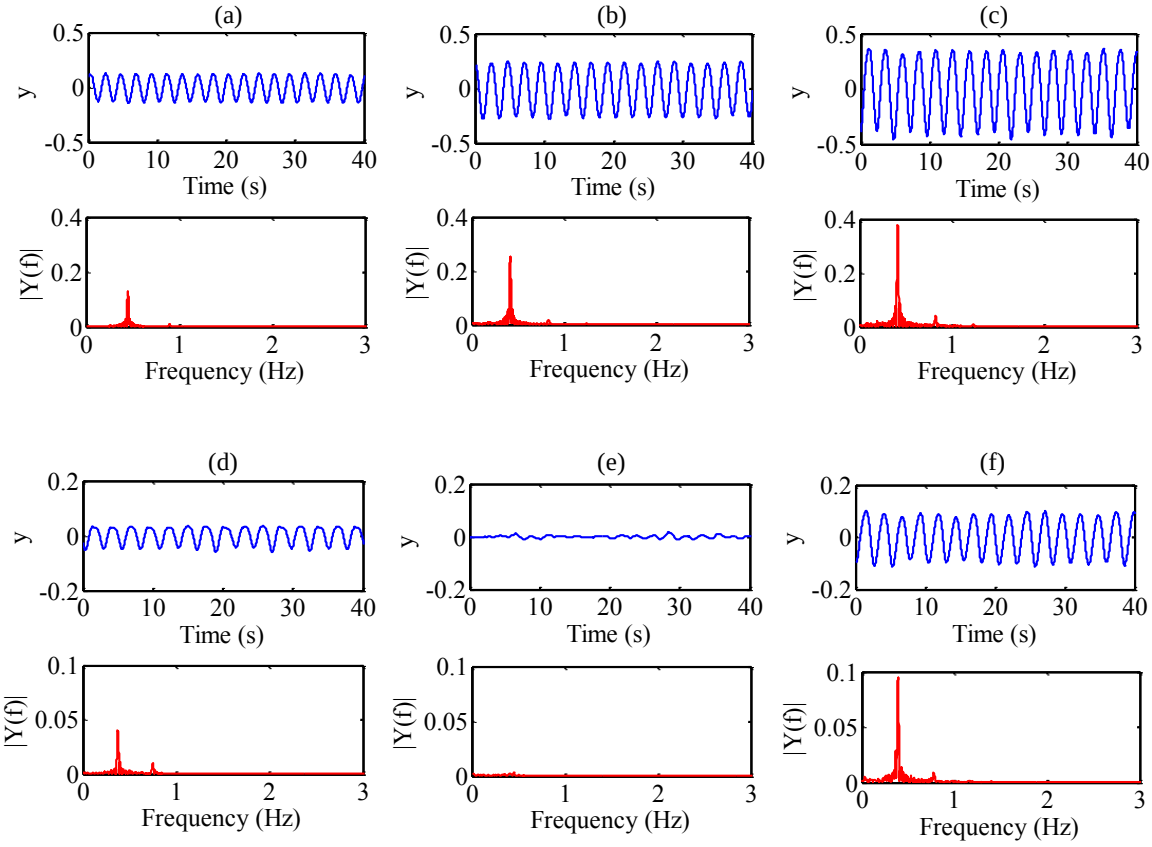

Figure 6.4. Sample time histories and FFT plots of the cylinder's displacement at (a-c) α=30º and (d-f) α=55º at three reduced velocities: first column U^*=10.7, second column U^*=16.7, and the third column U^*=20.7.

Figure 6.5 shows the dominant frequency of oscillations normalized by the system's natural frequency in water ($f_{os}/f_{nw\text{-}T}$) versus reduced velocity for varying angles of attack. The frequencies of oscillations stayed below the natural frequency of the system in water for all angles of attack. This behavior is different from the case of a circular cylinder in which the frequency of oscillations exceeds the natural frequency values in the lock-in region (Khalak and Williamson, 1999). The fact that $f_{os}/f_{nw\text{-}T}$ stayed at values smaller than one means that the jump from 0° to 180° in phasing between flow forces and the cylinder

displacement that is normally observed for a circular cylinder, was not observed for triangular cylinders. Instead the phase varied monotonically from around 0° to around 40°. Bourguet and Lo Jacono (2014) has observed a similar phenomenon for a rotating cylinder in flow.

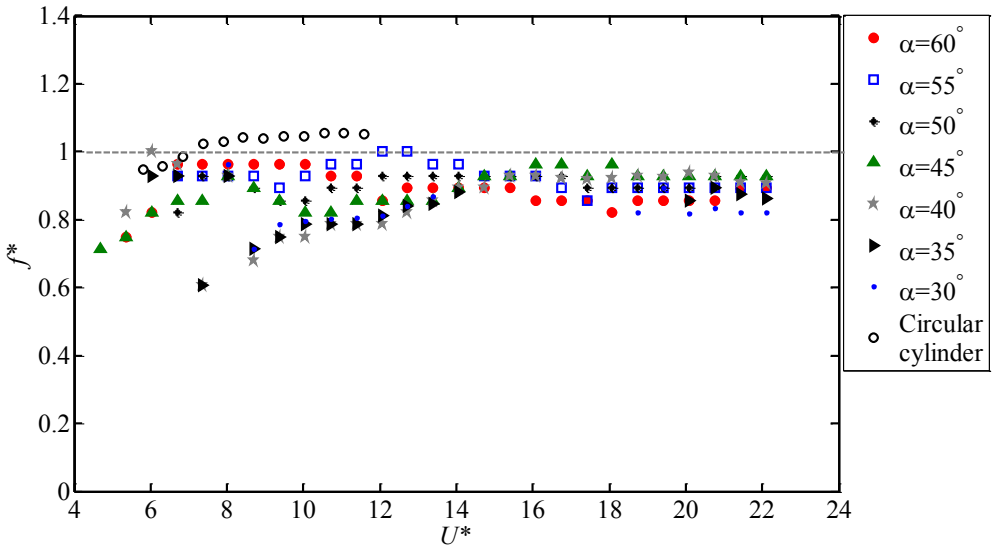

Figure 6.5. Dimensionless frequency of the crossflow oscillations ($f^*=f_{osc}/f_{na}$) versus the reduced velocity ($U^*=U/f_{nw}D$) at different angles of attack α.

Figure 6.6 shows the cylinder's mean displacement values versus reduced velocity for different angles of attack. As expected, the maximum values occurred at angles of attack for which the cylinder was in its most asymmetric orientation with respect to the incoming flow direction (i.e., α~30º). The mean displacement also increased by increasing reduced velocity at each angle of attack.

6.3.2 Flow forces

The force sensor attached to the top of the cylinder measured the total flow forces acting on the cylinder in both the crossflow and inline directions. The measured force in

the crossflow direction comprised both the hydrodynamic flow forces and the inertia force due to the motion of the force sensor.

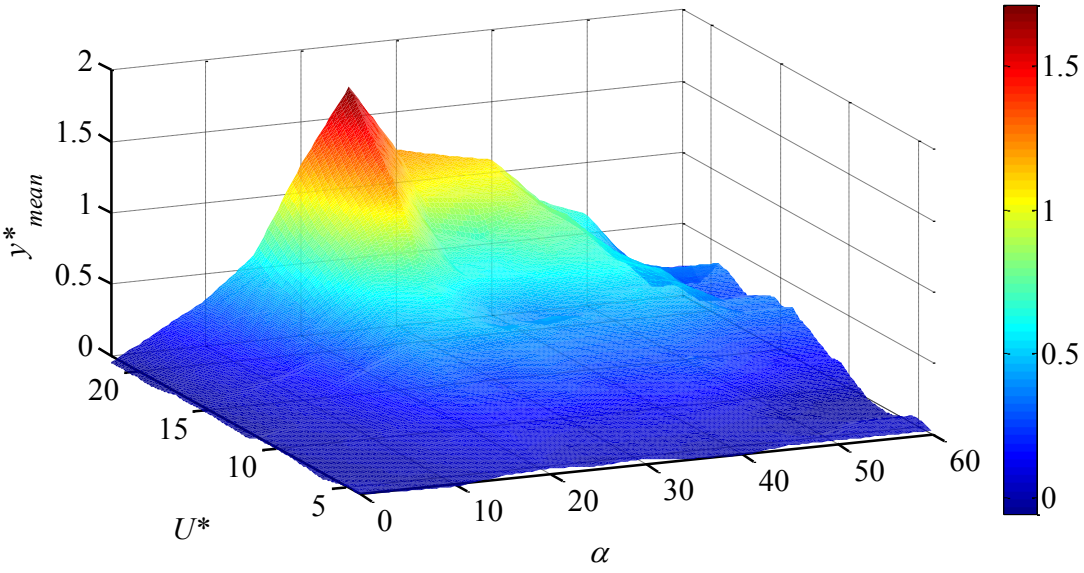

Figure 6.6. Dimensionless mean amplitude of the crossflow oscillations ($y^*_{mean}=y_{mean}/D$) versus the reduced velocity ($U^*=U/f_{nw}D$) at different angles of attack, α.

Therefore, the inertia force needed to be removed from the total measured transverse force by post-processing the experimental data. As the cylinder underwent large-amplitude oscillations, large inertia forces were generated during the oscillations of the cylinder. Subtracting such large forces from the total force measurements introduced large errors in the net crossflow force calculations. On this basis, an alternative method was used here to obtain the flow forces in the crossflow direction. Given the time series of the cylinder's crossflow displacement, it becomes possible to extract the lift forces as

$$F = m\left(\ddot{y} + 2\zeta\omega_n\dot{y} + \omega_n^2 y\right), \tag{6.1}$$

where F is the lift force, m is the system mass, ω_n the natural frequency in air, ζ the damping coefficient (0.01) and y the displacement data recorded using the non-contacting laser. This force reconstruction method was previously used by Seyed-Aghazadeh et al. (2014) to measure the flow forces acting on a tapered cylinder. The results were shown to match very well with the results of direct measurements using a force sensor and also with those of Khalak and Williamson (1999) for a uniform cylinder with a similar mass-damping ratio.

Figure 6.7 and Figure 6.8 show sample lift and drag time histories as well as their corresponding FFT plots at three different reduced velocities of U^*=10.7, 16.7 and 20.7 for two angles of attack of α=30º, 55º. These points are marked in Figure 6.3 with large symbols and have been studied in Figure 6.4 in terms of the frequency of oscillations. At a reduced velocity of U^*=10.7 for an angle of attack of α=30º (Figure 6.7(a)), the lift force consisted of the main harmonic (at a frequency close to the natural frequency of the system) as well as the second harmonic (twice the natural frequency of the system). This is a sample point in which the amplitude of oscillations resembled the VIV response. As previously shown by Du et al. (2014), for a circular cylinder undergoing VIV, while the first peak in the FFT of the crossflow forces corresponds to the main frequency of oscillations, the second peak at the second harmonic is related to the asymmetric shedding in the wake of the cylinder. For the reduced velocity of U^*=16.7, the lift force had a very small value, which corresponded to the zero amplitude of oscillations observed in Figure 6.3. For a larger reduced velocity of U^*=20.7, the lift force consisted of the main harmonic as well as contributions from higher harmonics (multiple integers of the first harmonic i.e., the 2nd, 3rd and 4th harmonics in this case). This sample point falls into the reduced velocity range

in which the amplitude of oscillations resembled the galloping response. The high-frequency flow forces are due to the vortex shedding than are observed at frequencies higher than the frequency of oscillations in the galloping response. For an angle of attack of α=55º, at a reduced velocity of U^*=10.7, the lift force mainly consisted of the first and the second harmonics and a slight contribution of the third harmonics was also observed. At higher reduced velocities of U^*=16.7 and 20.7, large higher harmonic contributions in the lift force were observed. These reduced velocities corresponded to the range of large amplitude galloping-like response of the system. The FFTs of the drag forces shown in Figure 6.8 also followed a similar trend as the lift force; i.e., while mainly the first and the second harmonics of the drag forces were observed for the VIV response of the system (Figure 6.8(a)), high frequency components of the flow forces were observed in the range corresponding to the galloping response.

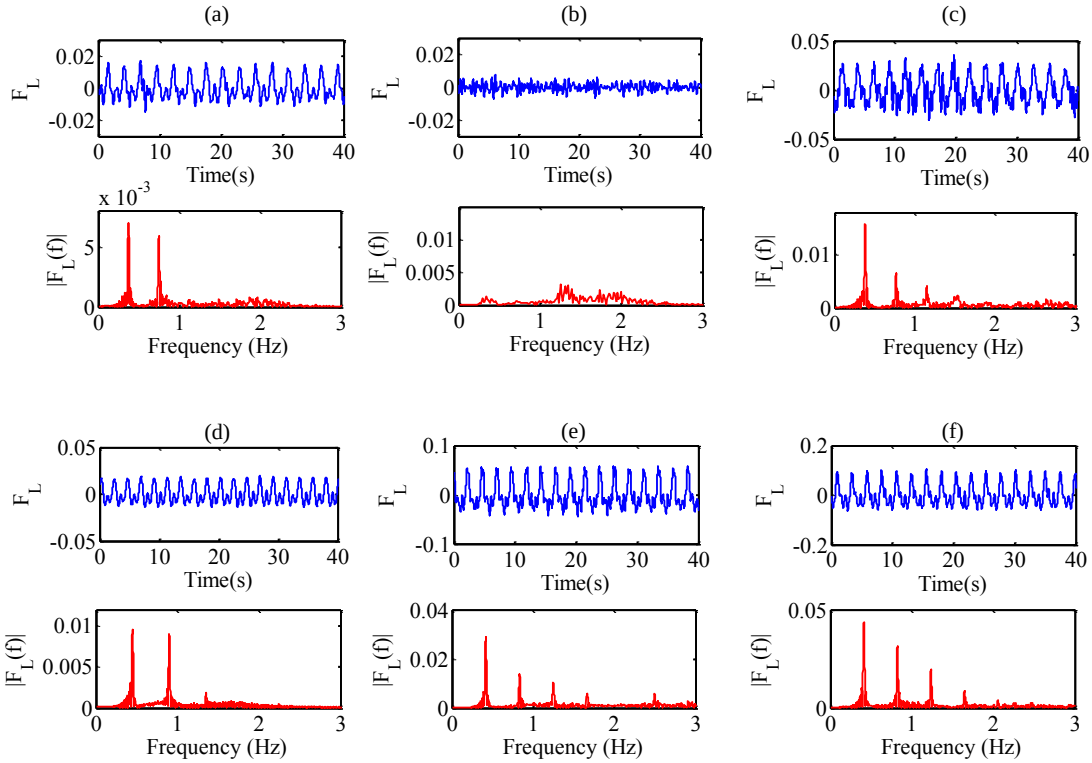

Figure 6.7. Sample time histories and FFT plots of the fluctuating flow forces acting on the cylinder in the crossflow direction at (a-c) α=30º and (d-f) α=55º at three reduced velocities: first column U^*=10.7, second column U^*=16.7, and the third column U^*=20.7.

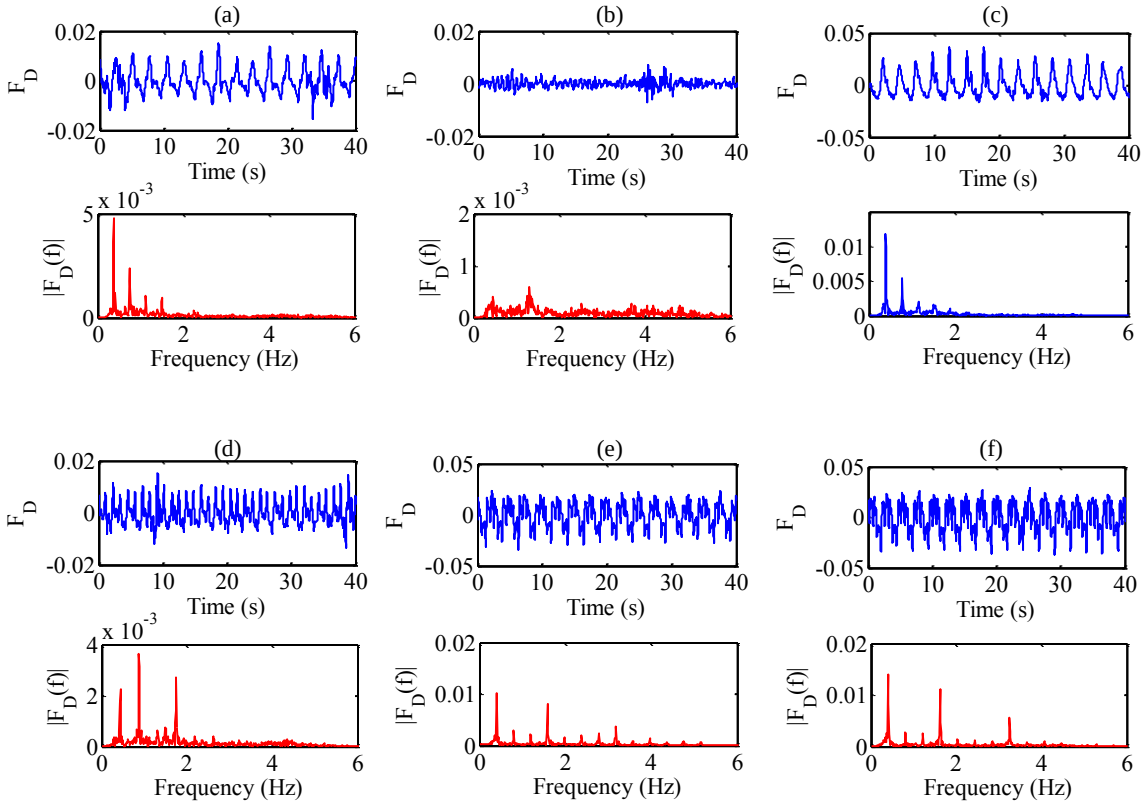

Figure 6.8. Sample time histories and FFT plots of the fluctuating flow forces acting on the cylinder in the inline direction at (a-c) α=30º and (d-f) α=55º at three reduced velocities: first column U^*=10.7, second column U^*=16.7, and the third column U^*=20.7.

In Figure 6.9, the fluctuating lift forces are shown versus reduced velocity at varying angles of attack. The flow forces in the crossflow direction, reconstructed from displacement data, followed well the trend seen in the crossflow displacement of the cylinder (Figure 6.3). The fluctuating lift force increased at higher reduced velocities at a constant angle of attack. Also, the fluctuating lift increased and reached its maximum values at high reduced velocities in the case of α=60º. For a circular cylinder, the bell-shaped force contribution shown in Figure 6.9(b) matched well the previously reported data (Khalak and Williamson, 1999). The flow forces acting in the inline direction are

plotted in Figure 6.10 for different reduced velocities at different angles of attack. Similar trend as the one seen for the lift forces was observed in the inline direction, as well.

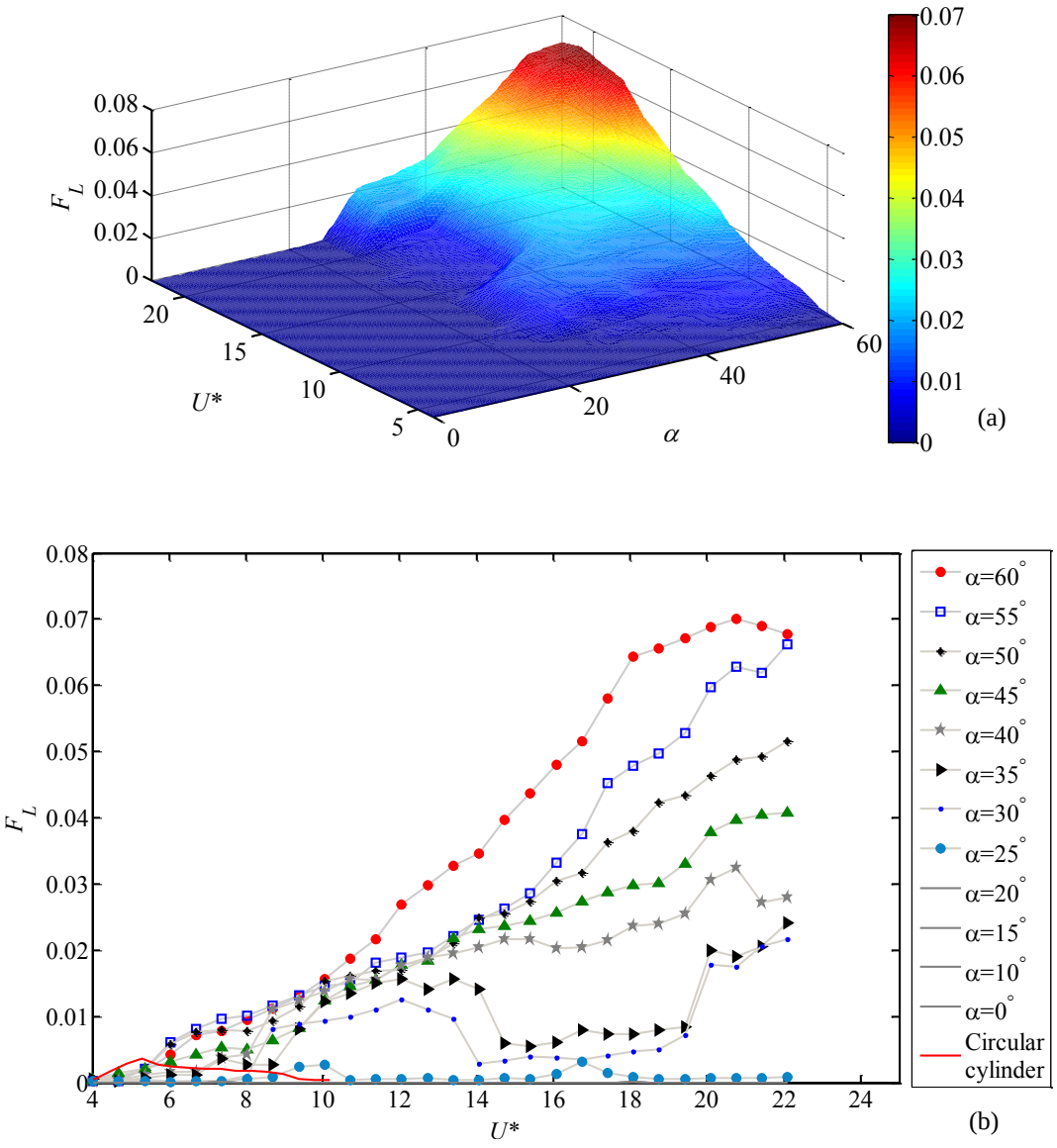

Figure 6.9. (a) Three-dimensional and (b) projected plot of the fluctuating flow forces acting on the cylinder in the crossflow direction versus the reduced velocity, U^*, and the angle of attack, α.

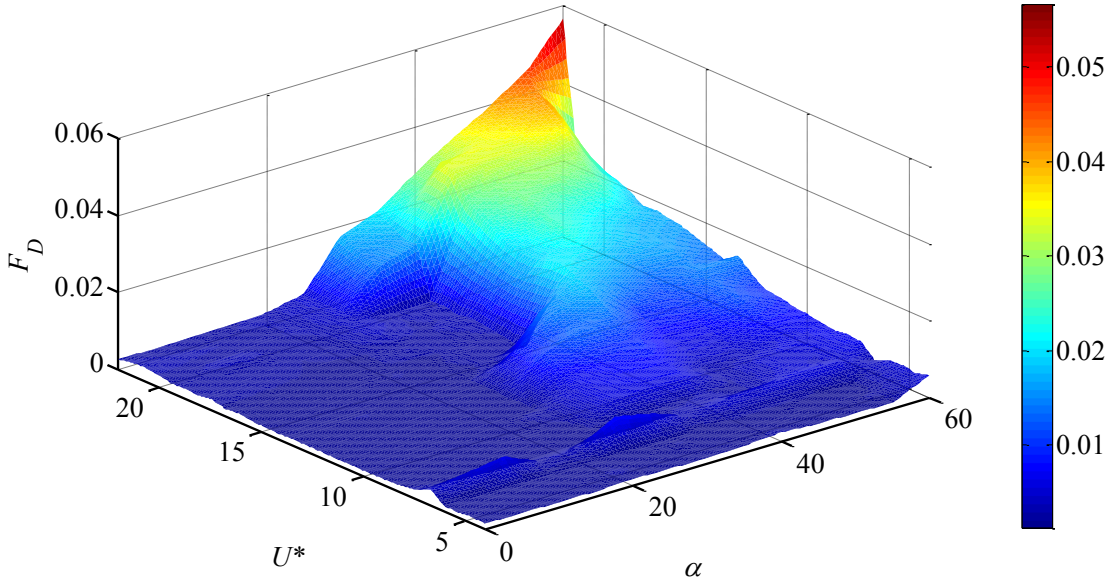

Figure 6.10. Three-dimensional plot of the fluctuating flow forces acting on the cylinder in the inline direction versus the reduced velocity, U^*, and the angle of attack, α.

Figure 6.11 shows the mean values of the lift and drag forces versus the reduced velocity at varying angles of attack. The trend observed here is in agreement with the plot of mean value of the cylinder's displacement shown in Figure 6.6. In the inline direction, at larger reduced velocities and larger angles of attack, the mean value component of the drag increased. The maximum mean drag corresponded to the case where a flat face of the triangular cylinder was facing the incoming flow (α=60º).

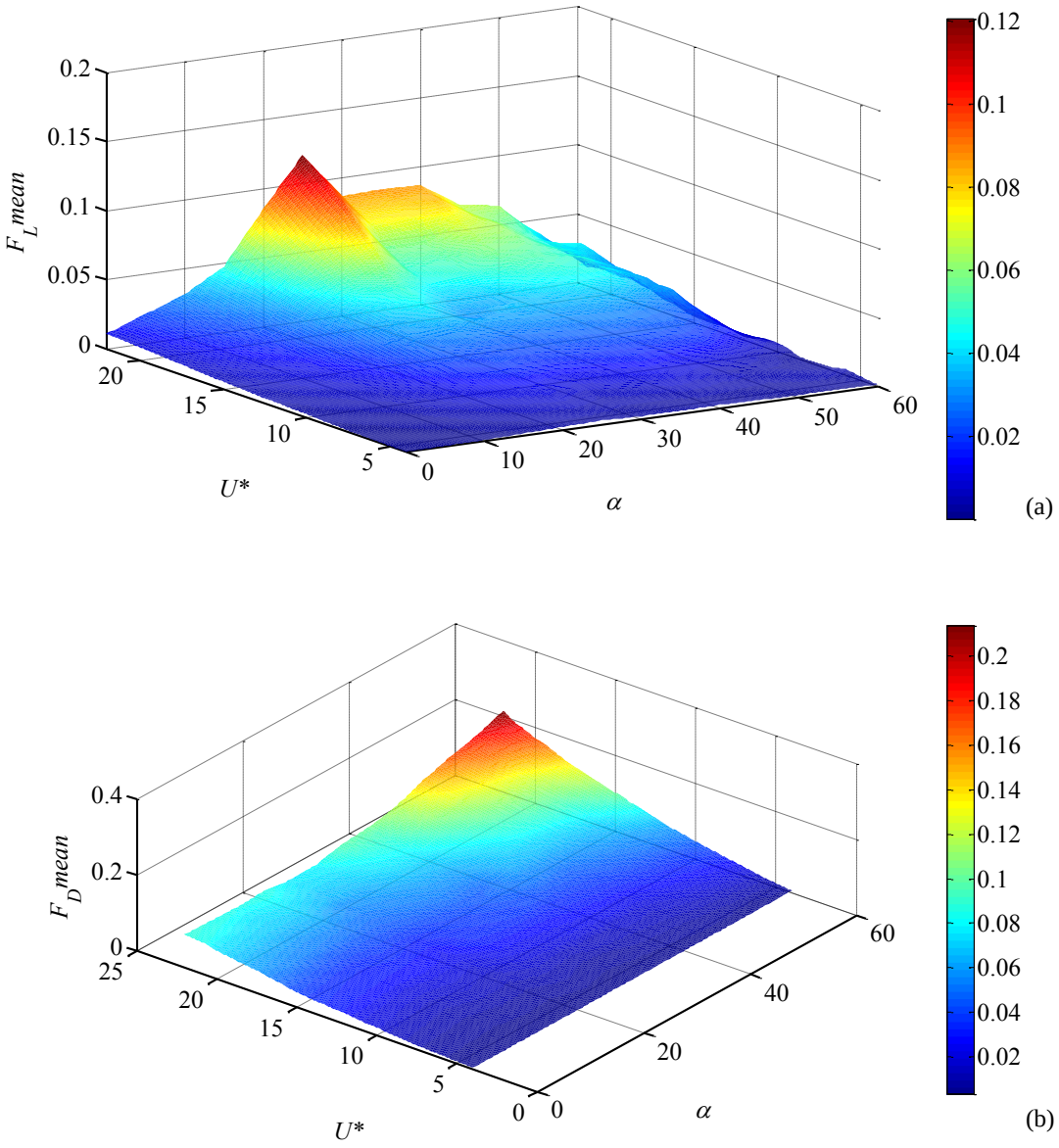

Figure 6.11. Mean value of the flow forces acting on the cylinder in the (a) crossflow and (b) inline direction versus the reduced velocity ($U^*=U/f_{nw}D$) for different angles of attack, α.

6.3.3 The wake

For a triangular cylinder with a degree of freedom to oscillate in the crossflow direction, dye flow visualizations were conducted to investigate how different angles of attack as well as oscillations of the cylinder influenced the vortex shedding pattern. The wake of the cylinder was studied at eight different reduced velocities of U^*=6.7, 8.7, 10.7, 12.7, 14.7, 16.7, 18.7, 20.7 for all angles of attack tested here. The selected reduced velocities covered the range where different responses (VIV, no oscillations and galloping) were observed as shown in Figure 6.3.

A full map of the wake patterns for a triangular cylinder at different angles of attack and different reduced velocities is provided in Figure 6.12. Several different vortex shedding patterns were observed in the wake of the triangular cylinder undergoing VIV and galloping. Sample snapshots of different observed wakes are shown in Figure 6.13 in which each shedding pattern observed in the course of these experiments is demonstrated for one cycle of cylinder's oscillations.

First, the wake of the cylinder is studied for the angles of attack in which both VIV and galloping were observed (α=30º and 35º). As shown in Figure 6.12, two single vortices were shed in each cycle of oscillation (2S pattern) in a wide range of reduced velocities up to U^*=14.7. The wake of the triangular cylinder at α=35º and U^*=6.7 is shown in Figure 6.13 as a sample case in which 2S shedding was observed. The vortex shedding frequencies within the lock-in range were measured and were equal to the frequency of oscillations (f_{vs}~f_{os}=0.35 at U^*=10.7). This observation is in agreement with the frequency content of the lift and drag forces shown in Figure 6.7 andFigure 6.8(a). Two peaks were

observed in the FFT plot of the lift and drag forces at the main frequency and the second harmonic. While the main frequency corresponded to the main frequency of vortex shedding (2S), the second peak at the second harmonic can be related to the asymmetric shedding in the wake of the cylinder (Du et al., 2014). In the range of U^*=14.5-19.5, the 2S vortex shedding persisted but the shedding frequency no longer followed the natural frequency of the system as in this range of reduced velocities, no oscillation was observed. Instead, the shedding frequency matched the Strouhal frequency for a stationary triangular cylinder as expected for a stationary cylinder in flow. For example, at U^*=18.7 the 2S shedding frequency was equal to f_{vs}~1.7 Hz, which was different from the natural frequency of the system (f_N=0.466 Hz), but was equal to the Strouhal frequency for a stationary triangular cylinder, f_{st}= 1.75, based on St=0.2, reported in Tu et al. (2014).

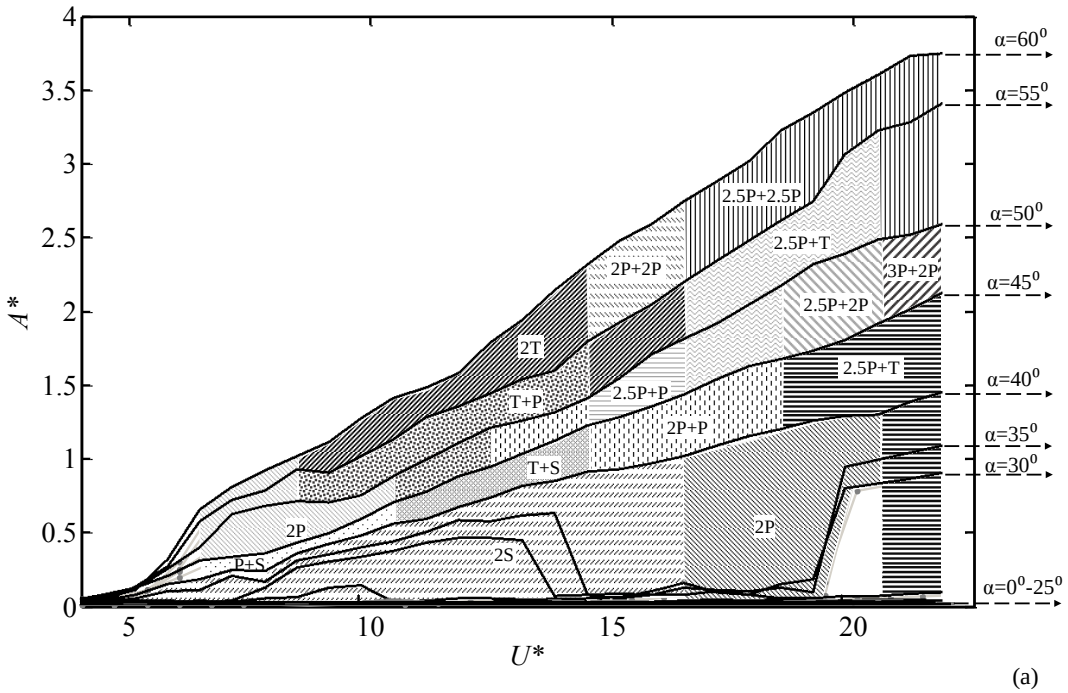

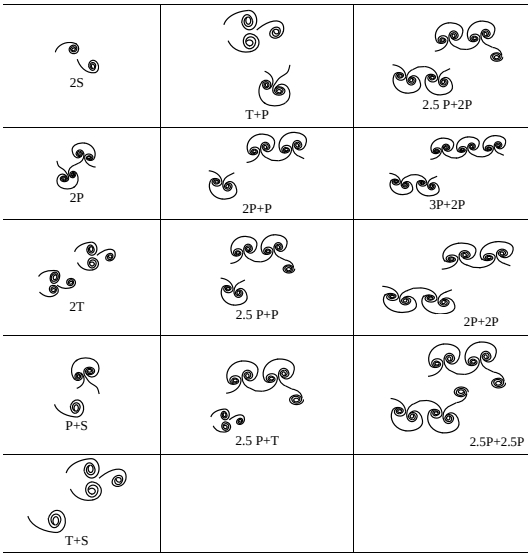

Figure 6.12. (a) Map of the vortex patterns in the wake of the triangular cylinder at varying angles of attack and different reduced velocities, (b) schematics of the introduced shedding patterns.

At larger flow velocities in the range of U^*=19.5-22, the cylinder started to oscillate again and the amplitude of oscillation increased with increasing U^*. Figure 6.13 shows the wake of the cylinder at a representative point within this region, U^*=20.7, in which two pairs and one single vortices were shed from one side when the cylinder was moving up and a triplet from the other side of the cylinder when it was moving down. We call this pattern (2.5P+T). Peaks at higher harmonics of lift and drag forces observed at FFT plots of this case (Figure 6.7 and Figure 6.8) of galloping are in agreement with the high frequency shedding modes observed at this region (2.5P+T).

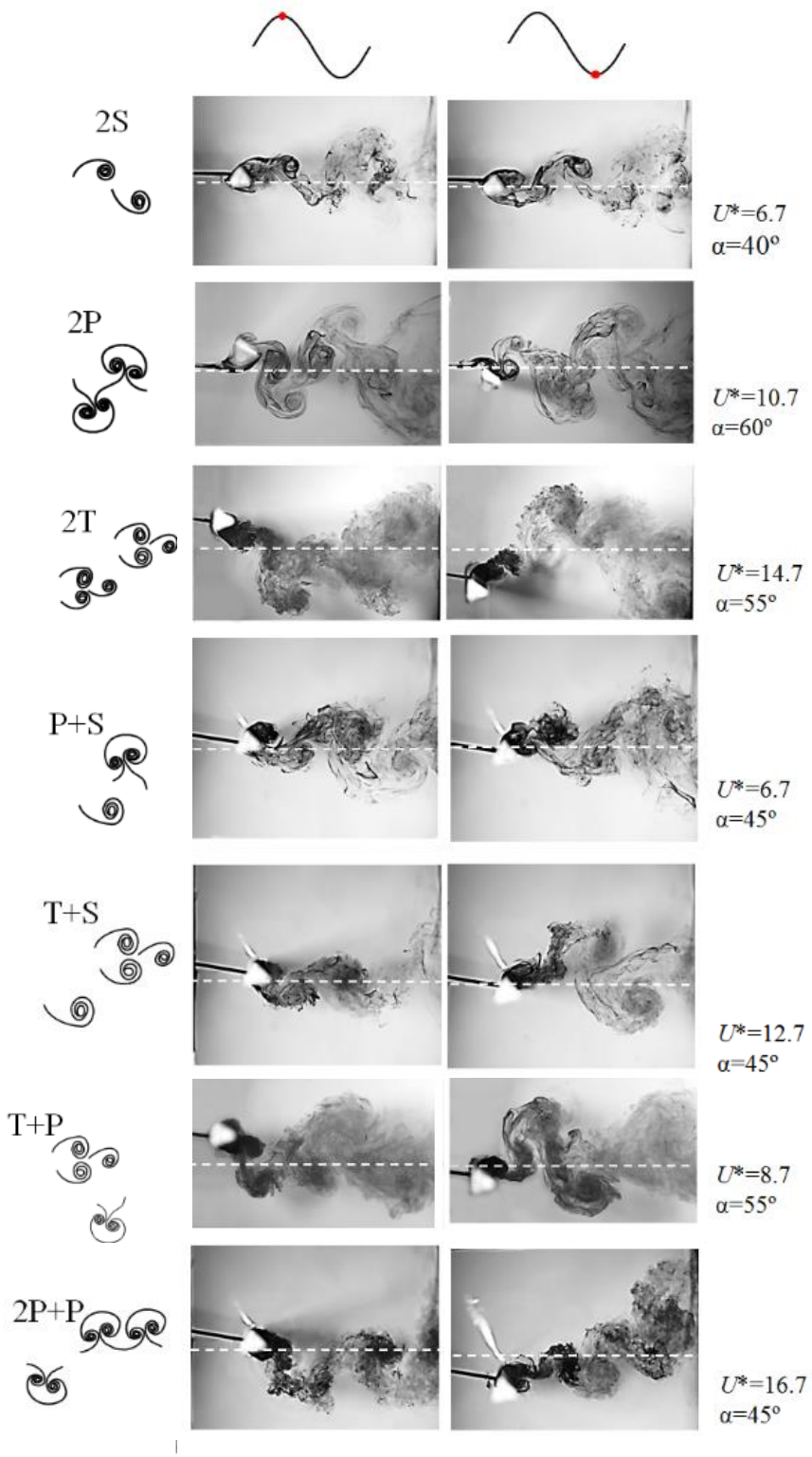
2S
U*=6.7
α=40°
2P
U*=10.7
α=60°
2T
U*=14.7
α=55°
P+S
U*=6.7
α=45°
T+S
U*=12.7
α=45°
T+P
U*=8.7
α=55°
2P+P
U*=16.7
α=45°

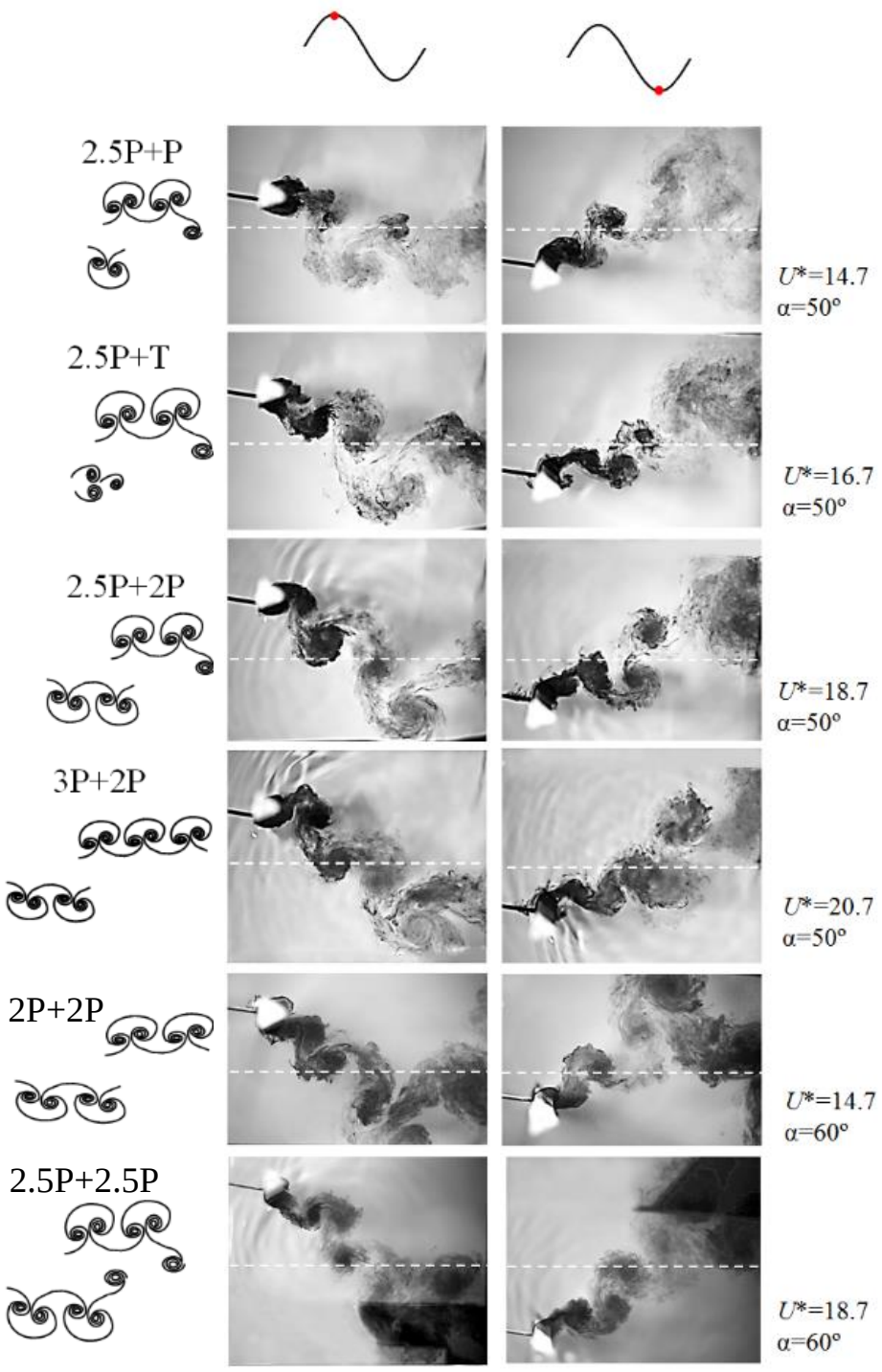

Figure 6.13. The shedding patterns observed in the wake of oscillating triangular cylinder at varying angles of attack and different reduced velocities. The flow direction is from left to right.

At larger angles of attack, where the triangular cylinder experienced galloping-like oscillations, several different shedding patterns were observed. While 2P and 2T patterns (two pairs of vortices and two triplets of vortices shed in one cycle of cylinder's oscillations) are in common with shedding modes observed previously in VIV of circular cylinders (Williamson and Govardhan, 2004), several new shedding patterns were observed in the wake of a triangular cylinder. Schematics of these patterns are given next to the experimental shedding snapshots in Figure 6.12.

In the reduced velocity range of U^*=6.7-8.7 at α=45º, a P+S shedding pattern was observed in which a pair of vortices was shed from one side and a single vortex from the other side of the cylinder. At the same angle of attack, but for higher reduced velocities of U^*=10.7-12.7, a T+S shedding pattern was observed, which consisted of a triplet of vortices shed from one side and a single vortex from the other side of the cylinder. A T+P pattern in which a triplet of vortices was shed when the cylinder moved up and a pair of vortices was shed when the cylinder moved down, was observed at the reduced velocity range of U^*=8.7-12.7 for an angle of attack of α=55º. At higher reduced velocities (U^*=14.7-16.7), another pattern was observed in which two pairs of vortices were shed from one side while only one pair was shed from the other side of the cylinder (2P+P). For U^*>16.7, a 2.5P+T pattern was observed in which two pairs and one single vortices were shed from one side and a triplet from the other side of the cylinder. This pattern was also observed in the reduced velocity range of U^*=18.7-20.7 at α=55º.

For α=50º, a 2P shedding was observed for U^*<10.7. This was followed by 2.5P+P in which two pairs and one single vortices were shed from one side and a pair of vortices

from the other side. This was followed by a shedding of two pairs and one single vortices from one side and two pairs of vortices from the other side (2.5P+2P). For the same angle of attack α=50º, at higher reduced velocities, the shedding pattern changed to 3P+2P in which three pairs of vortices were shed when the cylinder was moving up and two pairs when it was moving down.

For α=55º, 2P shedding was observed for U^*<6.7, followed by T+P and then 2.5P+T. Two symmetric and high frequency shedding patterns of 2P+2P and 2.5P+2.5P were observed at high reduced velocities when the cylinder was placed in a symmetric orientation with respect to the incoming flow direction (α=60º).

Overall, different flow-induced instabilities observed for triangular cylinder (galloping vs. VIV) at varying angles of attack and different reduced velocities were matched by different shedding patterns observed in the wake of the cylinder.

6.4 Conclusion

Flow-induced oscillation of a cylinder with a triangular cross-section was studied experimentally. The cylinder had one-degree-of-freedom to oscillate in the crossflow direction. The response of the cylinder in terms of the amplitudes of oscillations as well as the flow forces were studied at varying angles of attack in the range of α=0º-60º and a reduced velocity range of U^*=4-22.

Depending on the angle of attack and the reduced velocity, the cylinder experienced both VIV and galloping. For small angles of attack of α<30º, the cylinder did not oscillate while for larger angles of α=30º and 35º, the cylinder underwent large-amplitude

oscillations in a limited range of reduced velocities (U^*=7-14.5). The conducted dye flow visualization as well as the measured flow forces confirmed that the lock-in occurred in this range of reduced velocities and the triangular cylinder underwent VIV. At the same angles of attack and for larger reduced velocities (U^*=14.5-19.5), no oscillation was observed. The cylinder went back to large-amplitude oscillations again for these angles at higher reduced velocities (U^*=19.5-22), where the amplitude of oscillations increased with increasing reduced velocity. Several high harmonic shedding frequencies were observed in the flow force FFTs, which suggested a galloping-type response. Therefore, there was a range of angles of attack in which the cylinder experienced VIV at smaller reduced velocities and galloping at higher values. For angles of α=30º and 35º, in the intermediate range of reduced velocities between VIV and galloping (U^*=14.5-19.5) where no oscillation was observed, 2S vortex shedding was observed in which the shedding frequency matched the Strouhal frequency for a stationary triangular cylinder. For larger angles of attack of α>35º, the amplitude of oscillations increased monotonically and the cylinder underwent galloping. The amplitude of oscillations reached a maximum dimensionless value of A^*~3.7 at high reduced velocities for α=60º. The mean displacement of the cylinder increased at the angles of attack in which the cylinder was placed in an asymmetric orientation with respect to the incoming flow direction (α=20º-30º). Several different vortex shedding patterns were observed in the wake of the cylinder at different angles of attack and flow velocities. New, high-frequency shedding patterns were observed in the regions where galloping occurred.

The flow forces acting on the cylinder in both the crossflow and inline directions were measured. For the cases in which galloping was observed, higher harmonics were observed in the frequency contents of the lift and drag forces. The existence of higher harmonics were in agreement with the high-frequency vortex shedding patterns observed in the wake of the cylinder. Similar to the mean displacement of the cylinder, the mean value of the flow forces in the crossflow direction increased at higher reduced velocities for angles of attack of α=20º-30º.

CHAPTER 7

VORTEX INDUCED VIBRATIONS OF INCLINED FLEXIBLE CYLINDERS

7.1 Introduction

The majority of studies on Vortex-Induced Vibration (VIV) have investigated a flexibly-mounted rigid cylinder placed in flow with one degree of freedom in the crossflow direction (Bearman, 1984; Sarpkaya, 2004; Williamson and Govardhan, 2004). Later, studies by Jauvtis and Williamson (2004) and Parkinson and Smith (1964) showed that giving the structure a second degree of freedom in the inline direction can change the dynamic response of the system significantly. In many real world applications, such as mooring lines used to stabilize the existing offshore oil platforms and the conceptual designs for offshore wind turbines, VIV is observed in long flexible cylinders.

Early experimental studies by Vandiver (1993) and later by Chaplin et al. (2005b), Trim et al. (2005), Vandiver et al. (2006), Lie and Kaasen (2006) and Huera-Huarte and Bearman (2009a), as well as numerical studies of Bokaian and Geoola (1984) and Bourguet et al. (2011a) have shown that in a flexible cylinder, different higher structural modes can be excited in both the IL and CF directions.

Jhingran and Vandiver (2007), Modarres-Sadeghi et al. (2010) and Shi et al. (2012) have shown that higher harmonic forces do exist in the VIV response of flexible cylinders and that the existence of such high frequency flow forces can significantly affect the fatigue

life of the flexible cylinders. Modarres-Sadeghi et al. (2011) showed that chaotic response also exists in VIV of long flexible cylinders. For a flexible structure oscillating at a single frequency with its corresponding mode shape (mono-frequency excitation) or, in a more complex case, oscillating at multiple frequencies (multi-frequency excitation), the response measurements at a limited points along the length do not necessarily represent the behavior of the system precisely. Therefore, it has been of great interest to find a way to study the VIV response of flexible cylinders all along their length while only a limited number of measurements is available. Modal-analysis-based methods have been commonly used in studying the VIV response of long flexible structures (Chaplin et al., 2005b; Trim et al., 2005; Lie and Kaasen, 2006; Huera-Huarte and Bearman, 2009a). In this method, a continuous response along the length of the cylinder is reconstructed from limited measurement points that are almost evenly distributed along the length of the cylinder. If the number of measurement points satisfy the Nyquist-Shannon criterion ($m>2n+1$) (Mukundan et al., 2009), in which m is the necessary number of measurement points and n is the highest excited mode number, using the modal expansion theorem the response of the system can be reconstructed along the length .

While the continuous response reconstruction from limited number of sensors has been successfully achieved using modal expansion theorem, it should be noted that this method works fine when there exist enough sensors that are distributed evenly along the length of the cylinder. However, there are several cases where due to the experimental limitations or high cost of sensor installation and data transfer from sensors installed in deep seas, it is more desirable to reconstruct the response from the same limited number of

sensors that are localized in a region along the length of the cylinder. In the current study, a novel technique is introduced in which the previously used method based on modal expansion theorem is modified by Modal Assurance Criterion (MAC) to reconstruct the response of the system from limited localized measurement points.

While most VIV studies on flexible cylinders are conducted for high mass ratio systems ($m^*>1$), the ocean structures are mainly low mass ratio (Parkinson and Wawzonek, 1981; Huera-Huarte et al., 2014). The objective of this work is to study the VIV response of a low mass ratio flexible cylinder ($m^*<1$), which is totally submerged in uniform flow. In the present work, first we will discuss a series of small-scale VIV tests on a low mass ratio flexible cylinder placed in uniform flow and then we will use the experimental data in order to discuss a technique to reconstruct the VIV response of flexible cylinders from localized measurement points.

7.2 Experimental Set-up

The experiments were carried out in a re-circulating water tunnel, with a test section of 1.27 m×0.5 m×0.38 m and a turbulence intensity of less than 1% for up to a flow velocity of U=0.3 m/s. A uniform flexible circular cylinder with a diameter of D=0.6 cm, made from silicon rubber was tested. The cylinder was placed vertically in the test section of the water tunnel and a load cell was mounted at the top end of the cylinder to measure the tension along its length. An external tension of T=0.5 N was applied along the length of the cylinder. A streamlined end plate was used at the bottom boundary. Flow visualization was conducted in order to ensure that the leading edge of the end plate did not cause any separation (Jain and Modarres-Sadeghi, 2013). The immersed aspect ratio

(L/D) of the cylinder was 67, where L is the immersed length of the cylinder and D is the cylinder diameter. Only the top 6 cm of the cylinder (less than 10% of the total length) was out of water. The mass ratio of the cylinder was calculated to be m^*=0.43 ($m^* = 4m/\pi\rho D^2 L$, where m is the mass of the cylinder, L the cylinder length, D its diameter, and ρ the flow density). The elasticity modulus of the cylinder was obtained experimentally following the method discussed by Paidoussis (1998) as E = 2.4 MPa. The natural frequency of the cylinder can be found as (Obasaju et al., 1990)

$$f_n = \sqrt{\frac{Tn^2}{4ML^2} + \frac{EI\pi^2 n^2}{4ML^4}}, \tag{7.1}$$

where M is the mass of the cylinder plus the added mass ($M=m+m_a$) per unit length. By comparing the two terms in Eq. (7.1) for the parameters of the system considered here, it was found that the cylinder was tension-dominated (Calculated values for the first and second terms for the 1st mode were 8.9 and 0.12, respectively). The natural frequency of the first mode was measured experimentally in still water to be f_n = 2.83 Hz, and used to calculate the reduced velocity of the incoming flow as

$$U^* = \frac{U}{f_n D}, \tag{7.2}$$

where U is the flow velocity. In the experiments, the flow velocity was increased from 0.05 m/s to 0.25 m/s with increments of 0.0125 m/s and the cylinder response was recoded at each flow velocity. The cylinder was marked with uniformly-distributed black dots along its length. The cylinder oscillations were measured by capturing the motion of the cylinder in the streamwise (inline) and transverse (crossflow) directions using two synchronised high speed cameras (a Phantom Miro 110 and a Panasonic Lumix DMC-FZ200) at these

discrete points (Figure 7.1). The high speed cameras enabled recording videos with a high frame per second rate (up to 3000 fps). The captured videos were inputs to a tracking software (Tracker) which created synchronised displacement time histories in the inline and crossflow directions at these discrete points. The inline and crossflow displacements of the points $\left(\mathbf{x}(z,t),\mathbf{y}(z,t)\right)$ were functions of time, t, and position, z. Only the displacements of 10 points distributed along the length of the cylinder were tracked: one out of three from the total 30 points that were marked on the cylinder.

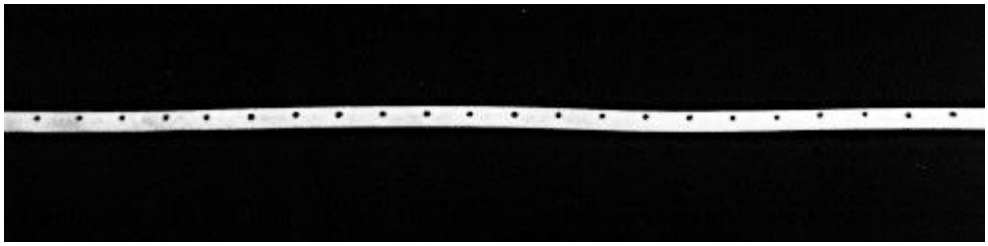

Figure 7.1. Discrete points marked on the flexible cylinder used to capture the cylinder's motion at discrete points by using a high speed camera.

7.3 Reconstructing a continuous response along the length of the cylinder

A method based on modal analysis was used to reconstruct the cylinder response continuously along its length using the displacement data at discrete points. Assuming sinusoidal mode shapes for the cylinder, its response can be expressed in matrix form as a linear combination of its mode shapes as

$$\mathbf{X}(z,t)=\mathbf{\Phi}(z)\mathbf{X}_M(t),\quad \mathbf{Y}(z,t)=\mathbf{\Phi}(z)\mathbf{Y}_M(t), \tag{7.3}$$

where, $\mathbf{X}(z,t)=\left[\mathbf{x}(z_1,t),\ \mathbf{x}(z_2,t),\ldots\right]$ and $\mathbf{Y}(z,t)=\left[\mathbf{y}(z_1,t),\ \mathbf{y}(z_2,t),\ldots\right]$ are the matrices of measured displacements in which the rows consist of the inline and crossflow

displacements measured at individual points along the cylinder; $\mathbf{\Phi}(z)=[\mathbf{\Phi}_1,\ \mathbf{\Phi}_2,\ \mathbf{\Phi}_3,\ldots]$ is the displacement modal shape matrix, in which each column consists of normalized sinusoidal mode shapes at different points along the cylinder at each mode number, *M*, normalized to be 1 at their maxima; $\mathbf{X}_M=[\mathbf{x}_{M1}(t),\mathbf{x}_{M2}(t),\mathbf{x}_{M3}(t),\ \ldots]$ and $\mathbf{Y}_M=[\mathbf{y}_{M1}(t),\mathbf{y}_{M2}(t),\mathbf{y}_{M3}(t),\ \ldots]$ are modal contribution matrices that each row consists of row vectors of time series of each mode's contribution to the overall response. In order to calculate the modal contribution matrices, $\mathbf{X}_M(t)$ and $\mathbf{Y}_M(t)$, the measured time histories are substituted in the $\mathbf{X}$ and $\mathbf{Y}$ matrices and by considering the number of modes used (*M*), the modal contribution matrices are obtained as

$$\mathbf{X}_M(t)=\mathbf{\Phi}^{-1}(z)\mathbf{X}(z,t),\quad \mathbf{Y}_M(t)=\mathbf{\Phi}^{-1}(z)\mathbf{Y}(z,t)\,. \tag{7.4}$$

Once each mode's contribution to the overall response is known at discrete points along the cylinder, modal expansion theorem can be applied to obtain the response of the system at any arbitrary point along the cylinder as

$$\mathbf{X}(z,t)=\mathbf{\Phi}(z)\mathbf{X}_M(t),\quad \mathbf{Y}(z,t)=\mathbf{\Phi}(z)\mathbf{Y}_M(t)\,, \tag{7.5}$$

in which, this time, the known parameters are the modal matrices $\mathbf{\Phi}(z)$ and modal contributions of each mode, $\mathbf{Y}_M(t)$ and $\mathbf{X}_M(t)$.

A major step in the reconstruction method is to choose the proper dominant structural modes that contribute in reconstructing the response of the system. In most previous studies using similar modal expansion theorem (Chaplin et al., 2005b; Trim et al., 2005; Huera-Huarte and Bearman, 2009a), all the structural modes, starting from the 1st

mode to a rather high mode, were used in the reconstruction process. In the present study, the selection of dominant structural modes is made based on the Modal Assurance Criterion (MAC) (Allemang, 2003; Pastor et al., 2012). As discussed later, this way of selecting the dominant modes will allow reconstructing the system response using localized measurement points. The MAC is a scalar constant relating the degree of consistency (linearity) between two vectors as:

$$MAC = \frac{\left|\{\boldsymbol{\psi}_A\}^T \{\boldsymbol{\psi}_x\}\right|^2}{\left|\{\boldsymbol{\psi}_A\}^T \{\boldsymbol{\psi}_A\}\right|\left|\{\boldsymbol{\psi}_x\}^T \{\boldsymbol{\psi}_x\}\right|}, \tag{7.6}$$

where, $\{\boldsymbol{\psi}_A\}$ and $\{\boldsymbol{\psi}_x\}$ are two vectors that are compared with each other. The MAC takes values between 0 to 1, where 0 corresponds to two independent vectors and 1 corresponds to identical vectors. Thus, if two vectors express a consistent, linear relationship, the MAC approaches unity. This method has been used previously in structural analysis to measure the linear correlation between experimental and theoretical mode shapes of flexible structures, from macro to nano scale (Helfrick et al., 2011; Cigeroglu and Samandari, 2014). In the current study, the MAC is used in order to decide on the mode shapes that contribute in the system response. Normalized instantaneous displacement of the cylinder is compared to the sinusoidal mode shapes of different modes and for M modes that are assumed to contribute to the response of the system, a vector of $1\times M$ of MAC numbers are calculated. The MAC numbers show the contribution of each structural mode shape in the total response and they are applied to Eq. (7.4) to adjust the reconstructed response:

$$\mathbf{X}_M(t) = \mathbf{M}[\boldsymbol{\Phi}(z)\mathbf{M}]^{-1}\mathbf{X}(z,t), \quad \mathbf{Y}_M(t) = \mathbf{M}[\boldsymbol{\Phi}(z)\mathbf{M}]^{-1}\mathbf{Y}(z,t), \tag{7.7}$$

where $\mathbf{M}$ is the MAC matrix, which is an $M \times M$ diagonal matrix of MAC numbers. Using the MAC matrix enhances the modal expansion method to automatically adjust contributions of the modes considered in the response reconstruction. Following this adjustment, the reconstruction method attenuates the modes that have small contributions and enhances the modes that contribute largely to the response reconstruction.

In Section 7.4, the reconstructed response of the cylinder using this method will be presented for the current experiment. Later in Section 7.6, it will be shown how this method of reconstructing the cylinder's response based on Modal Assurance Criterion can be used in reconstructing the VIV response from only a limited number of measurement points that are localized in a small region along the length of the cylinder.

7.4 Structural response of the system

In each test, videos of the cylinder's oscillations were captured at 120 fps. The first natural frequency of the cylinder in still water was measured experimentally to be 2.83 Hz. This natural frequency and the selected recording frame rate guaranteed that higher frequencies, up to at least the fifth mode, could be captured by the high speed videos. Also, as previously discussed by Mukundan et al. (2009), based on the Nyquist-Shannon criterion, the minimum number of measurement points (m) needed to capture the n^{th} structural mode (n) is $m=2n+1$. In the current study, 10 discrete points along the length were tracked and two boundaries were assumed to be fixed during the oscillations, which made it possible to capture the structural mode response up to the fifth mode. The flow

velocity was increased in small increments from U=0.05 m/s to U=0.25 m/s, which corresponded to a range of reduced flow velocities of U^*= 2.9 – 14.5 and Reynolds numbers of Re = 315 – 1580.

In the experiments, the first and the second modes were excited in the crossflow (CF) direction and up to the 4th structural mode in the inline (IL) direction. In what follows, the response of the cylinder at four different reduced velocities of U^*=3.6, U^*=6.5, U^*=8.7 and U^*=10.1 are discussed as sample cases of the typical behavior observed in the results. This is then followed by an overall view of the response over the entire range of reduced velocities tested.

7.4.1 Case 1: U^*=3.6 – mainly-first-mode excitation in the CF direction

Figure 7.2(a,b) shows the dimensionless RMS values of the cylinder displacement for both the inline and crossflow directions at a reduced velocity of U^*=3.6. The RMS values are normalized by the cylinder's diameter. The RMS values of the measured discrete experimental points are plotted on top of the reconstructed response to show that the reconstructed response matched the original experimental measurements very well. Frequency content of the structural response is plotted in Figure 7.2(c,d) for the inline (F_{IL}) and crossflow (F_{CF}) directions against the cylinder length, z, at a reduced velocity of U^*=3.6. The frequency of oscillations is normalized by fundamental natural frequency in still water. The amplitudes of oscillations along the length of the cylinder versus time for the same flow velocity in the IL and CF directions are depicted in Figure 7.2(e,f).

As shown in the frequency contents, while mainly a single frequency close to the first natural frequency of the cylinder was observed in the crossflow direction, several frequencies existed in the inline direction. In the CF direction, the structure oscillated at frequency close to its first natural frequency and its first structural mode shape was excited. However, in the inline direction, the structure oscillated at several frequencies (1^{st}, 2^{nd} and 3^{rd} harmonics) and the structural mode resembled the first structural mode shape (with no node along the length of the cylinder). In a tension-dominated beam, it is expected that when the second harmonic frequency is observed, the second structural mode shape gets excited. Gedikli and Dahl (2014) have observed similar phenomenon in VIV of flexible vertical cylinder in flow in which the ratio between the inline and the crossflow natural frequencies were kept constant at 2:1. The response consisted of the first mode excitation in the crossflow direction with an excitation of the second mode frequency in the inline direction, however, the structural mode shape was still the first mode in the inline direction. It was hypothesized that the variation of effective added mass was responsible for this situation.

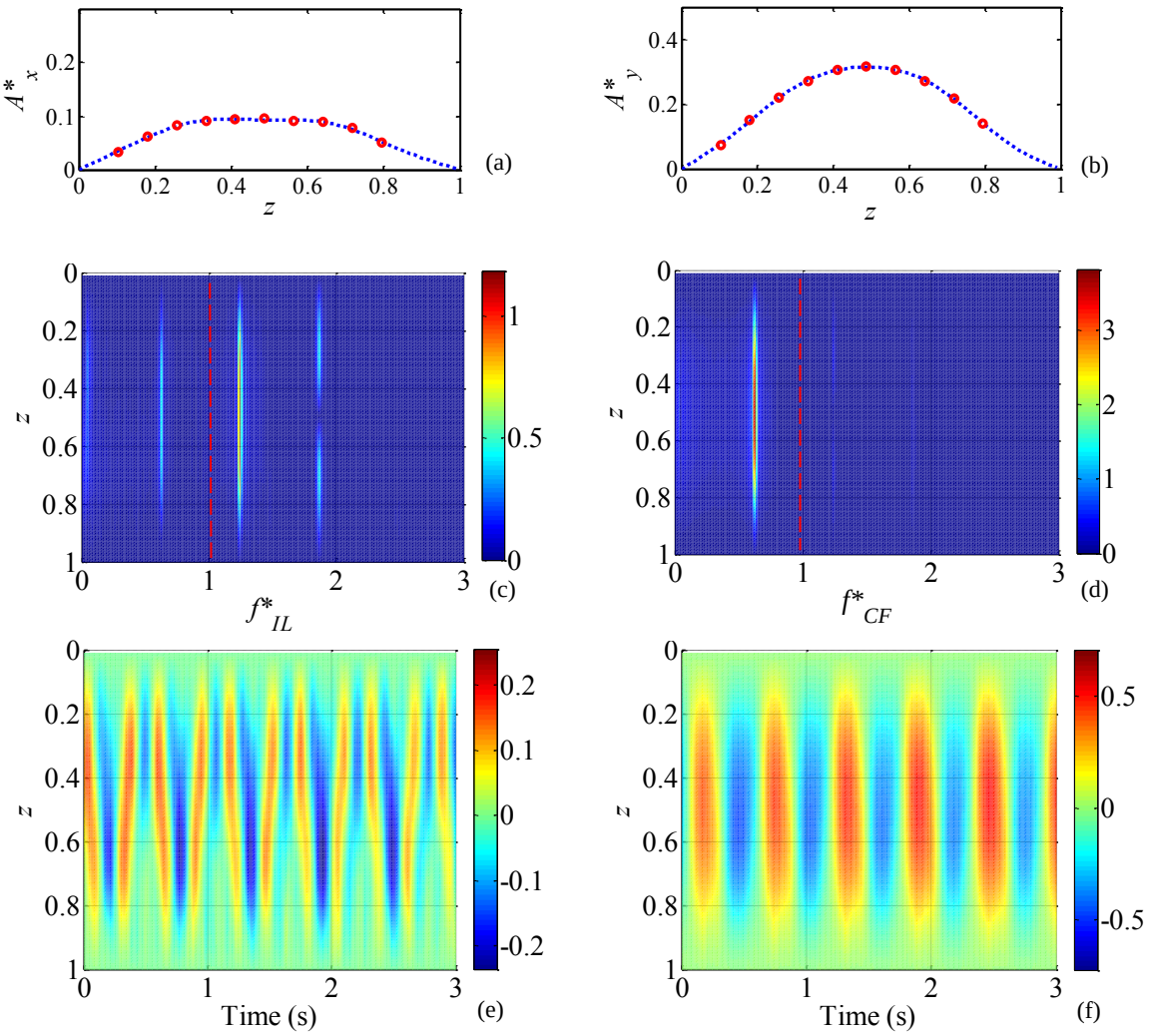

Figure 7.2. RMS values of the (a) inline and (b) crossflow displacement (dashed line: reconstructed response, circles: experimental measurement). Frequency contents of the (c) inline and (d) crossflow motion. Displacement time histories of the (e) inline and (f)

Overall at low reduced velocities, mono-frequency vortex-induced vibration was observed in the CF direction and multi-frequency oscillations in the IL direction.

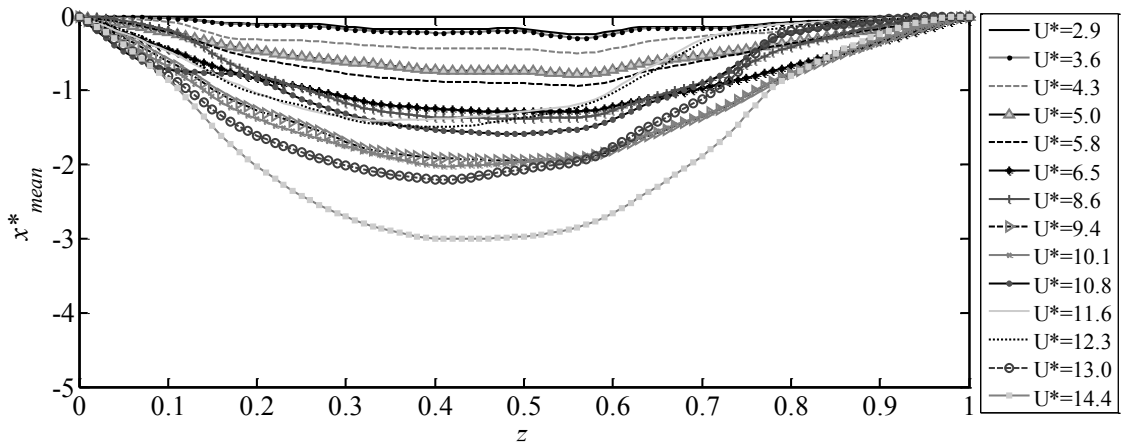

Figure 7.3. Spanwise mean deflection of the cylinder in the inline direction.

7.4.2 Case 2: U^*=6.5; mainly-first-mode excitation in the CF and second-mode in the IL direction

Figure 7.4 shows the same plot as Figure 7.3 but for U^*=6.5. In the crossflow direction, similar to the previous case, a frequency close to the first natural frequency of the system was observed. However, in the inline direction, a very small contribution of the first harmonic and a more significant contribution from the second harmonic were observed. At this reduced flow velocity the first structural mode in the CF direction and the 2nd structural mode in the IL direction were excited. Also, a small contribution of a frequency three times the fundamental frequency was observed, with the third structural mode. At high flow velocities as the amplitude of the inline oscillation increased, the contribution from the VIV response in the inline direction increased compared to the contribution from the mean deflection values. Therefore, the structure oscillated with the frequencies equal, twice and three times the fundamental frequency in the inline direction

where similar corresponding structural mode numbers were excited. In the crossflow direction the existence of the first structural mode at the fundamental frequency was observed.

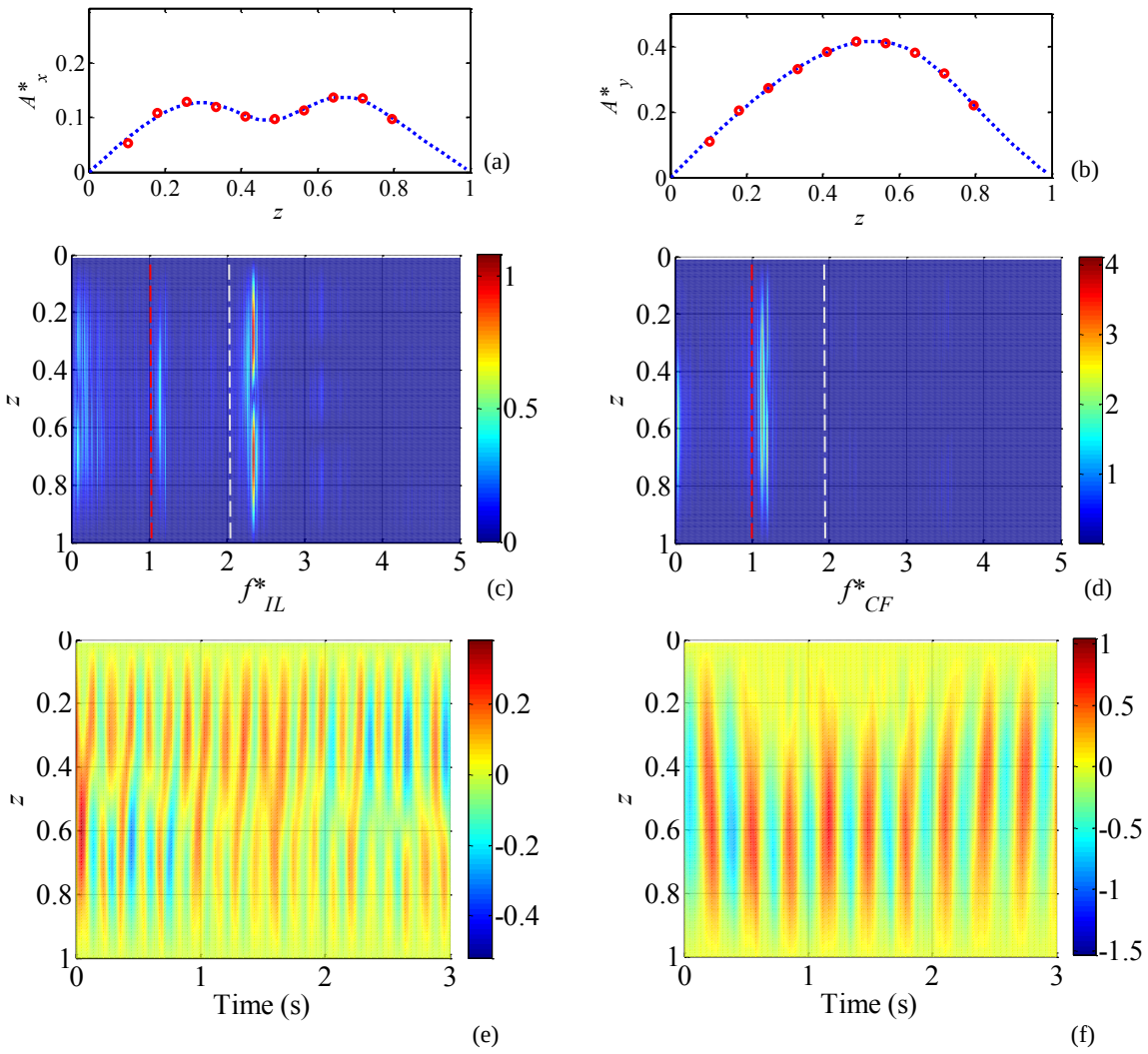

Figure 7.4. RMS values of the (a) inline and (b) crossflow displacement (dashed line: reconstructed response, circles: experimental measurement). Frequency contents of the (c) inline and (d) crossflow motion. Displacement time histories of the (e) inline and (f) crossflow motion at a reduced velocity of U^*=6.5.

7.4.3 Case 3: U^*=8.7- Transition to higher modes

The response of the system at a reduced velocity of U^*=8.7 is chosen as a representative response with a multi-modal excitation in which the response was in transition from lower modes to higher modes. Frequency content plots show that in the CF direction, contributions both from the first and the second modes were observed. The second mode frequency with the second structural mode shape started to develop at values slightly larger than the first natural frequency. In the inline direction, the cylinder was excited in its first, second and the third mode with their corresponding structural mode shapes. While the multi-frequency excitation is clear in the displacement time history of Figure 7.5(e), the transition from the first mode to the second mode in the crossflow direction is shown in time histories of Figure 7.5(f).

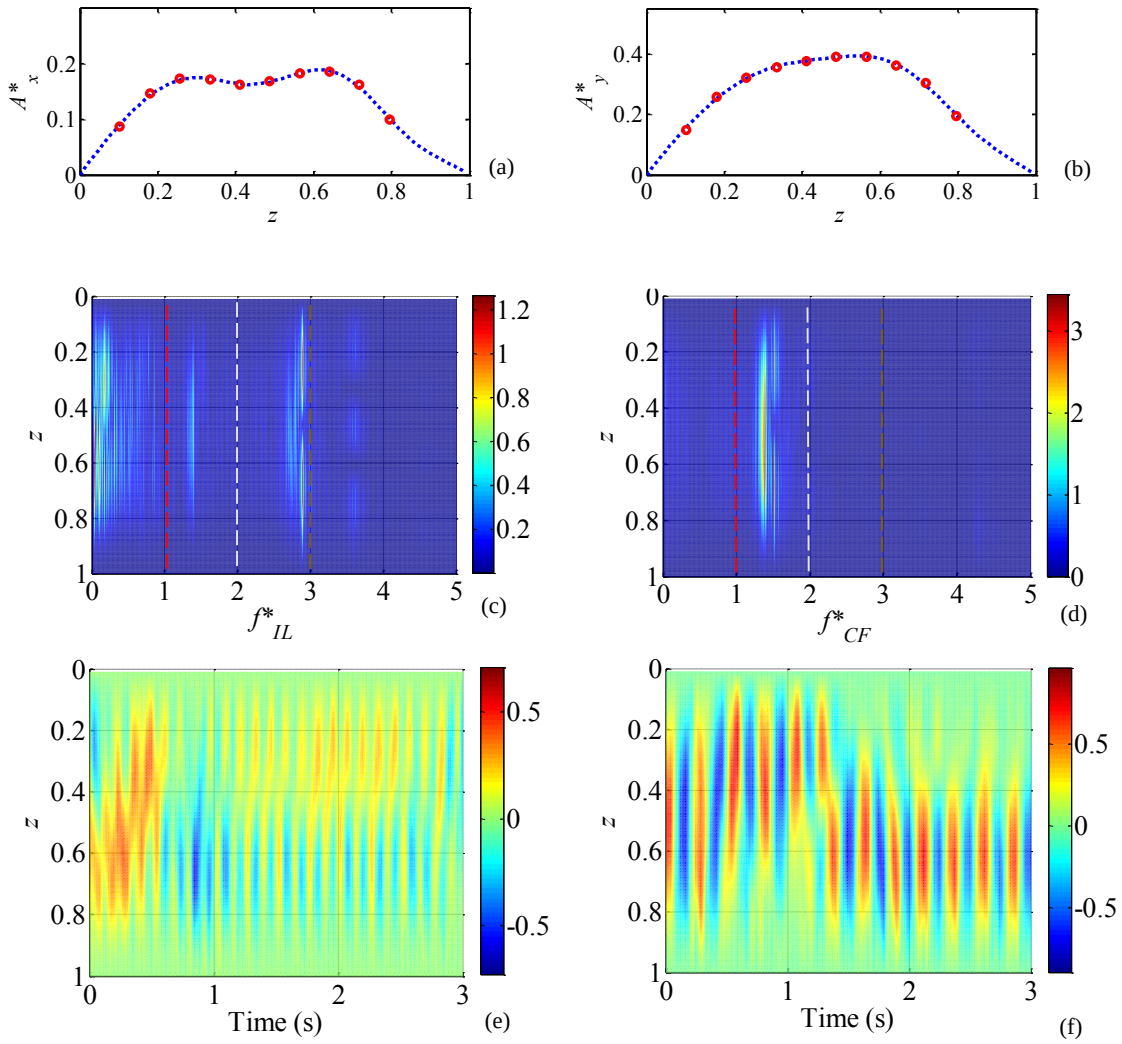

Figure 7.5. RMS values of the (a) inline and (b) crossflow displacement (dashed line: reconstructed response, circles: experimental measurement). Frequency contents of the (c) inline and (d) crossflow motion. Displacement time histories of the (e) inline and (f) crossflow motion at a reduced velocity of U^*=8.7.

7.4.4 Case 4: U^*=10.1 - Higher modes excitation

The last case studied here was chosen at a reduced velocity of U^*=10.1 in which the transition from the first mode to the second mode in the crossflow direction was completed. Figure 7.6(b) shows the existence of the second structural mode in the CF direction. Also, Figure 7.6(c,d) shows that the second harmonic in the crossflow direction

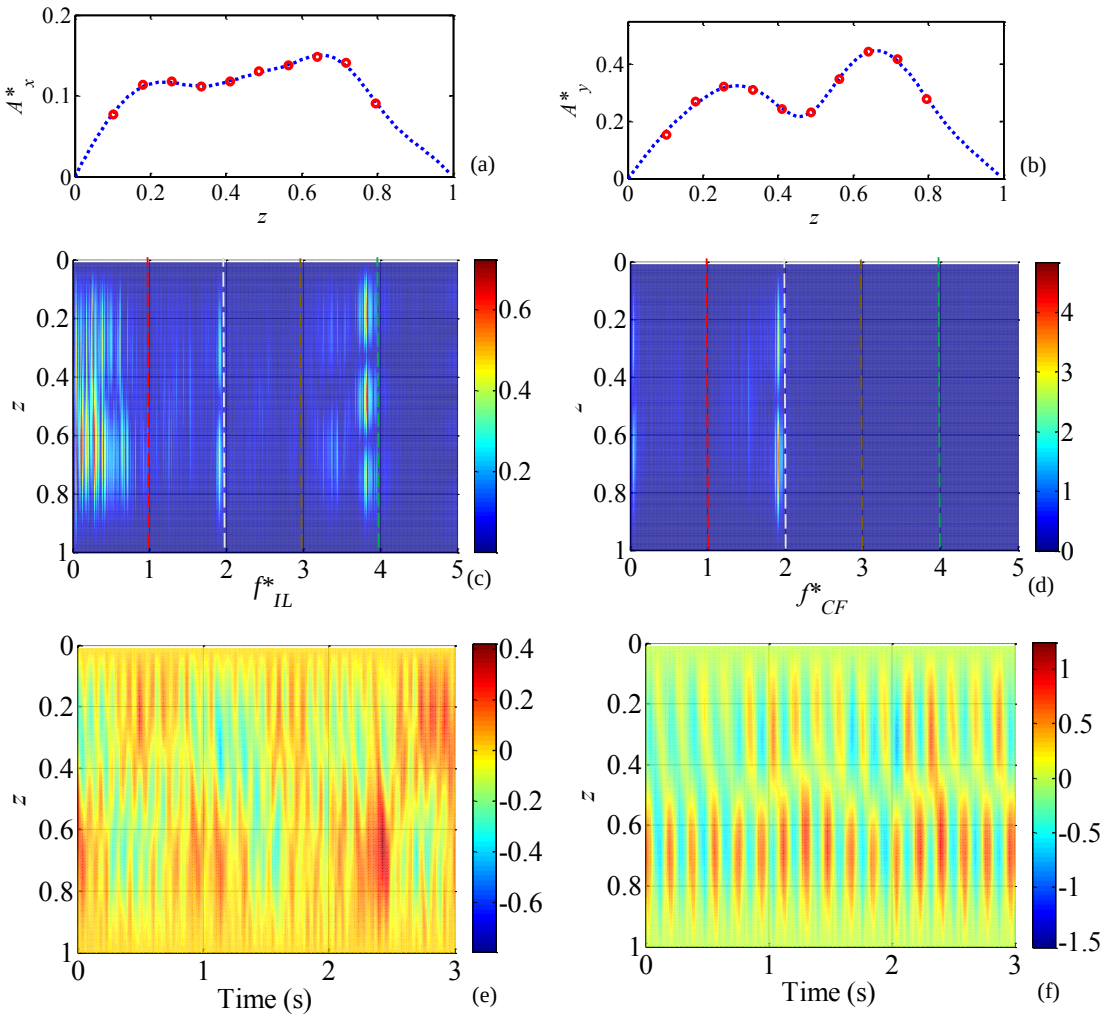

Figure 7.6. RMS values of the (a) inline and (b) crossflow displacement (dashed line: reconstructed response, circles: experimental measurement). Frequency contents of the (c) inline and (d) crossflow motion. Displacement time histories of the (e) inline and (f) crossflow motion at a reduced velocity of U^*=10.1.

together with the second structural mode shape. In the inline direction, the existence of the fourth modes was observed. It is also interesting to note that in the inline direction, while a fourth harmonic frequency was observed, the structural mode shape corresponding to this frequency stayed at the third structural mode. Also, the existence of travelling waves were

mostly noticeable at displacement time histories of this reduced velocities as shown in Figure 7.6 (e,f).

7.4.5 Response all over the lock-in range

The normalized RMS values of the modal weights for the first five modes at different reduced velocities are discussed in this section. These modal weights are the row vectors, $\mathbf{x}_M$ and $\mathbf{y}_M$ as introduced in Section 7.3. Figure 7.7 and Figure 7.8 show the sample representations of these row vectors for the reduced velocity of U^*=3.6. As shown previously in Section 7.4.1, the CF response at this velocity was dominated by the first structural mode, oscillating at its fundamental frequency. Similar behavior was shown by the modal weight representation here in which a large peak at the fundamental frequency was observed for the first structural mode (M=1) as shown in Figure 7.7. In the inline direction, both the first and second harmonics frequencies were observed, while the spatial mode shape corresponded to the first mode. Results for the inline direction are represented in Figure 7.8 in which the dominant peak at the frequency close to the fundamental and twice that are observed in the first structural modal weight, $\mathbf{x}_1(t)$.

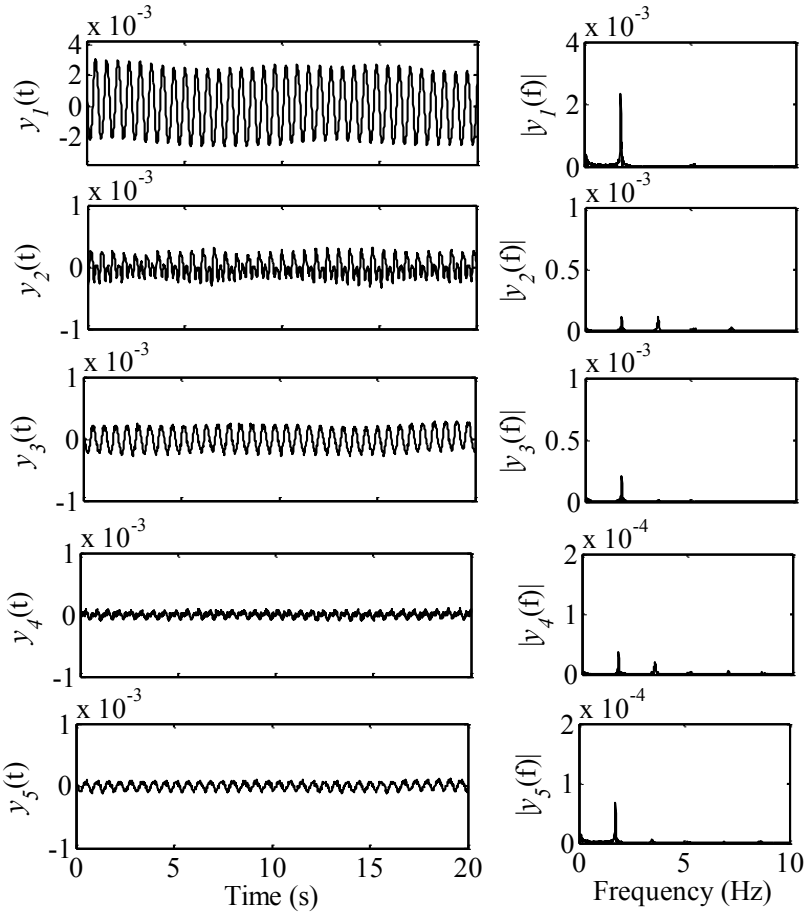

Figure 7.7. Time histories (left column) and FFT plots (right column) of the modal weights for the first five modes in the crossflow direction at a reduced velocity of U^*=3.6.

Figure 7.9(a) shows the normalized RMS values of the modal weights at varying reduced velocities for the CF direction. At low reduced velocities, oscillations started at the first mode with small amplitudes at a reduced velocity around U^*=3, reached a maximum value of $y^*_1 \approx 0.45$ and then decreased at higher velocities where the second mode contribution started to increase. In the low reduced velocity range where the first mode response was dominant, the normalized RMS values of the first mode weight resembled the bell-shaped amplitude of oscillations normally seen in the classical VIV of a rigid

uniform circular cylinder (Khalak and Williamson, 1999). For the range of reduced velocities studied here, higher modes such as the third, fourth and fifth mode did not contribute largely to the oscillations of the cylinder in the crossflow direction as the maximum magnitude for these modes did not exceed y^*~0.1. Similarly, in the inline direction (Figure 7.9(b)), while the first mode was dominant at a lower reduced velocities, the contribution of the second mode as well as higher modes (mainly the third and the fourth modes) increased at higher reduced velocities.

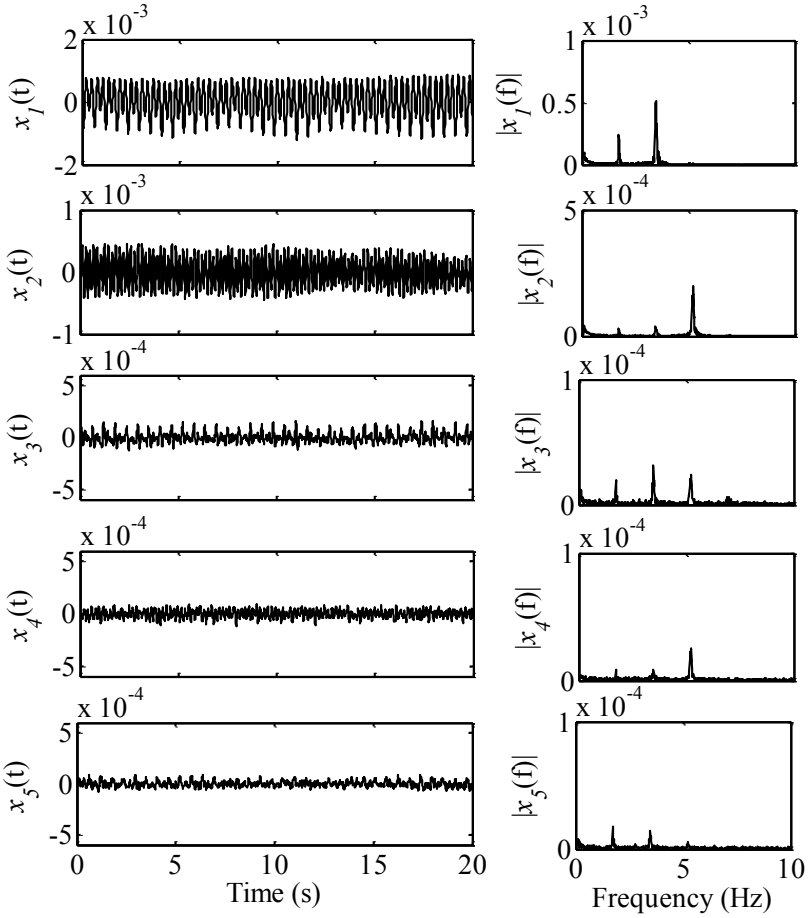

Figure 7.8. Time histories (left column) and FFT plots (right column) of the modal weights for the first five mode in the inline direction at reduced velocity of U*=3.6.

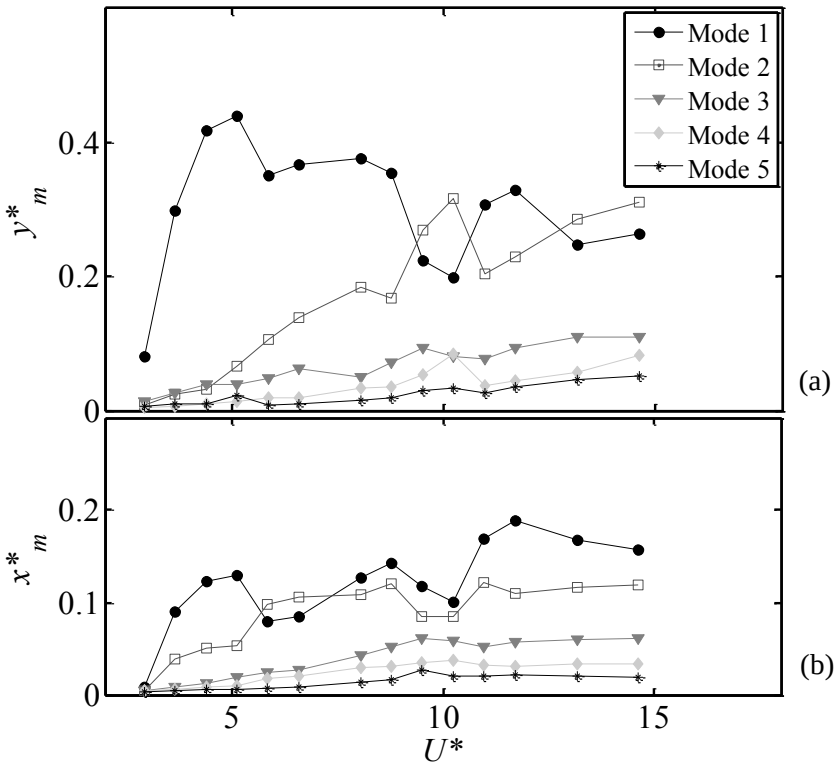

Figure 7.9. Modal contributions of the first five modes in the (a) crossflow and (b) inline direction.

7.5 Flow forces, phase differences and trajectories of motion

Flow forces acting along the length of the cylinder in the crossflow direction were calculated using the equation of motion of a continuous beam in tension:

$$m\ddot{y} - \left(Ty'\right)' + \left(EIy''\right)'' = f_y\left(z,t\right), \tag{7.8}$$

in which m is the mass per unit length of the cylinder, EI is the structural rigidity, T is the applied tension along the length and y is the measured displacement of the cylinder in the crossflow direction.

In order to find the regions that were excited by the flow, lift force coefficients in phase with the cylinder velocity (C_{Lv}) were calculated as

$$C_{Lv} = \frac{F_L \sin(\phi)}{1/2\, \rho L D U^2}, \tag{7.9}$$

where F_L is the lift force and φ is the phase difference between the lift force and the cylinder oscillations in the crossflow direction. Positive values of C_{Lv} represent the region where the energy is transferred from the flow to the cylinder and the structure is excited by the surrounding flow. Figure 7.10(a) shows the C_{Lv} values along the length of the cylinder for a sample reduced velocity of U^*=10.1. The lift coefficient in phase with velocity has positive values in the ranges of $0 \le z \le 0.22$, $0.41 \le z \le 0.51$ and $0.85 \le z \le 1$ suggesting that the flow forces contributed to the excitation of the cylinder at these regions at this reduced velocity.

Also, as it has been previously shown for a long flexible cylinder in shear flow (Bourguet et al., 2011a), the excitation regions where $C_{Lv} > 0$ coincide with the regions where the phase difference between the IL and CF displacements are in the range of φ_{xy}=[0 π], which corresponds to counterclockwise figure-eight trajectories. Counterclockwise figure-eight is defined based on the direction of motion in the upper half of the figure-eight path when the crossflow is from left to right (Dahl et al., 2007). Based on this definition, when the direction of cylinder's motion at the most extreme positions of the CF direction is opposite the flow direction, the orbital motion is called counterclockwise (CCW) and when the direction of cylinder's motion at the most extreme positions of the CF direction is the same as the flow direction, it is called clockwise (CW).

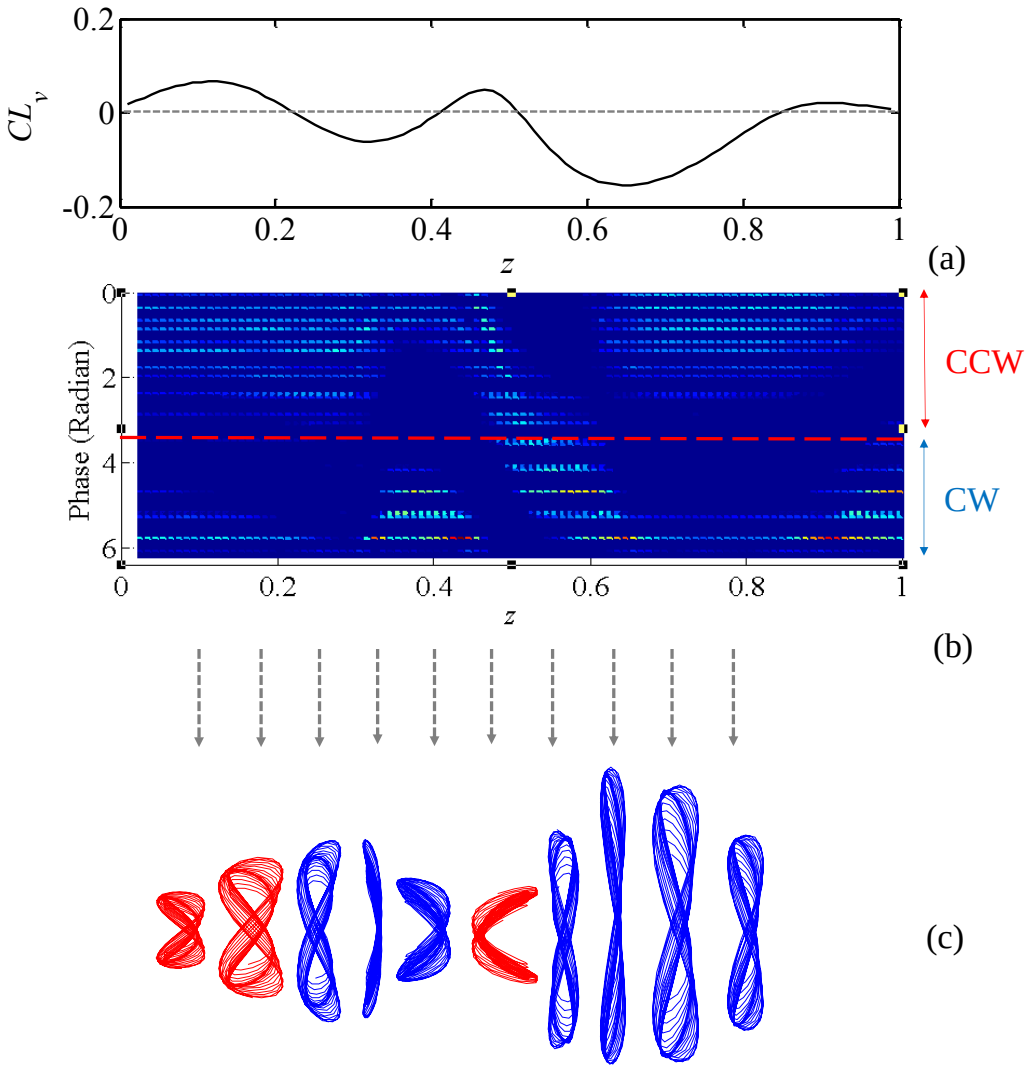

Figure 7.10. (a) Lift force in phase with velocity, C_{Lv}, (b) phase difference between the inline and crossflow displacements and (c) trajectories of motion at a reduced velocity of U^*=10.1.

To investigate the relation between the direction of the trajectories (CCW vs. CW) and flow forces (positive vs. negative C_{LV}) for the vertical cylinder in uniform flow, the phase difference has been plotted along the length of the cylinder for sample flow velocity of U^*=10.1 in Figure 7.10(b). The phase difference between the CF and the IL displacement has been obtained based on the instantaneous phase of the IL and CF

responses (Huera-Huarte and Bearman, 2009a). Also along with the phase differences, the trajectories are plotted at the measurement points in Figure 7.10(c) where counterclockwise trajectories are shown in red and clockwise ones in blue. Based on the results shown in Figure 7.10, it can be concluded that the regions along the length of the cylinder that were excited by the flow ($C_{Lv}>0$) experienced a counterclockwise figure-eight trajectory (φ_{xy}=[0 π]). This is in agreement with what has been seen for flexible cylinders in sheared flow (Bourguet et al., 2011b).

7.6 Using Modal Assurance Criterion (MAC) for Limited Number of Measurements

As seen in Section 7.4, continuous response of the system along the length of the cylinder was reconstructed from measurements at limited discrete points on the cylinder (10 points on the cylinder and 2 fixed points at the two boundaries). As previously discussed in Section 7.3, Modal Assurance Criterion (MAC) in connection with modal expansion theorem has been used in the response reconstruction at different reduced velocities. In this section, the use of MAC in reconstruction of the data is discussed, for cases that uniformly-distributed and relatively-dense measurement points are not available. This is often the case in practical applications, when as an example, measurements are possible only within a limited range of a flexible riser placed in the ocean and it is desired to reconstruct the complete response along the length of the riser based on those limited measurement points.

Figure 7.11(a) shows sample normalized RMS values of the cylinder's oscillations in the CF direction for a sample case with a reduced velocity of U^*=5. This is the response that has been reconstructed following the MAC method, this time using more measurement

point: 30 points distributed evenly along the length of the cylinder. This response is compared to the one that has been reconstructed using only 10 discrete measurement points. As it is shown, the reconstructed response from just 10 data points matches very well with the one with more measurement points, which closely represents the actual response of the system. Also, the response of the system using the same 10 measurement points has been obtained and plotted without making use of MAC and by considering the even contribution from the first five modes in the response reconstruction. The reconstructed response also matched very well with the actual response. Diagonal elements of the MAC number matrix, **M,** (Eq.(7.7)) associated with these three response reconstruction methods are given in Table 7.1. The MAC numbers for all three responses show very large values (in the scale of 0-1) for the first mode, meaning that it was mainly the first structural mode that contributed to the oscillations of the cylinder at this velocity. The diagonal elements of the MAC matrix, **M,** were very close to each other in these three different reconstructed responses. This example shows that if the measurement points are evenly distributed and cover the entire length of the cylinder, the reconstruction is easily possible only if the Nyquist-Shannon criterion ($m>2n+1$) is satisfied.

Table 7.1. Diagonal elements of the MAC matrix, **M**, at $U^*=5.0$

	Diagonal elements of MAC number Matrix	
	Evenly distributed	localized
Exact	$(0.99, 0.03, 0.02, 0.0, 0.0)$	---
MAC	$(0.99, 0.06, 0.04, 0.0, 0.0)$	$(0.99, 0.85, 0.0, 0.61, 0.37)$
No MAC	$(1,1,1,1,1)$	$(1,1,1,1,1)$

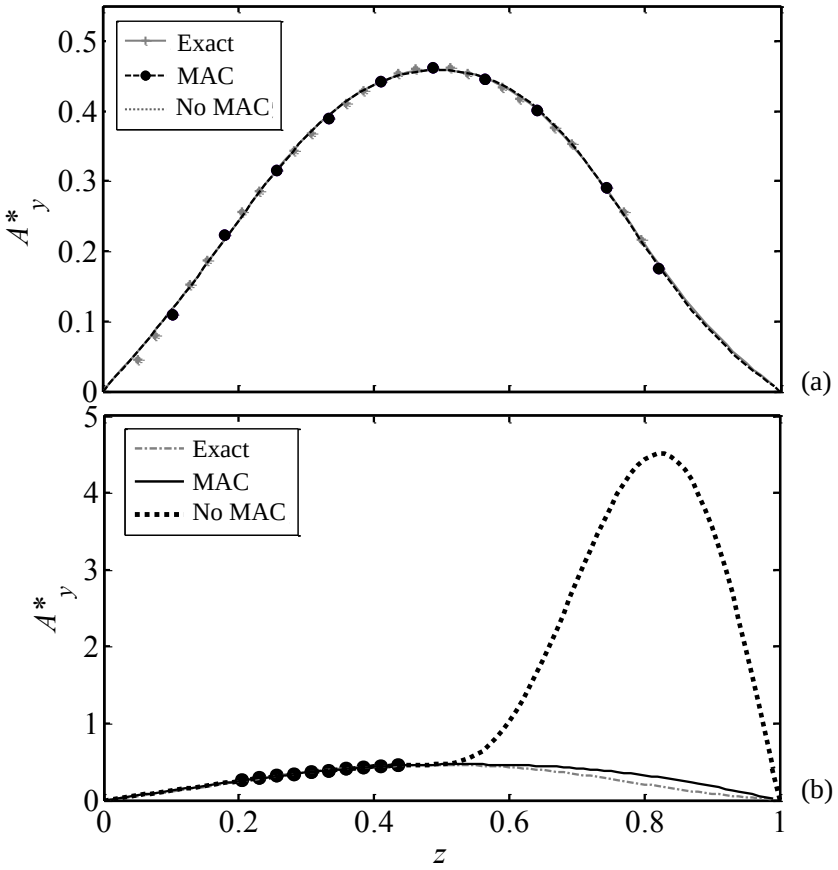

Figure 7.11. Sample response reconstructions in the crossflow direction at a reduced velocity of U^*=5.0: (a) evenly distributed measurement points and (b) locally distributed measurement points.

Sometimes, depending on the limitation of the experimental set-up or high cost of sensors and instrumentations needed to cover the entire length of the cylinder, measurements are conducted only locally. For example, consider the case in Figure 7.11(b), where the necessary number of measurement points to satisfy the Nyquist-Shannon criterion are chosen (10 points), but instead of even distribution of these points all along the cylinder, they are clustered in one region z=[0.2-0.4]. The challenge would be to reconstruct a continuous response of the riser using these limited data points.

The dashed line in Figure 7.11(b) shows the reconstructed response from these limited data points when only the modal expansion theorem has been used without implementing the MAC method. The actual reconstructed response from 30 measurement points is also plotted (dashed-dotted line). It is clear that using the modal expansion theorem failed in reconstructing the response properly, and there was a large overshoot between the reconstructed response and the actual one in regions where no measurement was available. Using the MAC method, however, made it possible to reconstruct the response accurately even for the regions where there was no measurement data point (continuous line). This can be explained by looking at the diagonal elements of MAC number matrix, **M**, for these three reconstructed responses in Table 7.1. The MAC numbers for the clustered measurement points still show the first mode is the dominant contributing mode. Applying each mode's contribution in the form of matrix **M** in Eq. (7.7) automatically adjusted the modal weight vector, $\mathbf{Y}_M(t)$, and mode shape matrix $\mathbf{\Phi}(z)$ to reconstruct the response more precisely. When using modal expansion theorem only (Eq. (7.4)), it is assumed that each mode contributes evenly in the response reconstruction and all of the diagonal elements of the MAC number matrix take the value of 1.

It should be noted that the measurement points cannot be clustered at any arbitrary regions for the MAC method to reconstruct the response. An estimate of the structural mode that will be excited is necessary. This is not a limitation for the method, because an estimate of the excited modes is necessary even when deciding on the number of sensors, in order to satisfy the Nyquist-Shannon criterion. Depending on the estimated excited mode, the cluster of sensors/measurement points should be localized in the range where

the estimated excited mode has the least correlation with its neighboring modes. By doing so, the MAC method could differentiate between one mode shape and its neighboring modes and allocate each mode its corresponding MAC number correctly. For example, Figure 7.12 shows the first five structural modes of a tensioned beam fixed at both ends, assuming these sinusoidal structural modes contribute to the response of the system. The bar plot of Figure 7.12 shows the correlation between these five modes at five different regions along the length of the cylinder. For example, cluster of measurement points in the first region z=[0 0.2], should be avoided as in this region almost every mode has a large correlation with other modes. This correlation should be expected when looking at the mode shapes at that region. In the range of z=[0 0.2] almost all five modes follow the same pattern and have relatively close curvatures, resulting in high correlation between these modes. However, region z=[0.2 0.4] is a suitable region for placing the sensors. As the bar plot shows, there is a relatively large correlation between the first and the second modes in the range of z=[0.2 0.4] but the correlations are much smaller for the other modes. As shown in Figure 7.11(b), reconstruction using data points from this region led to an accurate response. Overall, a rough estimation of the proper locations of the data points is needed for the MAC method to improve the reconstruction accuracy.

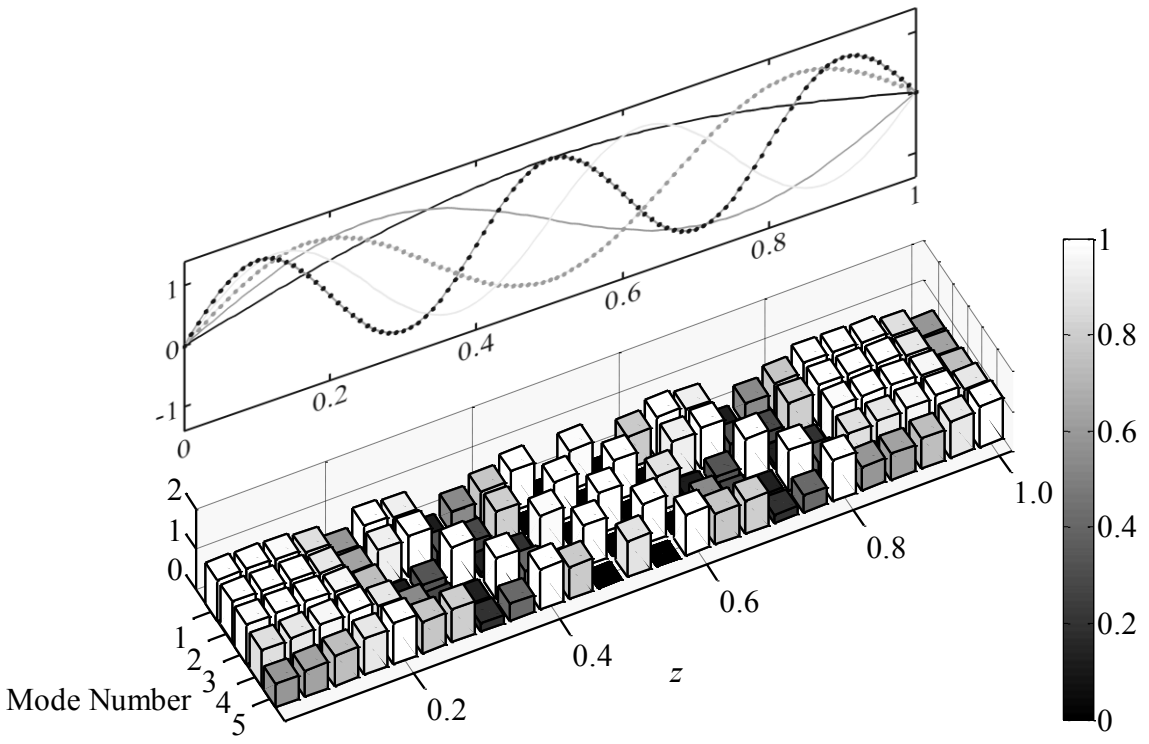

Figure 7.12. Correlation between the first five modes based on sinusoidal mode shapes.

7.7 Inclined flexible cylinder

As previously mentioned, the majority of the studies on VIV have investigated the flexibly mounted rigid cylinder or a flexible cylinder placed in flow such that the flow direction is perpendicular to the long axis of the cylinder – see reviews of Bearman (1984), Williamson and Govardhan (2004) and Sarpkaya (2004). However, in many real world applications of vortex-induced vibrations, such as mooring lines used to stabilize the existing off-shore oil platforms and the conceptual designs for offshore wind turbines, the cables used for towing submerged devices, and many other examples, the cylinder is not necessarily placed perpendicular to the oncoming flow direction. However, in several studies it has been assumed that the axial component of the flow has a negligible impact

on the dynamic response of the system (Jhingran and Vandiver, 2007) and the inclined cylinders can be treated as normal-incidence ones, if only the normal component of the free stream velocity is considered (known as Independence Principle). Studies for rigid inclined cylinder have shown, this hypothesis is applicable for small angles of inclinations but the impact of the axial component becomes dominant as the angle of inclination increases. Studies conducted by Surry and Surry (1967), Ramberg (1983) and Zhao et al. (2009) on a fixed rigid inclined cylinder suggest that an inclined cylinder behaves similarly to a normal-incidence one up to a maximum inclination of around 40°–50°. For the case of a flexibly mounted rigid cylinder, studies have shown that the amplitude of the vibrations, drag and lift coefficients and also the lock-in range are closely dependent on the degree of inclination (Vanatta, 1968; Lucor and Karniadakis, 2003; Franzini et al., 2009; Franzini et al., 2013; Jain and Modarres-Sadeghi, 2013). However, many engineering applications deal with flexible cylinders which have received far less attention. Although there are number of studies on vortex induced vibrations of a flexible cylinder placed normal to the flow (Vandiver, 1993; Chaplin et al., 2005b; Huera-Huarte and Bearman, 2009a; Modarres-Sadeghi et al., 2010; Bourguet et al., 2011b), there are very limited numerical studies on an inclined flexible cylinder placed in flow in which the validity of IP has been investigated (Bourguet et al., 2014; Bourguet and Triantafyllou, 2015). In this part of our research, we experimentally study the vortex-induced oscillations of an inclined flexible cylinder in range of Reynolds numbers from 160 to 4000. Here, based on the dynamic response of the system, we investigate the degree to which the Independence Principle (IP) is valid.

The experimental setup used for inclined cylinder experiments is exactly similar to the previously discussed vertical flexible cylinder (Section 7.2). The cylinder was fixed at both ends and placed at different inclinations in the test section (Figure 7.13). The natural frequency of the first mode of the system at each applied tension was measured in water, and was used to calculate the normal reduced velocity of the oncoming flow as

$$U_n^* = \frac{U\cos(\theta)}{f_n D} \tag{7.10}$$

where, f_n is the natural frequency obtained in water and θ is the angle between the cylinder and vertical line (Figure 7.13). The end conditions of the cylinder were clamped at both ends and the streamlined end plate was used at the bottom boundary to reduce the end effects.

7.7.1 Independence Principle (IP)

The system response in the crossflow and inline direction was measured for different inclinations of 30°, 45° and 70°. For each run, at a specific angle of inclination and a specific tension, the flow rate was increased from zero in small steps. The overall 60 s of the response was recorded using the high speed camera. The amplitude and frequency of the cylinder oscillations were obtained using the reconstruction method discussed previously in Section 7.3.

Having the response of the system at different reduced velocities at varying angles from 0º to 70º, the validity of IP can be investigated based on the amplitude of oscillations. Figure 7.14 shows the RMS values of the modal weights at first three modes for each inclination at different normal reduced velocities in the crossflow directions. For the sake

of comparison, the results of the vertical flexible cylinder discussed earlier is also plotted in Figure 7.14. As it is shown from Figure 7.14 (a), at low normal reduced velocity around U^*_n~3 the first mode amplitude started from almost zero values for all the inclinations, got to a maximum value of y^*_1~0. 5 and the amplitude decreased at higher velocities. Second mode contributions shown in Figure 7.14 (b) started to increase from zero values at lower velocities to higher values of y^*_2~0.5 at high reduced velocities. For all cases, the maximum RMS values of the first modal weights were almost the same at around y^*_1~0. 5 while the lock-in width for the first mode was much smaller for the 70° inclination. Also, while the first mode contribution diminished for the θ=70º case at lower values of the normal velocities, the second mode contribution started earlier at smaller values of normal reduced velocities compared to the other inclinations. The lock-in width for the first mode contribution was about $3<U_n^*<8$ for 70º inclination while for angles of inclination less than 70º the lock-in started at almost the same normal reduced velocity of U_n^*~3 but ended at higher velocities. For 70º inclination, the second mode contribution got to the maximum value also at lower velocities compared to the other inclinations. Based on the modal weights in the crossflow direction the independence principle for inclined cylinders can be validated; i.e. the narrower lock-in width for the first mode contribution for 70º inclination suggests that this case can not be treated as a vertical cylinder by just taking into account the normal component of the velocity, but the axial component resulting from inclination of the cylinder is playing an important role in the overall VIV response of the system.

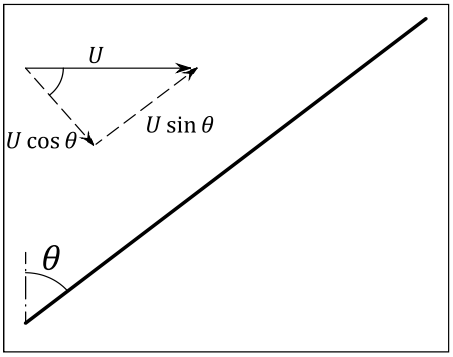

Figure 7.13. A schematic of the experimental setup.

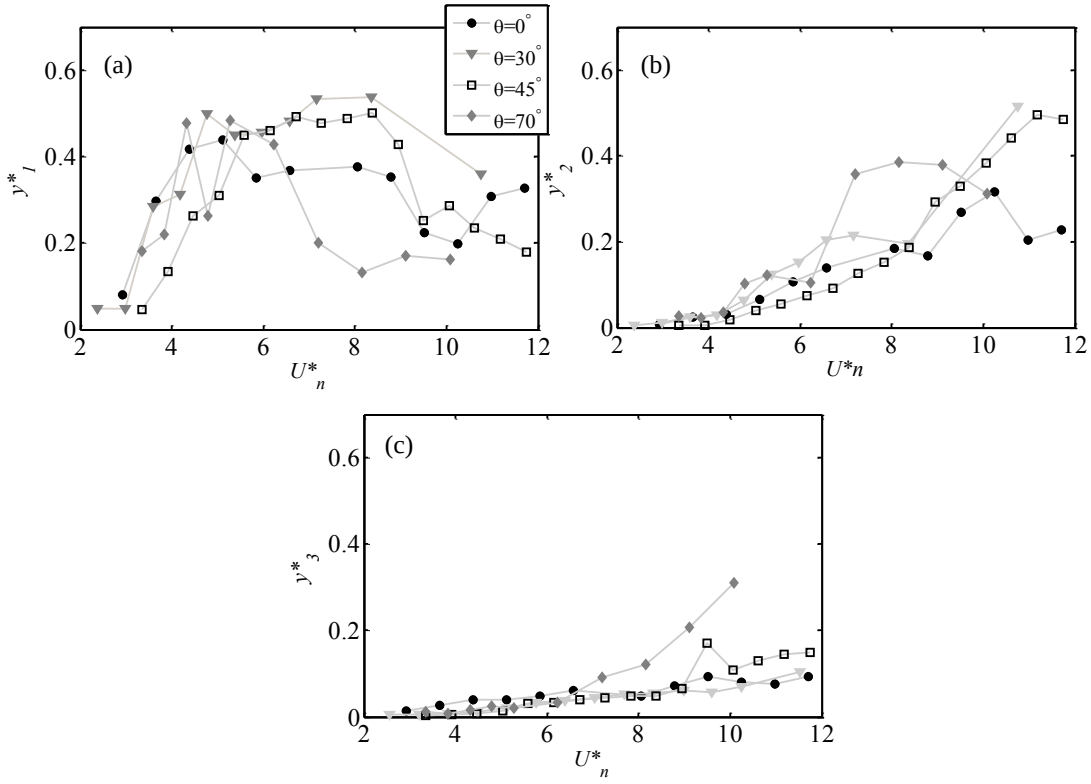

Figure 7.14 RMS values of the modal weights at crossflow direction for the first three modes (a) first mode, (b) second mode, (c) third mode

7.8 Conclusion

A series of experiments were conducted to study vortex-induced vibration of a as inclined flexible cylinder placed in uniform flow. First, to have a base of comparison a series of experiments were conducted to investigate the VIV of a vertical cylinder. The flow velocity was changed in the range of U=0.05-0.25 m/s which corresponded to a range of reduced flow velocities of U^*= 2.9 – 14.5 and Reynolds numbers of Re = 315 – 1580. The oscillations of a number of points along the length of the cylinder were tracked using two synchronized high speed cameras in the inline and crossflow directions. These data points were used to reconstruct a continuous response of the cylinder using on a novel technique based on the modal analysis method implementing Modal Assurance Criterion (MAC). This technique made it possible to reconstruct the response using only a limited localized measurement points.

Mono- and multi-frequency excitations as well as transition from lower modes to higher modes were observed in these experiments. Flow forces acting on the cylinder were calculated and the regions along the length of the cylinder that were excited by the flow (positive flow force coefficient in phase with velocity, i.e., positive C_{LV}) were identified. Counterclockwise figure-eight trajectories were observed in the regions with positive C_{LV}.

The reconstruction technique introduced here made it possible to properly reconstruct a continuous response along the length of the cylinder, even when the measurement points were localized in a small region of the cylinder. The MAC used in the reconstruction method adjusted each mode's contribution by comparing the linear correlation between the instantaneous displacement of the cylinder and the sinusoidal mode

shapes and automatically took into account each mode's contribution in the response reconstruction. Without using the MAC method, the modal expansion theorem, which is usually used in the literature to reconstruct the response, failed to properly reconstruct the response with localized measurement points. This advantage of the reconstruction method discussed here is of significance for practical applications in offshore industry, where limited localized sensors are usually used for VIV measurements due to the high installation and maintenance cost.

Finally, vortex induced vibrations of an inclined flexible cylinder placed in flow was investigated, experimentally. Different angles of inclination in a Reynolds number range of 160 to 4000 were tested and the validity of using the independence principle was studied. Considering the amplitude of oscillations in the transverse direction and for the 1^{st} mode of oscillations, it was observed that for angles of inclination up to 45°, the system behaved similarly to a normal-incidence case, if only the normal flow component was considered and the axial flow component had negligible effect on the system response. However, at 70°, if only the normal component of the oncoming flow was considered, the width of the lock-in region at 70° was smaller than the other inclinations. On this basis, the axial flow component affected the system response, and the Independence Principle was not valid.

CHAPTER 8

CONCLUSIONS AND FUTURE WORK

8.1 Overview

Vortex-Induced Vibration (VIV) of a circular cylinder placed in flow is a conical problem in fluid-structure interactions, both due to the fundamental questions associated with it and the wide range of industrial applications. The literature on VIV of a circular cylinder placed in flow is quite rich, both for a flexibly-mounted rigid cylinder (Bearman 1984; Sarpkaya 2004; Williamson & Govardhan 2004; Vandiver 2012) and a flexible cylinder (Vandiver 1993; Wu et al. 2012; Bourguet et al. 2012; Modarres-Sadeghi et al. 2011).

Typically, the majority of VIV studies have focused on symmetric systems in which the structure, its geometry, its boundary conditions and the incoming flow are symmetric. However, in many real-world applications of vortex-induced vibrations, such as mooring lines used to stabilize the existing off-shore oil platforms, towing cables, drilling risers and many other examples, the symmetry of the system is broken.

The main objective of this thesis was to study VIV of systems with broken symmetry and investigate how asymmetry introduced into the system can change the dynamic response of the system. To this end, among many examples of systems with

broken symmetry, some cases that are widely observed have been studied in the present thesis. The case of an inclined cylinder in which the cylinder is placed with an angle with respect to the incoming flow direction, or a tapered cylinder in which the diameter of the circular cylinder varies along its length, a circular cylinder which is forced to rotate about its long axis, or the case when the geometry of the cross-section changes from circular to another shape such as triangle have been studied in this thesis.

The following section outlines the most important contributions of this thesis from each chapter.

8.2 Conclusions

In Chapter 3 of this thesis, vortex-induced vibration of tapered cylinders free to oscillate in the crossflow direction was studied and the influence of the taper ratio on the VIV response of the system was investigated. Based on the experimental observations, it was concluded that

- The maximum amplitude of the crossflow oscillations stayed almost constant, for all taper ratios tested, at a value close to the maximum amplitude of a uniform cylinder with the same mass ratio.
- As the taper ratio was decreased (larger deviations from a uniform cylinder), the lock-in range started at larger reduced velocities and lasted up to higher reduced velocities.

- Tests were conducted for cylinders placed vertically in the test-section of the water tunnel, both with their diameter increasing downward and upward to show that the results were independent from the cylinder's orientation
- Hybrid shedding modes (both 2S and 2P shedding over the cylinder's length) were observed for all the linearly tapered cases for reduced velocities up to the value corresponding to the peak amplitude of oscillations. For reduced velocities higher than the peak amplitude, only 2P shedding was observed along the length.
- The splitting point which is the point at which the 2S and 2P vortex columns collided, changed its position along the length of the cylinder at different flow velocities, starting from smaller diameters at lower reduced velocities to larger diameters at higher reduced velocities.

In Chapter 4, VIV of a curved circular cylinder free to oscillate in the crossflow direction was studied experimentally. The influence of higher harmonic components of the flow forces on the response of the curved cylinder was studied in two configurations of the cylinder with respect to the oncoming flow direction: concave and convex. It was concluded that

- The amplitude of oscillations in both configurations decreased compared to a vertical cylinder with the same mass ratio
- Flow visualizations showed that the vortices were shed in parallel to the curved cylinder, when the cylinder was free to oscillate.

- Higher harmonic force components at frequencies twice and three times the frequency of oscillations were observed in flow forces acting on the vertical cylinder, as well as the curved cylinder.
- Asymmetry in the wake was responsible for the 2nd harmonic force component and the relative velocity of the structure with respect to the oncoming flow was responsible for the 3rd harmonic force component.
- The lock-in occurred over the same range of reduced velocities for the curved cylinder in the convex orientation as for a vertical cylinder, but it was extended to higher reduced velocities for a curved cylinder in the concave orientation. Higher harmonic force components were found to be responsible for the extended lock-in range in the concave orientation. Within this range, the higher harmonic forces were even larger than the first harmonic force and the structure was being excited mainly by these higher harmonic forces.

In Chapter 5 of this thesis, VIV of a flexibly-mounted circular cylinder free to oscillate in the crossflow direction with imposed rotation around its long axis was studied experimentally. The influence of different rotation rates on the response of the system was studied in terms of the amplitude and frequency of oscillations as well as the flow forces acting on the cylinder. Based on the experimental observations, it was concluded that

- The maximum amplitude of oscillations was limited to values less than a diameter of the cylinder at high rotation rates.
- The lock-in range became narrower at higher rotation rates and finally the oscillations ceased beyond a critical value of $\alpha=2.4$.

- Vortex shedding pattern was found to be 2S (two single vortices shed per cycle of oscillations) for rotation rates up to α=1.4 and transitioned toward an asymmetric P shedding (one pair of vortices shed in a cycle of oscillations) for rotation rates within the range of $1.4 \leq \alpha \leq 1.8$.
- When the rotating cylinder was free to oscillate in the crossflow direction, vortex shedding was found to persist up to higher rotation rates than those observed for a non-oscillating cylinder.
- The phase difference between the flow forces and displacement of the cylinder in the crossflow direction was influenced as the rotation rate was increased: At high reduced velocities, the phase difference decreased from 180° for a non-rotating cylinder to values close to 90° for a rotating cylinder at large rotation rates.
- Different shedding patterns were resulted in flow forces with different frequencies acting on the cylinder. In the crossflow direction, the dominant frequency of flow forces was found to be close to the system's natural frequency for all the rotation rates tested with either 2S or P vortex shedding pattern. In the inline direction, however, the change from 2S to P shedding at high rotation rates resulted in a shift of the ratio of the dominant frequency of the inline flow forces to the natural frequency of the system from 2:1 to 1:1.

In Chapter 6, flow-induced vibration of a triangular cross-section cylinder was studied experimentally. The response of the cylinder in terms of the amplitude of oscillations as well as the flow forces was studied at varying angles of attack in the range

of α=0º-60º and a reduced velocity range of U^*=4-22. Based on the experimental results, it was concluded that

- The cylinder underwent both VIV and galloping, depending on the angle of attack and the reduced velocity.
- For small angles of attack of α<30º, the cylinder did not oscillate; and for larger angles of α=30º and α=35º, the cylinder underwent VIV for lower reduced velocities (U^*=7-14.5) and galloping for larger reduced velocities (U^*=19.5-22).
- For angles of attack larger than α=35º, the amplitude of oscillations increased monotonically and the cylinder experienced galloping. The amplitude of oscillations reached a maximum dimensionless value of A^*~3.7 at higher reduced velocities for an angle of attack of α=60º.
- Different modes of vortex shedding were observed within the regions where galloping was observed. A full map of different shedding patterns for varying angles of attack and reduced velocities was constructed.
- The flow forces acting on the cylinder in both the crossflow and the inline directions were measured. The flow forces showed contributions from higher harmonics in the frequency content of the lift and drag forces. The existence of higher harmonics was in parallel with high-frequency vortex shedding patterns observed in the wake of the cylinder.

Finally, in Chapter 7, VIV of a flexible vertical and inclined cylinder was studied experimentally. A novel technique was introduced to reconstruct the dynamic response of the flexible cylinder from limited and localized measurement points based on modal

expansion theorem modified using Modal Assurance Criterion (MAC). The dynamic response was studied for different angles of inclination starting from zero (vertical cylinder) to 70^{o} and the validity of the Independence Principle (IP) was investigated. It was concluded that

- Mono- and multi-frequency excitation responses as well as transition from low mode numbers to higher ones were observed.
- Flow forces acting on the cylinder were calculated and they showed a consistent relation between the regions where the cylinder was being excited by the flow ($CLv>0$) and the counterclockwise figure-eight trajectories of oscillations in which the phase difference between the IL and CF directions were in the range of $\varphi_{xy}=[\pi\ 2\pi]$.
- Considering the amplitude of oscillations in the transverse direction for the 1st mode of oscillations, the inclined cylinder behaved similarly to a normal-incidence case for angles of inclination up to 45°, if only the normal flow component was considered. On this basis, it was concluded that the axial flow component had negligible effect on the system response for angles of inclination less than 45°. However, for larger angle of inclination of 70°, the width of the lock-in region was smaller than the other inclinations. Therefore, at this angle of inclination the system did not act as if only the normal component of the flow velocity contributed to the oscillations. On this basis, the axial flow component affected the system response, and the Independence Principle (IP) was not valid.

8.3 Recommendations for future work

In this thesis, vortex-induced vibration of structures with broken symmetry was studied. Several cases were studied in which the asymmetry was introduced into the system from different sources such as geometry of the cross-section, the wake and the boundary conditions. Even though the present study covered several aspects of VIV in structures with broken symmetry, there are still topics that can take this research to the next level.

- This research can be extended further by studying how the oscillations of structures in flow can be converted to useful form of energy. Extraction of energy from vibrating structures and converting it to electrical power has been proposed to be used in electronic components, such as MEMs devices, sensors used in health monitoring and other applications where the devices are not easily accessible or they require expensive maintenance. The level of harvested power needs to be determined based on the system parameters that affect the vibration of the structure. What can be done is to extract energy from vibrations of flexible structures and convert it to electrical power. In this connection, one needs to have a complete understanding of how different systems behave in crossflow. To accomplish this, the findings from this research can be applied to the growing energy harvesting area and contribute to the optimal energy extraction.
- As it was shown in this research, higher harmonics of the flow forces contributed significantly into the dynamic response of structures with broken symmetry. Such high frequency loading has a direct impact on the structural fatigue damage and may lead to catastrophic failure of civil or ocean engineering structures.

These high-frequency and sometimes large-in-amplitude forces are normally neglected in studying fatigue life of marine structures. The findings of this research raise new questions as to how to consider these high frequency forces dealing with fatigue life analysis of engineering structures.

- In this thesis it was shown how VIV can be suppressed by changing the system parameters. As an example, VIV suppression that was observed for high rotation rates in rotating cylinder or zero amplitude of oscillation observed for small angles of attack in triangular cylinder. Further investigations can recommend operation conditions and system parameters that needs to be tuned in operation of such asymmetric systems in order to avoid instability of the structure.

APPENDIX: MEASUREMENT RESOLUTION

In the following the specifications and resolution of the measurement devices used in the course of experiments are provided.

Laser displacement sensor

Laser sensor OptoNCDT 1402 (Figure 1) was used to directly measure the displacement of cylinder in the course of experiments. The sensor measured the displacement without any contact against the surface. The measuring rates for this sensor is in the range of 5-600 mm. Maximum resolution for this device is 0.6 µm. The maximum configurable sampling frequency is up to 1.5 KHz that makes this sensor suitable for measuring high frequency oscillations. Table 1 summarizes the characteristics of the laser displacement sensor.

http://www.micro-epsilon.com/

Figure 1. Laser displacement sensor.

Table 1. Properties of laser displacement sensor.

Details

- Measuring ranges (mm):
  5 | 10 | 20 | 50 | 100 | 200 | 250 | 600
- Linearity max. 9µm
- Resolution max. 0.6µm
- Compact design with integrated electronics
- Configurable measuring rate up to 1.5kHz
- Trigger input and Teach-In
- Peak selection
- CMOS technology
- Scalable analog output
- RS422

http://www.micro-epsilon.com/

Force sensor

A six-axis force sensor (ATI- Nano17/IP68) was used to directly measure the flow forces acting on the cylinder (Figure 2). This force sensor had a capability of high precision measurement of small forces. The calibration SI-25-0.25 had a sensing range of 25 N in the *Fx*, *Fy* and 35 N in *Fz* direction with a resolution of 1/160 N in all three directions. The torque sensing range was 250 N.mm with a resolution of 1/32 N.mm. It weighed 40.8 g and had a height and diameter of 22 mm and 20 mm, respectively. The single axis overload in F_{xy} and F_z were ±250 N and ±480 N, respectively. T_{xy} and T_z had a single axis overload capacity of ±1.6 N.m and ±1.8 N.m (Table 1). The sensor was rated water proof to a depth of 4 m. Table 2 also summarizes the characteristics of the force sensor.

Nano 17/IP68
http://www.ati-ia.com/

Figure 2. Six-axis force sensor.

Table 2. Properties of six-axis force sensor.

Metric Calibrations (SI)

Calibration	Fx,Fy	Fz	Tx,Ty	Tz	Fx,Fy	Fz	Tx,Ty	Tz
SI-12-0.12	12 N	17 N	120 Nmm	120 Nmm	1/320 N	1/320 N	1/64 Nmm	1/64 Nmm
SI-25-0.25	25 N	35 N	250 Nmm	250 Nmm	1/160 N	1/160 N	1/32 Nmm	1/32 Nmm
SI-50-0.5	50 N	70 N	500 Nmm	500 Nmm	1/80 N	1/80 N	1/16 Nmm	1/16 Nmm
	SENSING RANGES				RESOLUTION			

http://www.ati-ia.com/

BIBLIOGRAPHY

Abdelkefi, A., Hajj, M.R., Nayfeh, A.H., 2012. Phenomena and modeling of piezoelectric energy harvesting from freely oscillating cylinders. Nonlinear Dynamics 70, 1377-1388.

Ahmed, A., 2010. On the wake of a circular cylinder with nodal and saddle attachment. J Fluid Struct 26, 41-49.

Alawadhi, E.M., 2013. Numerical simulation of fluid flow past an oscillating triangular cylinder in a channel. Journal of Fluids Engineering 135, 041202.

Allemang, R.J., 2003. The modal assurance criterion–twenty years of use and abuse. Sound and vibration 37, 14-23.

Alonso, G., Meseguer, J., 2006. A parametric study of the galloping stability of two-dimensional triangular cross-section bodies. J Wind Eng Ind Aerod 94, 241-253.

Alonso, G., Sanz-Lobera, A., Meseguer, J., 2012. Hysteresis phenomena in transverse galloping of triangular cross-section bodies. J Fluid Struct 33, 243-251.

Assi, G.R., Srinil, N., Freire, C.M., Korkischko, I., 2014. Experimental investigation of the flow-induced vibration of a curved cylinder in convex and concave configurations. J Fluid Struct 44, 52-66.

Badr, H.M., Coutanceau, M., Dennis, S.C.R., Menard, C., 1990. Unsteady-Flow Past a Rotating Circular-Cylinder at Reynolds-Numbers 10(3) and 10(4). J Fluid Mech 220, 459-484.

Balasubramanian, S., Haan, F.L., Szewczyk, A.A., Skop, R.A., 2001. An experimental investigation of the vortex-excited vibrations of pivoted tapered circular cylinders in uniform and shear flow. J Wind Eng Ind Aerod 89, 757-784.

Bao, Y., Zhou, D., Zhao, Y.J., 2010. A two-step Taylor-characteristic-based Galerkin method for incompressible flows and its application to flow over triangular cylinder with different incidence angles. International journal for numerical methods in fluids 62, 1181-1208.

Bearman, P.W., 1984. Vortex Shedding from Oscillating Bluff-Bodies. Annu Rev Fluid Mech 16, 195-222.

Bernitsas, M.M., Raghavan, K., Ben-Simon, Y., Garcia, E.M., 2008. VIVACE (Vortex Induced Vibration Aquatic Clean Energy): A new concept in generation of clean and renewable energy from fluid flow. Journal of Offshore Mechanics and Arctic Engineering 130, 041101.

Blevins, R.D., 1990. Flow-induced vibration. New York, NY (USA); Van Nostrand Reinhold Co., Inc.

Bokaian, A., Geoola, F., 1984. Hydroelastic instabilities of square cylinders. J Sound Vib 92, 117-141.

Bourguet, R., Karniadakis, G.E., Triantafyllou, M.S., 2011a. Vortex-induced vibrations of a long flexible cylinder in shear flow. J Fluid Mech 677, 342-382.

Bourguet, R., Karniadakis, G.E., Triantafyllou, M.S., 2014. On the validity of the independence principle applied to the vortex-induced vibrations of a flexible cylinder inclined at 60°. J Fluid Struct.

Bourguet, R., Lo Jacono, D., 2014. Flow-induced vibrations of a rotating cylinder. J Fluid Mech 740, 342-380.

Bourguet, R., Lucor, D., Triantafyllou, M.S., 2012. Mono- and multi-frequency vortex-induced vibrations of a long tensioned beam in shear flow. J Fluid Struct 32, 52-64.

Bourguet, R., Modarres-Sadeghi, Y., Karniadakis, G.E., Triantafyllou, M.S., 2011b. Wake-body Resonance of Long Flexible Structures is Dominated by Counterclockwise Orbits. Phys Rev Lett 107.

Bourguet, R., Triantafyllou, M.S., 2015. Vortex-induced vibrations of a flexible cylinder at large inclination angle. Philosophical Transactions of the Royal Society A: Mathematical, Physical and Engineering Sciences 373, 20140108.

Chaplin, J.R., Bearman, P.W., Cheng, Y., Fontaine, E., Graham, J.M.R., Herfjord, K., Huera Huarte, F.J., Isherwood, M., Lambrakos, K., Larsen, C.M., 2005a. Blind predictions of laboratory measurements of vortex-induced vibrations of a tension riser. J Fluid Struct 21, 25-40.

Chaplin, J.R., Bearman, P.W., Huera-Huarte, F.J., Pattenden, R.J., 2005b. Laboratory measurements of vortex-induced vibrations of a vertical tension riser in a stepped current. J Fluid Struct 21, 3-24.

Chew, Y.T., Cheng, M., Luo, S.C., 1995. A Numerical Study of Flow Past a Rotating Circular-Cylinder Using a Hybrid Vortex Scheme. J Fluid Mech 299, 35-71.

Cigeroglu, E., Samandari, H., 2014. Nonlinear free Vibrations of curved double walled carbon Nanotubes using differential quadrature method. Physica E: Low-dimensional Systems and Nanostructures 64, 95-105.

Coutanceau, M., Menard, C., 1985. Influence of Rotation on the near-Wake Development Behind an Impulsively Started Circular-Cylinder. J Fluid Mech 158, 399-446.

Dahl, J.M., Hover, F.S., Triantafyllou, M.S., 2006. Two-degree-of-freedom vortex-induced vibrations using a force assisted apparatus. J Fluid Struct 22, 807-818.

Dahl, J.M., Hover, F.S., Triantafyllou, M.S., Dong, S., Karniadakis, G.E., 2007. Resonant vibrations of bluff bodies cause multivortex shedding and high frequency forces. Phys Rev Lett 99.

De, A.K., Dalal, A., 2007. Numerical study of laminar forced convection fluid flow and heat transfer from a triangular cylinder placed in a channel. Journal of heat transfer 129, 646-656.

de Vecchi, A., Sherwin, S.J., Graham, J.M.R., 2008. Wake dynamics of external flow past a curved circular cylinder with the free-stream aligned to the plane of curvature. J Fluid Struct 24, 1262-1270.

de Vecchi, A., Sherwin, S.J., Graham, J.M.R., 2009. Wake dynamics past a curved body of circular cross-section under forced cross-flow vibration. J Fluid Struct 25, 721-730.

Deniz, S., Staubli, T., 1997. Oscillating rectangular and octagonal profiles: Interaction of leading-and trailing-edge vortex formation. J Fluid Struct 11, 3-31.

Dong, S., Karniadakis, G.E., 2005. DNS of flow past a stationary and oscillating cylinder at. J Fluid Struct 20, 519-531.

Du, L., Jing, X., Sun, X., 2014. Modes of vortex formation and transition to three-dimensionality in the wake of a freely vibrating cylinder. J Fluid Struct.

Evangelinos, C., Lucor, D., Karniadakis, G., 2000. DNS-derived force distribution on flexible cylinders subject to vortex-induced vibration. J Fluid Struct 14, 429-440.

Feng, C.C., 1968. The measurement of vortex induced effects in flow past. University of British Columbia.

Franzini, G.R., Fujarra, A.L.C., Meneghini, J.R., Korkischko, I., Franciss, R., 2009. Experimental investigation of Vortex-Induced Vibration on rigid, smooth and inclined cylinders. J Fluid Struct 25, 742-750.

Franzini, G.R., Gonçalves, R.T., Meneghini, J.R., Fujarra, A.L.C., 2013. One and two degrees-of-freedom Vortex-Induced Vibration experiments with yawed cylinders. J Fluid Struct 42, 401-420.

Gaster, M., 1969. Vortex Shedding from Slender Cones at Low Reynolds Numbers. J Fluid Mech 38, 565-&.

Gaster, M., 1971. Vortex Shedding from Circular Cylinders at Low Reynolds Numbers. J Fluid Mech 46, 749-&.

Gedikli, E.D., Dahl, J.M., 2014. Mode Shape Variation for a Low-Mode Number Flexible Cylinder Subject to Vortex-Induced Vibrations, ASME 2014 33rd International Conference on Ocean, Offshore and Arctic Engineering. American Society of Mechanical Engineers, pp. V002T008A071-V002T008A071.

Grouthier, C., Michelin, S., de Langre, E., 2012. Energy harvesting using vortex-induced vibrations of tensioned cables. arXiv preprint arXiv:1203.0236.

Helfrick, M.N., Niezrecki, C., Avitabile, P., Schmidt, T., 2011. 3D digital image correlation methods for full-field vibration measurement. Mechanical Systems and Signal Processing 25, 917-927.

Hover, F.S., Techet, A.H., Triantafyllou, M.S., 1998. Forces on oscillating uniform and tapered cylinders in crossflow. J Fluid Mech 363, 97-114.

Hsiao, F.B., Chiang, C.H., 1998. Experimental study of cellular shedding vortices behind a tapered circular cylinder. Exp Therm Fluid Sci 17, 179-188.

Huera-Huarte, F., Bangash, Z., González, L., 2014. Towing tank experiments on the vortex-induced vibrations of low mass ratio long flexible cylinders. J Fluid Struct 48, 81-92.

Huera-Huarte, F.J., Bearman, P.W., 2009a. Wake structures and vortex-induced vibrations of a long flexible cylinder—part 1: dynamic response. J Fluid Struct 25, 969-990.

Huera-Huarte, F.J., Bearman, P.W., 2009b. Wake structures and vortex-induced vibrations of a long flexible cylinder—part 2: drag coefficients and vortex modes. J Fluid Struct 25, 991-1006.

Huera-Huarte, F.J., Bearman, P.W., Chaplin, J.R., 2006. On the force distribution along the axis of a flexible circular cylinder undergoing multi-mode vortex-induced vibrations. J Fluid Struct 22, 897-903.

Jain, A., Modarres-Sadeghi, Y., 2013. Vortex-induced vibrations of a flexibly-mounted inclined cylinder. J Fluid Struct 43, 28-40.

Jauvtis, N., Williamson, C.H.K., 2004. The effect of two degrees of freedom on vortex-induced vibration at low mass and damping. J Fluid Mech 509, 23-62.

Jeon, D., Gharib, M., 2001. ON CIRCULAR CYLINDERS UNDERGOING TWO-DEGREE-OF-FREEDOM FORCED MOTIONS. J Fluid Struct 15, 533-541.

Jhingran, V., Vandiver, J.K., 2007. Incorporating the higher harmonics in VIV fatigue predictions, ASME 2007 26th International Conference on Offshore Mechanics and Arctic Engineering. American Society of Mechanical Engineers, pp. 891-899.

Kaasen, K.E., Lie, H., Solaas, F., Vandiver, J.K., 2000. Norwegian deepwater program: analysis of vortex-induced vibrations of marine risers based on full-scale measurements, Offshore Technology Conference. Offshore Technology Conference.

Kang, S.M., Choi, H.C., Lee, S., 1999. Laminar flow past a rotating circular cylinder. Phys Fluids 11, 3312-3321.

Khalak, A., Williamson, C.H.K., 1997a. Fluid forces and dynamics of a hydroelastic structure with very low mass and damping. J Fluid Struct 11, 973-982.

Khalak, A., Williamson, C.H.K., 1997b. Investigation of relative effects of mass and damping in vortex-induced vibration of a circular cylinder. J Wind Eng Ind Aerod 69, 341-350.

Khalak, A., Williamson, C.H.K., 1999. Motions, forces and mode transitions in vortex-induced vibrations at low mass-damping. J Fluid Struct 13, 813-851.

Kumar De, A., Dalal, A., 2006. Numerical simulation of unconfined flow past a triangular cylinder. International journal for numerical methods in fluids 52, 801-821.

Kumar, S., Cantu, C., Gonzalez, B., 2011. Flow Past a Rotating Cylinder at Low and High Rotation Rates. J Fluid Eng-T Asme 133.

Larsen, C., Vikestad, K., Yttervik, R., Passano, E., 2000. VIVANA Theory manual". MARINTEK report, Trondheim.

Lie, H., Kaasen, K., 2006. Modal analysis of measurements from a large-scale VIV model test of a riser in linearly sheared flow. J Fluid Struct 22, 557-575.

Lucor, D., Imas, L., Karniadakis, G.E., 2001. Vortex dislocations and force distribution of long flexible cylinders subjected to sheared flows. J Fluid Struct 15, 641-650.

Lucor, D., Karniadakis, G.E., 2003. Effects of oblique inflow in vortex-induced vibrations. Flow Turbul Combust 71, 375-389.

Miliou, A., De Vecchi, A., Sherwin, S.J., Graham, J.M.R., 2007. Wake dynamics of external flow past a curved circular cylinder with the free stream aligned with the plane of curvature. J Fluid Mech 592, 89-115.

Miliou, A., Sherwin, S.J., Graham, J.M.R., 2003. Fluid dynamic loading on curved riser pipes. J Offshore Mech Arct 125, 176-182.

Mittal, S., Kumar, B., 2003. Flow past a rotating cylinder. J Fluid Mech 476, 303-334.

Modarres-Sadeghi, Y., Chasparis, F., Triantafyllou, M.S., Tognarelli, M., Beynet, P., 2011. Chaotic response is a generic feature of vortex-induced vibrations of flexible risers. J Sound Vib 330, 2565-2579.

Modarres-Sadeghi, Y., Mukundan, H., Dahl, J.M., Hover, F.S., Triantafyllou, M.S., 2010. The effect of higher harmonic forces on fatigue life of marine risers. J Sound Vib 329, 43-55.

Modi, V.J., 1997. Moving surface boundary-layer control: A review. J Fluid Struct 11, 627-663.

Morse, T., Govardhan, R., Williamson, C., 2008. The effect of end conditions on the vortex-induced vibration of cylinders. J Fluid Struct 24, 1227-1239.

Mukundan, H., Modarres-Sadeghi, Y., Dahl, J.M., Hover, F.S., Triantafyllou, M.S., 2009. Monitoring VIV fatigue damage on marine risers. J Fluid Struct 25, 617-628.

Narasimhamurthy, V.D., Andersson, H.I., Pettersen, B., 2009. Cellular vortex shedding behind a tapered circular cylinder. Phys Fluids 21.

Naudascher, E., Wang, Y., 1993. Flow-induced vibrations of prismatic bodies and grids of prisms. J Fluid Struct 7, 341-373.

Nemes, A., Zhao, J., Lo Jacono, D., Sheridan, J., 2012. The interaction between flow-induced vibration mechanisms of a square cylinder with varying angles of attack. J Fluid Mech 710, 102-130.

Obasaju, E., Ermshaus, R., Naudascher, E., 1990. Vortex-induced streamwise oscillations of a square-section cylinder in a uniform stream. J Fluid Mech 213, 171-189.

Paidoussis, M.P., 1998. Fluid-structure interactions: slender structures and axial flow. Academic press.

Papangelou, A., 1992. Vortex Shedding from Slender Cones at Low Reynolds-Numbers. J Fluid Mech 242, 299-321.

Parkinson, G., Smith, J., 1964. The square prism as an aeroelastic non-linear oscillator. The Quarterly Journal of Mechanics and Applied Mathematics 17, 225-239.

Parkinson, G., Wawzonek, M., 1981. Some considerations of combined effects of galloping and vortex resonance. J Wind Eng Ind Aerod 8, 135-143.

Parnaudeau, P., Heitz, D., Lamballais, E., Silvestrini, J.H., 2007. Direct numerical simulations of vortex shedding behind cylinders with spanwise linear nonuniformity. J Turbul 8, 1-13.

Pastor, M., Binda, M., Harčarik, T., 2012. Modal Assurance Criterion. Modelling of Mechanical and Mechatronics Systems 48, 543-548.

Piccirillo, P.S., Van Atta, C., 1993. An experimental study of vortex shedding behind linearly tapered cylinders at low Reynolds number. J Fluid Mech 246, 163-195.

Pralits, J.O., Brandt, L., Giannetti, F., 2010. Instability and sensitivity of the flow around a rotating circular cylinder. J Fluid Mech 650, 513-536.

Provansal, M., Monkewitz, P., 2006. Vortex shedding dynamics in the laminar wake of cones. 12th International Symposium on Flow Visualization, Gottingen, Germany.

Ramberg, S.E., 1983. The Effects of Yaw and Finite Length Upon the Vortex Wakes of Stationary and Vibrating Circular-Cylinders. J Fluid Mech 128, 81-107.

Rao, A., Leontini, J.S., Thompson, M.C., Hourigan, K., 2013. Three-dimensionality in the wake of a rapidly rotating cylinder in uniform flow. J Fluid Mech 730, 379-391.

Rao, A., Radi, A., Leontini, J.S., Thompson, M.C., Sheridan, J., Hourigan, K., A review of rotating cylinder wake transitions. J Fluid Struct.

Sarpkaya, T., 2004. A critical review of the intrinsic nature of vortex-induced vibrations. J Fluid Struct 19, 389-447.

Seyed-Aghazadeh, B., Carlson, D.W., Modarres-Sadeghi, Y., 2014. The influence of taper ratio on vortex-induced vibration of tapered cylinders in the crossflow direction. J Fluid Struct.

Shi, C., Manuel, L., Tognarelli, M., Botros, T., 2012. On the vortex-induced vibration response of a model riser and location of sensors for fatigue damage prediction. Journal of Offshore Mechanics and Arctic Engineering 134, 031802.

Srigrarom, S., Koh, A., 2008. Flow field of self-excited rotationally oscillating equilateral triangular cylinder. J Fluid Struct 24, 750-755.

Stansby, P.K., Rainey, R.C.T., 2001a. A CFD study of the dynamic response of a rotating cylinder in a current. J Fluid Struct 15, 513-521.

Stansby, P.K., Rainey, R.C.T., 2001b. On the orbital response of a rotating cylinder in a current. J Fluid Mech 439, 87-108.

Stojkovic, D., Breuer, M., Durst, F., 2002. Effect of high rotation rates on the laminar flow around a circular cylinder. Phys Fluids 14, 3160-3178.

Su, Z., Liu, Y., Zhang, H., Zhang, D., 2007. Numerical simulation of vortex-induced vibration of a square cylinder. Journal of mechanical science and technology 21, 1415-1424.

Surry, J., Surry, D., 1967. THE EFFECT OF INCLINATION ON THE STROUHAL NUMBER AND OTHER WAKE PROPERTIES OF CIRCULAR CYLINDERS AT SUBCRITICAL REYNOLDS NUMBERS.

Takamoto, M., Izumi, K., 1981. Experimental-Observation of Stable Arrangement of Vortex Rings. Phys Fluids 24, 1582-1583.

Techet, A.H., Hover, F.S., Triantafyllou, M.S., 1998. Vortical patterns behind a tapered cylinder oscillating transversely to a uniform flow. J Fluid Mech 363, 79-96.

Thakur, A., Liu, X., Marshall, J.S., 2004. Wake flow of single and multiple yawed cylinders. J Fluid Eng-T Asme 126, 861-870.

Tokumaru, P.T., Dimotakis, P.E., 1991. Rotary Oscillation Control of a Cylinder Wake. J Fluid Mech 224, 77-&.

Tokumaru, P.T., Dimotakis, P.E., 1993. The Lift of a Cylinder Executing Rotary Motions in a Uniform-Flow. J Fluid Mech 255, 1-10.

Triantafyllou, M., Triantafyllou, G., Tein, Y., Ambrose, B.D., 1999. Pragmatic riser VIV analysis, Offshore Technology Conference. Offshore Technology Conference.

Trim, A., Braaten, H., Lie, H., Tognarelli, M., 2005. Experimental investigation of vortex-induced vibration of long marine risers. J Fluid Struct 21, 335-361.

Tu, J., Zhou, D., Bao, Y., Han, Z., Li, R., 2014. Flow characteristics and flow-induced forces of a stationary and rotating triangular cylinder with different incidence angles at low Reynolds numbers. J Fluid Struct 45, 107-123.

Valles, B., Andersson, H.I., Jenssen, C.B., 2002. Oblique vortex shedding behind tapered cylinders. J Fluid Struct 16, 453-+.

Vanatta, C.W., 1968. Experiments on Vortex Shedding from Yawed Circular Cylinders. Aiaa J 6, 931-&.

Vandiver, J., Marcollo, H., Swithenbank, S., Jhingran, V., 2006. High-mode-number vortex-induced-vibration field experiments. Journal of petroleum technology 58, 69-70.

Vandiver, J.K., 1993. Dimensionless Parameters Important to the Prediction of Vortex-Induced Vibration of Long, Flexible Cylinders in Ocean Currents. J Fluid Struct 7, 423-455.

Vandiver, J.K., 2012. Damping Parameters for flow-induced vibration. J Fluid Struct 35, 105-119.

Vandiver, J.K., Jaiswal, V., Jhingran, V., 2009. Insights on vortex-induced, traveling waves on long risers. J Fluid Struct 25, 641-653.

Vandiver, J.K., Li, L., 1995. SHEAR7 program theoretical manual. Massachusetts Institute of Technology (MIT) July.

Visscher, J., Pettersen, B., Andersson, H.I., 2011. Experimental study on the wake behind tapered circular cylinders. J Fluid Struct 27, 1228-1237.

Wang, S., Zhu, L., Zhang, X., He, G., 2011. Flow Past Two Freely Rotatable Triangular Cylinders in Tandem Arrangement. Journal of Fluids Engineering 133, 081202.

Wang, X.Q., So, R.M.C., Chan, K.T., 2003. A non-linear fluid force model for vortex-induced vibration of an elastic cylinder. J Sound Vib 260, 287-305.

Williamson, C.H.K., 1996. Three-dimensional wake transition. J Fluid Mech 328, 345-407.

Williamson, C.H.K., Govardhan, R., 2004. Vortex-induced vibrations. Annu Rev Fluid Mech 36, 413-455.

Williamson, C.H.K.R.A., 1988. Vortex formation in the wake of an oscillating cylinder. YJFLS Journal of Fluids and Structures 2, 355-381.

Wu, X.D., Ge, F., Hong, Y.S., 2012. A review of recent studies on vortex-induced vibrations of long slender cylinders. J Fluid Struct 28, 292-308.

Zeinoddini, M., Tamimi, V., Seif, M.S., 2013. Stream-wise and cross-flow vortex induced vibrations of single tapered circular cylinders: An experimental study. Appl Ocean Res 42, 124-135.

Zhao, M., Cheng, L., Lu, L., 2014. Vortex induced vibrations of a rotating circular cylinder at low Reynolds number. Physics of Fluids (1994-present) 26, 073602.

Zhao, M., Cheng, L., Zhou, T., 2009. Direct numerical simulation of three-dimensional flow past a yawed circular cylinder of infinite length. J Fluid Struct 25, 831-847.

Zhao, M., Cheng, L., Zhou, T., 2013. Numerical simulation of vortex-induced vibration of a square cylinder at a low Reynolds number. Physics of Fluids (1994-present) 25, 023603.